WAPD-TM-1340
DOE RESEARCH AND
DEVELOPMENT REPORT

PROPERTIES OF THORIA AND THORIA-URANIA: A REVIEW

(LWBR Development Program)

JUNE 1978

CONTRACT EY-76-C-11-0014

BETTIS ATOMIC POWER LABORATORY
WEST MIFFLIN, PENNSYLVANIA

Operated for the U. S. Department of Energy by
WESTINGHOUSE ELECTRIC CORPORATION

DISCLAIMER

WAPD-TM-1340

Special External Distribution

PROPERTIES OF THORIA AND THORIA-URANIA: A REVIEW
(LWBR Development Program)

J. Belle and R. M. Berman

June 1978

Contract No. EY-76-C-11-0014

Printed in the United States of America
Available from the
National Technical Information Service
U. S. Department of Commerce
5285 Port Royal Road
Springfield, Virginia 22151

NOTE

This document is an interim memorandum prepared primarily for internal reference and does not represent a final expression of the opinion of Westinghouse. When this memorandum is distributed externally, it is with the express understanding that Westinghouse makes no representation as to completeness, accuracy, or usability of information contained therein.

080 6000

BETTIS ATOMIC POWER LABORATORY
West Mifflin, Pennsylvania

Operated for the U. S. Department of Energy by
WESTINGHOUSE ELECTRIC CORPORATION

FOREWORD

The Shippingport Atomic Power Station located in Shippingport, Pennsylvania was the first large-scale, central-station nuclear power plant in the United States and the first plant of such size in the world operated solely to produce electric power. This project was started in 1953 to confirm the practical application of nuclear power for large-scale electric power generation. It has provided much of the technology being used for design and operation of the commercial, central-station nuclear power plants now in use.

Subsequent to development and successful operation of the Pressurized Water Reactor in the DOE-owned reactor plant at the Shippingport Atomic Power Station, the Atomic Energy Commission in 1965 undertook a research and development program to design and build a Light Water Breeder Reactor core for operation in the Shippingport Station. In 1976, with fabrication of the Light Water Breeder Reactor (LWBR) nearing completion the Energy Research and Development Administration established the Advanced Water Breeder Applications program (AWBA) to develop and disseminate technical information which would assist U.S. industry in evaluating the LWBR-concept. All three of these reactor development projects have been administered by the Division of Naval Reactors with the goal of developing practical improvements in the utilization of nuclear fuel resources for generation of electrical energy using water-cooled nuclear reactors.

The objective of the Light Water Breeder Reactor project has been to develop a technology that would significantly improve the utilization of the nation's nuclear fuel resources employing the well-established water reactor technology. To achieve this objective, work has been directed toward analysis, design, component tests, and fabrication of a water-cooled, thorium oxide fuel cycle breeder reactor to install and operate at the Shippingport Station. Operation of the LWBR core in the Shippingport Station started in the Fall of 1977 and is expected to be completed in about 3 to 4 years. Then the fissionable fuel inventory of the core will be measured. This effort, when completed in about 2 to 3 years after completion of LWBR core operation, is expected to confirm that breeding actually took place.

The Advanced Water Breeder Applications (AWBA) project was initiated to develop and disseminate technical information that will assist U.S. industry in evaluating the LWBR concept for commercial-scale applications. The project will explore some of the problems that would be faced by industry in adapting technology confirmed in the LWBR program. Information to be developed includes concepts for commercial-scale prebreeder cores which will produce uranium-233 for light water breeder cores while producing electric power, improvements for breeder cores based on the technology developed to fabricate and operate the Shippingport LWBR core, and other information and technology to aid in evaluating commercial-scale application of the LWBR concept.

Technical information developed under the Shippingport, LWBR, and AWBA projects has been and will continue to be published in technical memoranda, one of which is this present report.

TABLE OF CONTENTS

TABLE OF CONTENTS (Cont)

LIST OF TABLES

LIST OF TABLES (Cont)

LIST OF FIGURES

LIST OF FIGURES (Cont)

Information on the physical, chemical, and mechanical properties of thoria and thoria-urania is reviewed and assessed. The properties discussed are those judged to be important for an understanding of the behavior of these oxides as nuclear fuel materials. Evaluation was made, where possible, of the effects of composition, material variables, temperature, and irradiation exposure. Data were taken from a review of the literature and from both published and unpublished data derived from the Light Water Breeder Reactor (LWBR) Program at the Bettis Atomic Power Laboratory.

PROPERTIES OF THORIA AND THORIA-URANIA: A REVIEW
(LWBR Development Program)

J. Belle and R. M. Berman

I. INTRODUCTION

This review summarizes and assesses information on those properties of thoria and thoria-urania that are of major importance to use of these materials as nuclear fuels. A significant part of the information discussed in this report was obtained from work carried out as part of the Light Water Breeder Reactor (LWBR) Program.

An earlier compilation of physical, chemical, and mechanical properties of thoria, alone and in combination with other oxides, was published as a data manual by Oak Ridge National Laboratory in September, 1970 (Reference 1). A subsequent compilation was issued in May, 1977 (Reference 2). The present report is not an updated version of the previously published data manuals but is an assessment of some of the material properties of both ThO_2 and ThO_2-UO_2 solid solutions. Information previously presented in Bettis reports as well as unpublished Bettis data and published information in the literature are incorporated in this review. Among the properties that are discussed are the following: crystal properties, solid solution formation, thermal properties, thermodynamic functions, vaporization behavior, diffusion kinetics, mechanical properties, stability in high-temperature water, and gas adsorption and release. Excluded from this report are topics concerned with fuel fabrication, sintering kinetics and grain growth, fuel element irradiation behavior, and nuclear

properties since these subjects are covered in other Bettis reports. Those material properties not of direct concern to nuclear application are also excluded from this review.

II. CRYSTAL PROPERTIES OF ThO_2

A. Structure

The only oxide of thorium with significant stability is ThO_2, thorium dioxide (thoria). Below its melting point ThO_2 occurs only as a cubic phase having the fluorite structure, which was first identified and described for the material fluorite (CaF_2).

The fluorite structure is represented in Figure 1. The pattern shown here is repeated indefinitely in three dimensions. Each thorium ion (dark sphere) is surrounded by eight oxygen ions (light sphere) at the corners of a cube of which the thorium ion is the center. Each oxygen ion is surrounded by a similar cube, but only four of the eight corners are occupied by thorium ions. The four thorium ions form a tetrahedron surrounding the oxygen ion.

Oxides with the fluorite-type structure have the capability of accommodating a wide variety of metallic elements in solid solution in the cation positions normally occupied by thorium. By contrast, oxygen is the only anion accepted to any significant extent although the oxygen positions may be vacant. (There is a completely separate series of fluorite-type oxyfluorides with the general formula MOF). There are also interstitial positions, the unoccupied four corners of the cube surrounding the oxygen ions. These may accommodate additional oxygens, as in the case of uranium dioxide. The cation lattice can experience a wide variety of substitutions of ions that have approximately the same atomic radius, within a factor of about 1.5, as the ion being replaced. If, however, the newly-introduced impurity atom has a different ionic charge than the ion it replaces, there must be compensation for it in the anion lattice to maintain overall electric neutrality. This compensation takes the form of an interstitial oxygen (to compensate for two extra positive charges) or an oxygen omission from the regular anion lattice, leaving a vacancy and compensating for two extra negative charges.

B. Composition

Unlike uranium dioxide, thorium dioxide cannot accommodate oxygen in excess of its stoichiometric composition of ThO_2. At high temperatures, however, it is possible to produce thoria that is somewhat deficient in oxygen. For example,

thoria blackens in color with loss of oxygen after exposure to a temperature of 1800°C or higher in a vacuum or in a reducing atmosphere, but the loss is too small to correlate with either chemical analysis or lattice parameter change.

The minimum content of oxygen in the fluorite phase at any given temperature is the composition that is in equilibrium with thorium metal. Above the eutectic at 1735 ± 20°C, the metallic phase consists of liquid thorium metal with some oxygen in solution. In his study of the thorium-oxygen system, Benz (Reference 3) delineated the phase boundaries and therefore the limits of the fluorite-type phase. At the 1735°C eutectic the minimum oxygen content for the fluorite-type phase is given as $ThO_{1.985\pm0.01}$. As the temperature is raised, the minimum oxygen subscript decreases along an approximate straight line, reaching a value of $ThO_{1.87\pm0.04}$ at a higher eutectic, 2740 ± 100°C. Above this, the minimum oxygen subscript increases, reaching 2 at the melting temperature of 3370°C*. The maximum variation of oxygen content in thoria is therefore from 1.87 to 2 atoms per formula unit at 2740°C.

C. Diffractogram of Pure ThO_2

A face-centered-cubic structure, such as that shown in Figure 1, produces observable diffraction peaks only for those sets of planes having Miller Indices, h, k, and l, that are either all even or all odd. The peaks observable with copper K_α x-rays are listed in Table 1 together with newly calculated position and intensity data based on the latest available wave length and atomic scattering factor data (Reference 4). Table 1 also lists similar data for five other commonly-used x-ray wave lengths.

In calculating the positions of Table 1, the edge of the unit cell of pure thoria was taken as 5.5975Å. This is a consensus value based on many measurements made on reactor-grade material at the Bettis Atomic Power Laboratory. A typical sample of pure, well-crystallized thoria, made by calcining thorium oxalate for example, gives a diffractogram of excellent quality, with exceptionally sharp, strong peaks at highly reproducible diffraction angles.

In general, there should be no significant peak broadening or shifting due to strain or to small grain size. Grain size of calcined thoria is on the order of 1μm. (Note that the sol-gel type of thoria preparation has a much smaller grain size and shows x-ray diffraction peak broadening.) Calcined thoria may therefore be used as an internal or external standard in the study of other

---

*Benz (Reference 3) reported the melting point of ThO_2 as 3390°C; however, see discussion below in Section V.A.

materials; the observed width of its peaks may be ascribed to instrumental factors and applied as a correction to the peaks of the material of interest, and the variation of its Bragg angles from the calculated values of Table 1 may be taken as an assessment of instrumental error in each local section of the diffractogram.

Values listed in Table 1 are for 25°C. Thoria may also be used as an internal standard for high-temperature x-ray diffractometry studies. Indeed, thoria is probably the best material for this purpose; it is refractory, non-reactive, and continues to give an excellent diffractogram as the temperature is raised. A correction must, however, be made for thermal expansion. Values for the unit cell of thoria as a function of temperature are discussed in Section V.C.

D. Cell Size and Calculated (Theoretical) Density

The volume of the cubic unit cell shown in Figure 1 is $(5.5975\text{Å})^3 = 175.381\text{Å}^3 = 1.75381 \times 10^{-22}$ cm^3. The unit cell contains 4 thorium and 8 oxygen ions which together have a mass, in atomic weight units, of $4(232.038) + 8(15.994) = 1056.147$, which is equivalent to $1056.147/(6.02252 \times 10^{23}) = 1.75366 \times 10^{-21}$ grams. The theoretical density may therefore be calculated as $(1.75366 \times 10^{-21})/(1.75381 \times 10^{-22}) = 9.9992$ g/cm^3 = 10.00 g/cm^3 for pure ThO_2 at 25°C.

E. Lattice Energy

The lattice energy, a measure of the stability of the lattice, is the energy that would be released at 0°K by the formation of the lattice from a gas consisting of its separate ions. It is one of the factors affecting the heat of formation of solid crystalline ThO_2 or UO_2 from its gaseous constituent elements; the others are energy terms associated with the vaporization of the metal, the dissociation of O_2, the affinity of the oxygen atom for two electrons, and the first four ionization potentials of the thorium or uranium atom. Since all the other terms can be measured, the lattice energy can be calculated. A calculation of this type is known as the Born-Haber Cycle.

These calculations have been performed by Childs and Benson, et al (References 5 and 6). The two authors use slightly different values for certain terms representing different assessments of the available data. The calculations differ also in that Childs calculated the lattice energy from electrostatic,

Van der Walls, and repulsion terms and arrived at a value for the heat of formation which he compared with experimental data, while Benson, et al, used the experimental data. The calculation is as follows:

$$U = \Delta H - L - D + 2A - \Sigma I_i \qquad \text{(Eq. 1)}$$

where

U = lattice energy

ΔH = heat of formation of the crystalline solid

L = heat of vaporization of the metal

D = dissociation energy of O_2

A = affinity of O atom for two electrons

ΣI_i = sum of first four ionization potentials of the metal atom.

The calculations are summarized in Table 2.

A summary of some of the properties of the crystal structures of ThO_2 and UO_2 is given in Table 3.

III. ThO_2 SOLID SOLUTIONS

A. Cell Size and Calculated Density

The addition to ThO_2 of other constituents in solid solution changes the theoretical density by altering the molecular weight, which can be calculated from Vegard's Law. Vegard's Law states that the cell size of cubic solid solutions varies linearly with molar composition. To obtain the cell size of a solid solution, therefore, the mole fraction of each component is multiplied by an appropriate coefficient, and the results are added together.

The coefficients to be used for this purpose are listed in Table 4. The first group of values listed in Table 4 consists of the measured cell sizes of pure dioxides with fluorite-type structures. These dioxides can be mixed in any proportion, the result being a single fluorite-type cubic phase; however, there may be compositional regions for mixtures containing Tb or Hf where a single cubic phase is not stable. Where such a phase can be fabricated, however its cell size should be predictable by Vegard's Law, and its density may then be calculated from its composition and its cell volume.

For the second group of substances in Table 4, pure dioxide end-members with face-centered-cubic structures are not available. (ZrO_2 has a monoclinic structure that may be considered as a distorted fluorite-type arrangement.) The values given were obtained by extrapolation from measurements on solid solutions.

For the third and final group of values, it was necessary to calculate, from tabulated ionic radii (Reference 7) the cell size that a hypothetical cubic dioxide would have if it were stable. Where radii of the +4 ion were not available, they were estimated by multiplying the value for the corresponding +3 ion by 0.866. This factor was obtained by averaging the ratios in cases where radii were available for both +3 and +4 ions.

Table 4 also lists separate values for U^{+4}, U^{+5}, and U^{+6}. In unoxidized thoria-urania solid solutions, the cell size can be calculated using the coefficients for Th and U^{+4}. Where there is slight to moderate oxidation, the calculation can be performed by considering the oxidized uranium to consist entirely of a separate species, U^{+5}. However, in dilute solutions of urania in thoria, oxidized to the maximum extent possible, a significant portion of the uranium consists of U^{+6}, and this must be taken into account in the calculation as a fourth type of cation (together with Th, U^{+4}, and U^{+5}).

Table 4 also includes the symbol $\square$ for anion-vacancies. Available data on lanthanide-bearing solid solutions indicate that, for each mole of vacancies per mole of material, the cell size is decreased by 0.061 angstroms.

There are certain compositional regions where minor departures from Vegard's Law have been found experimentally. Among these is a region in the ThO_2-UO_2 binary close to the composition of UO_2 (about 2 mole percent ThO_2). Measured cell sizes in this small region are slightly less than would be calculated by Vegard's Law. This is discussed more fully in Sections IV and V.

B. Extent of Solid Solution

Cation solid solution in thoria takes place by the substitution of other metallic ions for thorium ions in the lattice. The extent to which this substitution is permitted depends largely on the size mismatch between the newly-introduced ion and the thorium ion it replaces. The Th^{+4} ion has a radius of 1.02Å; those of Ce^{+4}, U^{+4}, and Pa^{+4}, for example, are 0.92Å, 0.97Å, and 1.08Å, respectively. Thoria is known to form complete and continuous solid solutions between itself and the fluorite-type dioxides of the other ions mentioned.

Relationships in the binary systems between thoria and the other actinide dioxides have not been fully characterized. However, fluorite-type dioxides exist for all of them, at least through californium (Z = 98). Figure 2 shows the decrease in cell size and in ionic radius with increasing atomic number (Reference 8). Even for californium, the last of the series for which information is available, the size mismatch with thorium ions is only about 12 percent.

Since mismatches up to about 28 percent can be tolerated in other complete solid solution series, it is reasonable to assume that all the cubic actinide dioxides are miscible in all proportions.

The ionic radius of Hf^{+4} is 0.78Å and that of Zr^{+4} is 0.79Å. Zirconium forms a cubic fluorite-type dioxide that is stable only above 2300°C; at lower temperatures the oxide can be "stabilized" by various additives, but thorium is not one of these. It seems probable, however, that thoria, like urania, forms a continuous solid solution with zirconia at temperatures above 2300°C; at lower temperatures, extensive but not complete solid solutions exist. Below 1800°C the extent of solid solution is very limited, i.e., <2 percent (Reference 9). Similar relationships probably occur in the thoria-hafnia binary system.

The thoria-lanthanide oxide binary systems have been investigated (Reference 10). The extent of lanthanide solubility in thoria is substantial but, except in the case of CeO_2, not complete. The lower atomic number lanthanide oxides (except CeO_2) have a maximum solubility of 50 to 70 mole percent in thoria; the limit declines with decreasing temperature and increasing atomic number. There is also a much more limited solubility of thorium ion in the lanthanide-rich phases of the systems. The yttria-thoria binary system behaves similarly to intermediate atomic number members of the lanthanide-thoria systems.

Among the divalent elements, Ca^{+2} may be incorporated into ThO_2 to a small extent through the addition of CaO. The maximum solubility of calcia in thoria is probably less than 2 mole percent (Reference 9).

IV. The ThO_2-UO_2 SYSTEM

A. Extent of Solid Solution

The ThO_2-UO_2 system has been studied by various investigators. Work through early 1961, summarized in Reference 11, showed that ThO_2 and UO_2 form a continuous series of face-centered-cubic solid solutions and that the lattice parameters follow Vegard's Law quite closely. The most extensive of the early work was that of Lambertson, et at (Reference 12), who used a quench technique to examine samples heated to temperatures either just above or just below melting. In later work, Christensen (Reference 13) used the tungsten filament technique to investigate the region below 20 mole percent ThO_2 in greater detail than did Lambertson, et al. He reported a significant departure from ideal solid solubility, indicated by both the appearance of a minimum at about 2 mole percent ThO_2 and the departure from Vegard's Law in a plot of lattice parameter versus

composition. These results reproduced in Figure 3 show that the minimum occurred between 2 and 4 weight percent ThO_2 for both the solid solution and the liquidus. Cohen and Berman (Reference 14) confirmed the anomalous minimum but found that Vegard's Law was followed very closely for all other compositions. The compositions, lattice constants, and theoretical densities are listed in Tables 5 and 6 and are plotted in Figures 4 and 5. The region of interest for LWBR application, the high ThO_2, low UO_2 portion, appears to conform to ideal solid solution behavior. A refinement in the solidus and liquidus temperatures in the high UO_2 region of the ThO_2-UO_2 system is discussed in Section V.A.

B. The ThO_2-UO_2-O System

When heated in air or in other oxidizing media, the ThO_2-UO_2 solid solution can take up oxygen to an extent that depends on temperature and oxygen activity and increases with uranium content. Cohen and Berman (Reference 14) conducted a metallographic and x-ray study of the limits of oxygen solubility in ThO_2-UO_2, and significant result are summarized in this report.

Figure 6 shows the UO_2-ThO_2-O diagram as delineated at 1200°C. In general, this work agrees well with the results of an earlier study (Reference 15).

The diagram shows that a continuous, fluorite-type solid solution forms between UO_2 and ThO_2. This solid solution can be oxidized continuously, while still remaining a single cubic phase, to any composition up to a certain definite limit which depends primarily on the U/Th ratio but also on temperature and the partial pressure of oxygen. This limit, which is represented by the curved line running from $UO_{2.25}$ to ThO_2, is called the oxidation limit. The region between the bottom of the diagram and the oxidation limit is the stability field of the cubic, fluorite-type phase.

High-urania compositions are in equilibrium with the U_5O_{13} edge of the U_3O_{8-x} field at the oxidation limit. Material with a bulk composition falling outside the oxidation limit is found, on x-ray and ceramographic investigation, to consist of appropriate amounts of two phases.

One of these phases consists of an orthorhombic phase with cell dimensions that do not differ significantly from the nominal values for U_5O_{13}. There is no reason to believe that this material incorporates any substantial amount of thorium. The other phase consists of cubic material with a composition lying

on the oxidation limit. Its cell size corresponds to the Vegard's Law value for the end of a straight tie-line running from U_3O_{8-x} through the position of the bulk composition of the two-phase mixture to the oxidation limit.

This phenomenon is not observed in high-thoria compositions. It is possible to oxidize these compositions only to the oxidation limit. No solid phase corresponding to the U_3O_{8-x} phases appears. At the oxidation limit, these compositions are in equilibrium with air or the oxidizing furnace atmosphere. At the composition at which one type of behavior changes to the other, U_3O_{8-x}, the oxidizing furnace atmosphere, and the cubic oxide phase at the oxidation limit are all in equilibrium; these represent the corners of a triangular three-phase field. The location of the corner along the oxidation limit is believed to vary somewhat with temperature and with partial pressure of oxygen; that is, there is a fairly significant movement of the corner of the triangle along the line which can be regarded as fixed. However, the effects of these factors have not been thoroughly explored.

The behavior of the corner of the three-phase field was explored by Gilpatrick, et al (Reference 16). They reported that the position of the corner of the three-phase field moves along the oxidation limit in the direction of the urania-rich side as the temperature increases.

Gilpatrick, et al, also studied the position of the oxidation limit itself at various temperatures. Although some of their early ORNL progress reports showed a temperature dependence of the oxidation limit, later work showed that the oxidation limit remains essentially fixed in position, at least for thoria-rich compositions, over the range studied.

Cohen and Berman (Reference 14) discussed the factors controlling the position of the oxidation limit. In the urania-rich portion of the diagram, the limit is fixed at $(U, Th)_4O_9$ apparently by structural limitations. In the thoria-rich portion of the diagram, however, the limit of oxidation is fixed by the fact that there are insufficient uranium ions which can be oxidized from U^{+4} to U^{+6}. Cohen and Berman calculated the effect of decreasing the availability of uranium on the number of sites available for accommodating interstitial oxygen. Each such site is surrounded by six nearest-neighbor cations, which may be six thoriums, five thoriums and one uranium, etc. For each composition,

it is possible to calculate the probability of the different cation environments. They found that experimental data on material at the oxidation limit corresponded to the following:

1. None of the positions surrounded by six thoriums accommodated an interstitial oxygen ion.
2. All of the suitable interstitial positions, the nearest neighbors of which include two or more uranium ions, accommodate oxygen.
3. Of those interstitial positions surrounded by one uranium and five thorium ions, 18.5 percent contain interstitial oxygen.

These criteria will permit oxidation of compositions with UO_2 content between 16 and 40 mole percent to a point where, if all the oxidation is attributed to the uranium, the average valence of the uranium can exceed +5. The maximum valence is +5.0656, attainable at $U_{0.27}Th_{0.73}O_{2.144}$. In these compositions in which the uranium valence is above +5, the lattice parameter decreases with oxidation until a minimum is reached at the point where the mean valence is +5; thereafter, the lattice parameter increases. Based on these data, U^{+5} and U^{+6} are considered separate chemical entities, each with its own Vegard's Law coefficient, in the calculation of lattice parameter from chemical composition. This calculation was discussed in Section III.

Anderson, et al (Reference 15) and Cohen and Berman (Reference 14) reported observations of a second cubic phase in high-urania oxidized samples heated to the 500 and 1000°C temperature range for long time periods. A second cubic phase has also been observed as a surface effect on ThO_2-UO_2 samples exposed to high-temperature 680°F (360°C) oxygenated water (Reference 17). Such oxidized samples consist of two cubic phases; one has a cell size corresponding to that expected for the bulk composition according to Vegard's Law, and the other has a cell size (or perhaps a pseudo-cell size) about 0.01Å smaller. Photomicrographs show a very irregular, interlocking texture of two phases. It could be argued that the two phases represent an ordered and disordered structure on the UO_{2+x} - U_4O_9 model with the small-cell material corresponding to the U_4O_9 structure. The oxidation of ThO_2-UO_2 in oxygenated water is discussed in Section IX.

C. Homogeneity

Implicit in the preceding discussion of the ThO_2-UO_2 solid solution system was the assumption that compositions in this binary system are not only

equilibrium structures but are also homogeneous. In this section, kinetic factors and processing conditions which contribute to formation of the homogeneous binary solid solution are considered.

Solid solution formation of mixed oxides can be accomplished through chemical reaction from an aqueous solution of salts of the two cation species; i.e., a co-precipitation reaction, or from a solid state reaction of the two component oxides. In the former case, a uniform distribution of the cation species in solution is achieved, and the critical problem in achieving homogeneity is to prevent segregation of the mixed oxides during the precipitation stage. In the latter case, formation of sintered bodies of mixed oxide solution has generally required two separate heat treatments, the first to initiate the process of solid solution and the second to complete the process along with forming the desired sintered body. Sintered ceramic mixed oxides for nuclear application have been fabricated using one of these two approaches. In the LWBR program, however, a single sintering cycle was used to accomplish both homogenization and sintering. Thus, it became important to assess the degree of homogeneity attained by this simplified process.

Homogeneity in a solid solution of two oxides such as ThO_2 and UO_2 is not a property; it is a condition or state. The binary ThO_2-UO_2 solid solution formed through solid-state reaction of the individual oxides tends to homogenize by diffusion processes. Given sufficient time, sufficiently elevated temperatures, and a sufficiently uniform mixture of similarly-sized individual particles of the two oxides, ThO_2 and UO_2 would form uniform solid solutions for all compositions. An absolutely uniform uranium distribution (except in pure UO_2) would require an infinite time, but it is possible to estimate a finite sintering time that would be sufficient to bring the entire range of composition within specified limits above and below the bulk or average composition. This approach was discussed in Reference 18 and is reviewed briefly below.

Berman suggested, in Reference 18, that the solid solution homogenizes as a result of many diffusion processes: volume diffusion, augmented by grain-boundary diffusion, and surface diffusion. He determined an empirical "inter-diffusion coefficient" for various times and temperatures by measuring the composition profiles in materials that were deliberately fabricated with large inhomogeneities. A combination of electron probe, x-ray diffraction, and auto-radiographic techniques was used to obtain composition profiles, gradients, and

distributions. As a result, an effective, "practical" measure of the interdiffusion coefficient was obtained which may be applied to typical sintered, polycrystalline mixtures to ThO_2 and UO_2. It may be expressed as

$$\bar{D} = 1.125 \times 10^{-5} \exp(-62{,}200/RT) \text{ cm}^2/\text{sec}$$

Further limitations must be placed on this expression; it was the result of measurements on samples in which ThO_2 served as the solvent and UO_2 as a comparatively dilute solute; compositions were in the range of 1 to 5 w/o UO_2, and, strictly speaking, the expression should be regarded as applicable only for this general range. Also, the expression represents a combination of different types of diffusion applicable to polycrystalline material with a density of approximately 98% of theoretical and a grain size in the neighborhood of ASTM #9 at temperatures in the vicinity of 2000°K. Because of the combination of diffusion processes, the expression does not represent the "chemical" or "interdiffusion" coefficient as defined by Darken (Reference 19). (See Section VII for further discussion.)

The metallic ions diffuse through a continuous fluorite-type lattice of oxygen ions which can be conceived as remaining essentially intact and extending through both the inhomogeneity and the matrix. Since the diffusion of uranium outward from the inhomogeneity is somewhat more rapid than the diffusion of thorium inward*, pores form at the high uranium margin of the diffusion zone that develops around the periphery of each UO_2 grain.

The principal method used to inspect sintered pellets of ThO_2-UO_2 for the degree of inhomogeneity consisted of making autoradiographs of polished surfaces on Kodak NTA plates. After development, the high urania segregations appear as dark spots. The spots in various size ranges are counted and the size ranges are corrected for the effect of alpha-particle range in the emulsion which increases the apparent diameter of each spot by an average of about 29 microns. Finally the total fractional area occupied by the inhomogeneities is calculated.

By a combination of autoradiography and microprobe analysis, Berman was able to quantify in terms of chemical composition the nature of inhomogeneities as revealed by autoradiography. A discussion of this work is presented in References 18 and 20.

---

*See Section VII for discussion of relative diffusion rates.

V. THERMAL PROPERTIES

A. Melting Point

In their compilation of data on thorium ceramics (Reference 1), Peterson and Curtis cite two values for the melting point of ThO_2: 3300 ± 100°C from the work of Lambertson, et al (Reference 12) and 3390°C from the work of Benz (Reference 3). In the latter work, Benz investigated the thorium-thoria system, using induction heating from a radio frequency generator with a tungsten susceptor. He delineated the liquidus and solidus in the system through metallographic examination of samples after cooling. An optical pyrometer calibrated to 2500°C was used to determine temperatures, and temperatures above 2500°C were extrapolated linearly. On this basis Benz reported the melting point of pure thoria as 3390°C with no explicit statement concerning limits of error of this value. On the other hand, Lambertson, et al, in their study of the UO_2-ThO_2 phase equilibrium system, qualified their measurements, particularly those for pure ThO_2, citing the experimental difficulties and the specific corrections for temperatures higher than 2880°C. For ThO_2 they found values from 3285 to 3555°C. Although extrapolation of the melting points of the solid solutions to pure thoria gave a value of 3350°C, Lambertson, et al suggested a lower value (3300°C) to allow for curvature near the ThO_2 end of the system to match that found near the UO_2 end. This lower value (3300°C) is in good agreement with the extrapolated value of about 3270°C made by Christensen (Reference 13) from his melting point measurements for some compositions in the ThO_2-UO_2 system. However, the assumption that the melting point-composition curves should have symmetrical curvatures at both ends of the ThO_2-UO_2 system is not warranted since loss of oxygen could be responsible for the curvature at the UO_2 rich side and this condition would not exist to the same extent at the high ThO_2 end. The "true" value is probably between that of Benz (3390°C) and the extrapolated value of Lambertson et al (3350°C). The recommended value is therefore 3370 ± 20°C, with the understanding that the ±20°C is not a true experimental error band but rather reflects the average of two numbers.

As was discussed in Section IV, stoichiometric thoria continues as a single, face-centered-cubic phase up to the melting point, at which it is in equilibrium with a liquid of the same composition, i.e., it melts congruently. Substoichiometric thorium oxide melts at somewhat lower temperatures. These changes progress approximately linearly with decreasing oxygen until the

monotectic is reached at a temperature of 2740 ± 100°C. At this temperature, a fluorite-type solid phase with a composition of $ThO_{1.87\pm0.04}$ is in equilibrium with a liquid of composition $ThO_{1.5\pm0.2}$. The composition of $ThO_{1.87}$ at 2740°C represents the highest attainable oxygen deficiency for stable cubic ThO_{2-x}.

The defined melting point of pure stoichiometric thoria (3370°C ± 20°C) is the highest known for any oxide. Accordingly, a straight line between this melting point and that of another oxide component in solid solution would have a downward slope as it moves away from the thoria composition. The magnitude of the slope, however, is uncertain as can be seen from the melting point-composition curves for ThO_2-UO_2 solid solutions as determined by Lambertson, et al (Reference 12) and by Christensen (Reference 13). (See Figure 7, reproduced from Figure 36 in Reference 1.) Shown in Figure 6-33 in Reference 11 from the work of Lambertson, et al is a comparison of the experimental solidus and liquidus with those calculated from ideal solution theory. The maximum deviation of the experimental data from the theoretical ideal solution curves is about 50°C.

The situation at the high UO_2 end of the ThO_2-UO_2 system is considerably more complicated than at the other end. For example, Latta, et al (Reference 21) criticized the work of Lambertson, et al and of Christensen and suggested different values for the solidus-liquidus temperature in the high UO_2 region of the ThO_2-UO_2 system. According to Latta, et al, the early melting point studies of Lambertson, et al and Christensen permitted exposure of the ThO_2-UO_2 specimens to the furnace environment and thus introduced uncertainties with changes in stoichiometry and preferential vaporization of UO_2*. To avoid these complications Latta, et al used specimens specially prepared to control stoichiometry and sealed them in tungsten capsules by electron beam welding. They investigated a narrow range of compositions, namely 0 to 17 mole percent ThO_2; their results are shown in Figure 8. It is clear from their results that a minimum does exist in the temperature-composition diagram but at 5 rather than at 2 mole percent as found by both Christensen and Cohen and Berman. This inconsistency between the Latta, et al thermal arrest measurements and the lattice parameter measurements may be a result of small differences in stoichiometric composition but remains unresolved. Note also that the melting point for UO_2 (2850°C) measured by Latta, et al is higher than that determined by Christensen (2800°C).

Some estimate of the effect of irradiation on the melting points of ThO_2 and ThO_2-UO_2 solid solutions can be made from the measurements of Christensen,

---

*See discussion of vaporization phenomena in Section VI.C.

et al (Reference 22) on the melting points of irradiated UO_2. These authors reported measurements of the melting points of "nearly" stoichiometric UO_2 samples that had been irradiated to various burnup levels from about 2000 to 52,000 MWD/T. Measurements were made relative to unirradiated UO_2, which was assumed to have a melting point of 2800°C. Their data indicated a nearly linear decrease of melting point with irradiation exposure at a rate of about 32°C/10,000 MWD/T or about $9°C/10^{20}$ fissions/cc ($16°F/10^{20}$ fissions/cc). Similar data for ThO_2 and ThO_2-UO_2 are not available; however, it is not unreasonable to assume a similar decrease with burnup of the melting points for ThO_2 and ThO_2-UO_2.

B. Boiling Point

Only one estimate has been made for the boiling point of ThO_2, that by Mott (Reference 23); the reported value was 4400°C. No information exists on boiling points for ThO_2-UO_2 compositions.

C. Thermal Expansion

Peterson and Curtis (Reference 1) showed plots of thermal expansion data obtained both from direct dilatometric measurements (Reference 24) and from x-ray lattice parameter measurements (References 25 to 28). The direct measurements of Reference 24 covered the widest temperature range (to about 2500°F) and, according to Peterson and Curtis, are in good agreement with other direct measurements (see Reference 1) as well as with expansion data derived from x-ray measurements (References 25 to 28). Three other sets of measurements of the thermal expansion of thoria have appeared subsequent to the compilation of Reference 1. On was a set of dilatometric measurements made at Battelle Memorial Institute (Reference 29); the other two were high temperature x-ray diffraction measurements (References 30 and 31).

The x-ray data of Hoch (Reference 30) and of Hirata, et al (Reference 31) were combined with the older data of Kempter and Elliott (Reference 25) and were fit to the equation:

$$a_o = 5.59537 + 4.62057 \times 10^{-5}T + 4.710404 \times 10^{-9}T^2 \quad ,$$

where a_o is in angstroms and T is in °C. A plot of these data is shown in Figure 9; included in this plot are the dilatometric measurements of Reference 29.

Calculation of cell sizes with percentage increases for various temperatures was made and compared with the dilatometric measurements; these data are shown in Table 7. The dilatometric measurements gave results that are significantly higher than the x-ray cell size data at temperatures above 800°C, and the difference increases systematically. This can be attributed to the accumulation of dislocations and other lattice defects, which affect the external dimensions but not the cell size.

Springer, et al (Reference 29) also reported dilatometric measurements of thermal expansion for ThO_2-10 w/o UO_2 and ThO_2-20 w/o UO_2 from 20 to 2000°C. The data for these two solid solutions and for ThO_2 shown in Table 8 differ slightly, each composition represented by a single sample. However, after the initial stage of heating (up to 400°C), the measurements follow essentially parallel curves. No phase changes or permanent length changes were noted for these materials.

D. Thermal Conductivity

An assessment of the thermal conductivity of polycrystalline thoria and of a limited range of thoria-urania solid solution compositions was issued as a Bettis report (Reference 32). This evaluation was made from data obtained by Battelle Memorial Institute (BMI) workers and reported in References 29 and 33 and also included analyses discussed in an earlier Bettis report (Reference 34). The data base consisted of a set of measurements of thermal diffusivity, thermal expansivity, and specific heat made on ThO_2-UO_2 solutions ranging in composition from 0 to 30 w/o UO_2, in temperatures from 200 to 2000°C, and in density from 90 to 98% of the theoretical value. The expansivity data were discussed above in Section III.C, and the specific heat data that were used are discussed below in Section VI.A.

The thermal diffusivity data were obtained by using the flash-diffusivity method, which is based on the transient behavior of a specimen subjected to a short-time thermal pulse incident on one side of the specimen. In the technique used by the BMI authors (Reference 29), a thin, disk-shaped specimen was placed in an isothermal zone of a furnace, and the front face of the specimen was exposed to a short-duration (about 1 millisecond) laser pulse. As the pulse travelled through the specimen, the temperature rise of the back face of the

specimen was recorded as a function of time, using an IR detector oscilloscope-camera system. The temperature-time history of the back face of the specimen was directly related to the thermal diffusivity of the specimen.

The thermal conductivity K was calculated from the measured quantities by means of the following equation,

$$K = C_p \alpha \rho$$

where C_p is the specific heat at constant pressure, α is the thermal diffusivity, and ρ is the density.

A summary of the conclusions presented in Reference 32 is reviewed below.

1. Porosity Correction

The thermal conductivity was corrected to the value K_o, the thermal conductivity of 100% dense material, through use of the Maxwell-Euckel relation,

$$\frac{K}{K_o} = \frac{1 - P}{1 + \beta P}$$

where P is the volume fraction of porosity and β is a coefficient dependent on pore shape and on the ratio γ, which is defined as the ratio of the conductivity of the pores to that of the surrounding matrix. The calculation therefore requires iteration; an estimate of the conductivity of the matrix is needed for the porosity correction in order that a better estimate of the conductivity of the oxide may be calculated.

Marino (Reference 35) derived an equation for the calculation of the coefficient β from γ and from a pore shape factor, ε. Berman et al (Reference 32) calculated that the best-fit value for ε for the set of data was 0.1637 (dimensionless). This value can be taken as representative of high-density oxides, the type of oxide for which the value of ε was calculated.

Using this value for ε, and successively estimating γ from the assumption that the gas within the pores consists primarily of CO and H_2*, the values of β in Table 9 could be calculated for ThO_2; they apply as well, to a close approximation, for the other compositions in the low UO_2 range in the ThO_2-UO_2 system, i.e., for the LWBR compositions. Inspection of Table 9 shows that, for most

*This assumption is reasonable based on the gas release results reported by Smid (Reference 36). See discussion in Section X.

purposes, β can be regarded as constant, with a value of 1.1 (dimensionless). However, this approximation was not used in Reference 32; the full correction was made in obtaining values of K_o.

2. Effect of Composition

Values of K_o for the specific ThO_2-UO_2 compositions as well as for ThO_2 were fit to the following equation,

$$1/K_o = A_o + A_1U + A_2U^2 + (B_o + B_1U + B_2U^2)T$$

where

K_o = thermal conductivity of 100% dense material, watt/cm°K

T = temperature, °K

U = mole fraction UO_2,

and the best fit-values of the coefficients are as follows:

Coefficient	$0 \leq U \leq 0.1$	$0.1\ U \leq 0.3$
A_o	0.93137	6.5219
A_1	20.830	-78.628
A_2	-281.018	213.518
B_o	0.018220	0.011585
B_1	0.034136	0.14715
B_2	0.10432	-0.36054

Solutions of the above equation for various values of temperature and UO_2 content to the experimental limit of 30 weight percent UO_2 are listed in Table 10 and are plotted in Figure 10. Figure 10 also shows the small discontinuity occurring at a value of U = 0.1 (10 mole percent UO_2) between the two sets of coefficients.

3. Phonon and Photon Transfer

For pure ThO_2, the equation above simplifies to $1/K_o = 0.93137 + 0.01822T$, the typical expression for phonon scattering where the first term is the athermal contribution and the second is the thermal contribution. Evaluation of this expression at T = 1950°C = 2223°K gave a value for K_o = 0.0242 w/cm°K, and in fact one of the ThO_2 specimens reported in Reference 32 followed the expression closely and gave thermal conductivities close to the calculated values after correction for porosity. This sample had nonuniform grain sizes, with grain

diameters smaller than 1 μm at the center of the pellet. Two other ThO_2 samples did not follow the curve, and at temperatures above 1200°C gave thermal conductivity values higher than the predicted values. The difference increased with increasing temperature, and at 1950°C, the K_o value was 0.033 w/cm°K, or 0.009 w/cm°K above the predicted value. This increase can be explained as resulting from a radiative transfer contribution to the thermal conductivity.

Pure thoria is somewhat transparent in the infrared, and therefore radiative transfer can make some contribution to the thermal conductivity at high temperatures if the grain boundaries are not so closely spaced that the energy is scattered and transformed into ordinary thermal lattice vibration. In the case of the two specimens that apparently showed the effects of radiative transfer, the average grain diameter, d, was about 15μm or 0.0015 cm (equivalent to ASTM #9). The radiative contribution to the thermal conductivity, K_r, is proportional to d and also to the cube of the absolute temperature. Thus, using the proportionality constant C_r, it is possible to write

$$K_r = dT^3C_r$$

where, in this case,

$K_r = 0.009$ w/cm°K
d = 0.0015 cm
T = 2223°K,

and the proportionality constant, C_r, can therefore be evaluated as 5.5×10^{-10} $w/cm^{-2}\ deg^{-4}$. An expression for the thermal conductivity for thoria, corrected for porosity, can be written as

$$K_o = \frac{1}{0.93137 + 0.01822T} + 5.5 \times 10^{-10}T^3d \quad ,$$

the first term being due to thermal and athermal phonon scattering and the last term being the radiative contribution. For d = 0.0015 cm, K_o reaches a minimum of 0.03313 w/cm°K at 1870°C (2143°K). As the temperature is increased above this point, the thermal conductivity increases.

A correction for the radiative contribution to thermal conductivity is valid only for pure ThO_2 and not for ThO_2-UO_2 solid solutions, since the addition of urania greatly increases the optical absorption in the infrared and thus decreases the radiative contribution to below the level of significance.

4. Effect of In-Pile Irradiation

As discussed above the thermal resistivity (the reciprocal of the conductivity) of unirradiated, 100% dense material, ignoring the radiative contribution, is

$$R_o = 1/K_o = A + BT$$

where the coefficients A and B are functions of composition. The terms A and BT can be considered, respectively, the athermal and thermal terms.

For irradiated material, according to Reference 32, two additional terms should be added to the equation for R_o:

$$R_I = R_o + C/T + DF/T$$

$$R_I = A + BT + C/T + DF/T$$

where C/T and DF/T are terms independent and dependent on burnup. Reference 32 gives the values C = 17.30 and D = 5.92 for UO_2, where F is burnup in units of 10^{20} fissions/cm^3 of fuel, R_o is thermal resistivity in cm°K/watt, and T is temperature in K.

The term C/T represents the accumulation of defects and dislocations which reaches saturation soon after the start of irradiation; the saturation point it reaches, and therefore its contribution to thermal resistivity, is inversely proportional to absolute temperature. The DF/T term represents the accumulation of fission fragments. The values given above for C and D were obtained from the data for UO_2; however, the changes with burnup, and the mechanisms of these changes, should be sufficiently similar in ThO_2 and ThO_2-UO_2 solid solutions that these coefficients can be considered applicable.

5. Effect of Cracks

Almost all irradiated samples show cracks, and the thermal resistance of these cracks is added to the thermal resistance of the fuel. Berman, et al (Reference 32) calculated this effect by postulating a unit cube of fuel, 1 cm on each edge, such that the thermal resistance is identical to the thermal resistivity, R_I. Opposite sides of the cube were designated the hot and cold side. It was necessary to add, to this postulated unit cube, cracks parallel to the plane representing the hot or cold side, which are equivalent in thermal effect to the cracks in the actual fuel sample.

These cracks will have a width w and a total area a. Photomontages of cross sections of the actual fuel can be used to determine values for a and w.

In an operating fuel element such as in the helium-filled rods of LWBR these cracks are filled with helium, plus a minor amount of the fission gases krypton and xenon, at a temperature comparable to the surrounding fuel. The thermal resistivity of helium, R_{He}, is the reciprocal of the conductivity K_{He}; it is virtually independent of pressure over a very wide range and little affected by fission-gas impurities. It may be calculated as follows:

$$K_{He} = 1/R_{He} = 1.445 \times 10^{-3} T^{0.721} \text{ w/cm°K}$$

In addition to the thermal resistance of a body of helium with area a and width w, the thermal resistance of the equivalent crack includes increments representing the thermal resistance of the two fuel-gas interfaces. Reference 32 showed that these can be appropriately evaluated by adding to w a "thermal jump distance," Δw, and performing the calculation as if the body had a width of $w + \Delta w$, and no interface effects. For typical cracks in ceramic oxide fuels, Δw has a value of 1.47×10^{-3} cm; this value compensates for both interfaces.

One more correction was suggested in Reference 32. After calculating the increment to thermal resistance caused by the helium and the two interfaces, it is necessary to subtract the resistance that would have been caused by a similar volume of porous fuel that is not present because of the crack. Accordingly the total resistivity of the fuel R may be calculated from the equation:

$$R = R_I + \frac{R_{He}(w + \Delta w) - R_I^w}{a}$$

In theory, it is therefore possible to calculate an increment of thermal resistivity appropriate to cracks, given a photograph of a typical cross-section showing the crack pattern. In practice, the thermal conductivity estimate is reduced by an appropriately conservative precentage to allow for the formation of cracks after the start of irradiation.

VI. THERMOCHEMICAL PROPERTIES

A. Thermodynamic Functions of ThO_2

Peterson and Curtis (Reference 1) prepared tables of thermodynamic properties (heat capacity, enthalpy, entropy, the free-energy function, heat of formation, and free energy of formation) of thoria, and these tabulations are

reproduced here in Tables 11 and 12. The Table 11 values up to 298.15°K were taken from the work of Osborne and Westrum (Reference 37), and those values for higher temperatures were based on the analysis given by Godfrey, et al (Reference 38) of data by Victor and Douglas (Reference 39), Southard (Reference 40), and Hoch and Johnston (Reference 41). The data on heat and free energy of formation of ThO_2 shown in Table 12 were based on the heat of formation at 25°C reported by Huber, et al (Reference 42), and thermodynamic functions of thorium, oxygen, and thoria from References 43 and 44 and Table 11, respectively. Rand summarized the various sets of thermodynamic data in Reference 42; his assessment is in essential agreement with that made by Godfrey, et al (Reference 38) and used by Peterson and Curtis (Reference 1).

B. Enthalpy and Heat Capacity of ThO_2 and ThO_2-UO_2

Springer, et al (Reference 29) made enthalpy measurements and derived specific heat (heat capacity) data for ThO_2 and two ThO_2-UO_2 solid solutions as part of their thermal property studies discussed in Section V.D. The specific heat data for ThO_2 were compared with some earlier data, and this comparison taken from Reference 29 is shown in Figure 11. Figure 12 shows a composite of specific heat curves for the three materials (ThO_2, ThO_2-10 w/o UO_2, and ThO_2-20 w/o UO_2); the specific heat varies little with the addition of UO_2 at least up to about 20 w/o UO_2. The individual specific heat data are also shown in Table 13.

Note that these specific heat data were derived from experimental enthalpy data and are therefore values for specific heat at constant pressure,

$$C_P = \left(\frac{\partial H}{\partial T}\right)_P$$

The two specific heats are related by the equation,

$$C_P - C_V = \frac{\alpha^2 V}{\beta} T$$

where

α = coefficient of thermal expansion,

β = coefficient of compressibility (reciprocal of bulk modulus),

V = molar volume, and

T = absolute temperature.

The term $(\alpha^2 V/\beta)T$ is negligibly small for the temperature range of the enthalpy measurements.

C. Vaporization Behavior

The vaporization behavior of thorium dioxide has been widely studied. A summary of some of the sets of data (References 46 to 51) was given in a log P versus 1/T plot in Reference 1, reproduced here in Figure 13. In this illustration, the two lines from Ackermann, et al (Reference 50) represent (1) vapor pressures neglecting vapor species other than $ThO_2(g)$ and (2) calculations correcting for the formation of ThO(g) and O species.

The work of Ackermann, et al (Reference 50) was, by far, the most extensive. They combined results from effusion measurements of the dioxide phase and liquid metal-dioxide mixtures and results from mass spectrometric measurements of the dioxide phase to obtain an internally consistent set of thermodynamic data. Their significant results can be summarized as follows. The solid dioxide evaporates congruently at all temperatures. Above 2800°K there is a measurable but thermodynamically insignificant substoichiometry, $ThO_{1.994}$. The vapor species include contributions from ThO(g) and O(g). The "effective" pressure is given by the equation:

$$\log P_e(\text{atm}) = 8.26 - 3.55 \times 10^4/T \quad .$$

The partial pressures of the predominant vapor species, $ThO_2(g)$, ThO(g), and O(g), in equilibrium with solid ThO_2 are as follows:

$$\log P_{ThO_2} = 7.64 - 3.44 \times 10^4/T$$

$$\log P_{ThO} = 8.70 - 3.792 \times 10^4/T$$

$$\log P_O = 8.10 - 3.792 \times 10^4/T$$

The heat of vaporization of ThO_2 was found to be 159.5 kcal/mole. In subsequent work, Ackermann and Rauh (Reference 52) revised their earlier values for the thermodynamic properties of ThO(g).

In a binary system, such as ThO_2-UO_2, with greatly different heats of vaporization for the components, the usual mode of vaporization is preferential vaporization of the component with the higher volatility. This is confirmed from the work of Alexander, et al (Reference 51), who determined the partial pressures of UO_2 over two ThO_2-UO_2 compositions, ThO_2-8 w/o UO_2 and ThO_2-20 w/o

UO_2, as well as the vapor pressures of the pure end members. Their data are shown in Figure 14 along with the Ackermann, et al (Reference 50) vapor pressure data for ThO_2 (solid).

D. Thermodynamics of the ThO_2-UO_2 System

A discussion of the limits of oxidation in the ThO_2-UO_2 system from metallographic and x-ray diffraction evidence was given in Section IV. In this section, the thermodynamic aspects are summarized.

Peterson and Curtis (Reference 1) listed the available data, which include the work of Anderson, et al (Reference 15), Aronson and Clayton (Reference 53), Roberts, et al (Reference 54), and Aitken, et al (Reference 55). The most extensive measurements of the partial thermodynamic quantities for solution of oxygen in $Th_{1-y}U_yO_{2+x}$ are those of Aronson and Clayton (Reference 53) derived from solid state electrochemical measurements; these data are listed in Table 14. These data as well as those from References 15 and 54 show that, at a fixed value of x, the oxygen potential of $Th_{1-y}U_yO_{2+x}$ increases as the uranium content decreases.

Aitken, et al (Reference 55) measured the volatilization of uranium oxide from ThO_2-UO_2 solid solutions in a stream of dry air at 1200 to 1600°C. They assumed that the uranium vaporizes as UO_3, that is, that the vaporization process can be expressed as follows:

$$U_yTh_{1-y}O_{2+x} + \frac{3\delta}{2} O_2(g) \rightleftharpoons UO_3(g) + U_{y-\delta}Th_{1-y}O_{2+x}$$

If δ is small, the amount of gas removed does not significantly change the composition of the solution, and the activity of the uranium dioxide can be determined from the partial pressures of UO_3 and O_2 gas in equilibrium with the solution. They derived the results shown in Table 15. Using these results and values of $\overline{G}_{O2}$, $\overline{H}_{O2}$, and $\overline{S}_{O2}$ from the work of Aronson and Clayton (Reference 53) and Roberts, et al (Reference 54), they constructed a curve shown in Figure 15 for the free energies of formation for the stoichiometric and nonstoichiometric solid solutions in equilibrium with oxygen at 0.2 atmosphere at 1300°C. The dashed line for the stoichiometric solid solution is for the ideal solid solution. The values of ΔG_f for $UO_{2.61}$ and $UO_{2.25}$ are extrapolated to the right hand side of Figure 15. Since there is no known solubility of ThO_2 in the U_3O_{8-z} phase, the minimum in the free energy versus composition curve for $UO_{2.61}$ occurs at y = 1. The dashed straight line drawn from the value for $UO_{2.61}$ tangent to the nonstiochiometric solid solution curve leads to the point of tangency in the

vicinity of $0.5 < y < 0.6$. For a mole fraction of uranium greater than the point of tangency, precipitation of the U_3O_{8-z} phase should occur, a result in agreement with the x-ray diffraction observations discussed in Section IV.

VII. DIFFUSION KINETICS

A. Introduction

Fick's first law, $J = -D\,\partial c/\partial x$, defines the diffusion coefficient as the constant which relates the flux of matter J to the concentration gradient causing the flow. The literature is replete with specific terminologies for various types of diffusion coefficients, but some are used interchangeably. A few definitions are therefore in order.

The terms "tracer diffusion coefficient" and "self-diffusion coefficient" refer to diffusion in the absence of a chemical concentration gradient. Thus, if an element "i" is present in only very dilute concentration in a solid of homogeneous composition and if there are no external driving forces, the concentration of "i" tends toward an equilibrium distribution as a result of the force of its own concentration gradient $\partial c_i/\partial x$. Then D is the diffusion coefficient of the tracer element "i", often symbolized by D*. If the tracer and the medium through which the tracer diffuses are the same element, for example ^{230}Th and ^{232}Th, D becomes the "self-diffusion coefficient," D_{self}. In reality, there is always a concentration gradient when, for example, element A is plated or deposited on element A or on some solid solution AB, but with a radioactive (or otherwise detectable) tracer the amount of solute added to the solvent can be so small that compositional changes can be ignored.

The term "lattice diffusion coefficient" is a general term and refers to a diffusion process within the bulk or lattice of the crystal; "bulk" and "volume" have also been used interchangeably for "lattice."

The term "boundary diffusion coefficient" (D_b) refers to diffusion along an interface or boundary, such as a grain boundary. Surface diffusion, whose coefficient is symbolized by D_s, refers to diffusion along a surface.

"Intrinsic" diffusion refers to a process in which only thermally created point defects are involved in the diffusion process, whereas "extrinsic" diffusion refers to diffusion as a result of defects produced through impurities and not from thermal energy. "Apparent" diffusion is a term used to include contributions from several diffusion paths combined into one diffusion coefficient. "Defect" diffusion refers to the diffusivity of a particular point defect, such as for example a vacancy. And finally, chemical or interdiffusion refers to

diffusion in a chemical potential gradient. In the interdiffusion of ThO_2 and UO_2, for example, the cations diffuse in a fixed oxygen lattice. Thus in a simplified way the chemical or interdiffusion coefficient represents counter-diffusion of thorium and uranium ions, which are related to the individual self-diffusion coefficients by the Darken equation (Reference 19).

$$\tilde{D} = X_2 D_1^S + X_1 D_2^S \left(1 + \frac{d \ln \gamma_1}{d \ln X_1}\right)$$

where X_1 and X_2 are the mole fractions of the diffusion species (Th and U), D_1^S and D_2^S are the respective self-diffusion coefficients and γ_1 is the activity coefficient of component 1. For an ideal and dilute solution the term $(d \ln \gamma_1)/(d \ln X_1)$ becomes zero, and the interdiffusion coefficient is the weighted average of the self-diffusion coefficients.

Note that all of these diffusion processes refer to isothermal diffusion, that is, to a migration process in the absence of a temperature gradient. "Thermal diffusion" considers the effect of a temperature gradient on the migration of a solute within a solid.

In general, there are two experimental approaches to evaluate diffusion coefficients: (1) the direct method, which measures the mass flow through a solid by determining the change in the concentration of the diffusing species as a function of distance into the solid and (2) the indirect method in which the diffusion coefficient is determined by measuring some diffusion-controlled phenomenon. There are many experimental techniques which have been used under each of these broad classifications.

A considerable body of information exists on the kinetics of diffusion processes in ThO_2, and some limited data are also available for ThO_2-UO_2. Dragoo (Reference 56) provided a tabular summary of the available data as of 1975. These data together with more recent information are reviewed in this section.

B. Volume Diffusion

1. Oxygen Self-Diffusion in ThO_2

Unlike the situation for uranium dioxide for which oxygen diffusion data are voluminous, there are only three sets of measurements (References 57 to 59) of oxygen diffusion kinetics in ThO_2. In the first of these, Morgan and Yust (Reference 57) measured the diffusion of oxygen in fine-grained 10μm diameter thoria spheres using the method of heterogeneous isotopic exchange. In this method, as used for oxygen, diffusion is measured indirectly by the exchange of

the ^{18}O isotope in either the gas or solid phase with normal oxygen of the other phase. The change in ^{18}O concentration in the gas phase is measured by analyzing samples with a mass spectrometer. This ^{18}O isotopic exchange technique was first used on a nuclear fuel material, UO_2, with CO_2 as the carrier gas for ^{18}O (Reference 60). Morgan and Yust used the same approach and carried out measurements over the temperature range 600 to 1400°C. The reported results were expressed by the Arrhenius-type equation,

$$D = 1 \times 10^{-8} \exp(-14.7 \times 10^3/RT) \text{ cm}^2/\text{sec}$$

Morgan and Yust qualified their results by stating that the absolute magnitude of the measured diffusion coefficients is uncertain because of uncertainties associated with the evaluation of the equivalent spherical diameter of the ThO_2 particles used. Another qualification can be made to their data; the very low activation energy (14.7 kcal/mole) suggests a considerable grain boundary contribution to the observed diffusion.

Edwards, et al (Reference 58) used the same ^{18}O isotopic exchange method but with coarser ThO_2 particles prepared by passing sintered ThO_2 particles through a plasma torch. Their results in the temperature range between 900 and 1500°C were represented by the equation $D = 4.4 \exp(-65.8 \times 10^3/RT)$ cm^2/sec. They interpreted the diffusion process to be intrinsic diffusion.

In the latest work on oxygen self-diffusion in ThO_2, Ando, et al (Reference 59) used single crystal ThO_2 prepared by an arc fusion process. Oxygen enriched in the ^{18}O isotope to about 5% was used as the carrier gas. They determined the amount of tracer in the solid specimen by measuring the decrease in the mass ratio 34/32 of the gas phase by means of a mass spectrometer. Experiments were performed over the temperature range 845 to 1646°C.

Ando, et al expressed their results in the form of two equations: $D = 5.73 \times 10^{-2} \exp(-49.9 \times 10^3/RT)$ cm^2/sec for the higher temperature portion of the temperature range and $D = 1.00 \times 10^{-6} \exp(-17.6 \times 10^3/RT)$ cm^2/sec for the lower temperature portion. The data show a clear break in the temperature dependence around 1200°C. (Ando, et al., stated throughout the text of their paper that the break occurs at 1100°C, but this is obviously an error.)

The results of these sets of measurements are shown in Figure 16 along with similarly-determined oxygen self-diffusion data for uranium dioxide (References 60 to 63). (The line labelled "B" for oxygen self-diffusion in UO_2 in Figure 16 was a consensus (Reference 62) of reported values made prior to publication of the Reference 63 results.) Unlike the Edwards data, the Ando data show a definite

"knee" in the Arrhenius curve, indicative of a mixture of extrinsic (lower temperature portion) and intrinsic (higher temperature portion) diffusion. This discrepency between the two sets of data (those of Edwards and Ando) is hard to explain on the extrinsic-intrinsic argument, since the single crystal ThO_2 in the work of Ando, et al has an apparent high purity but shows extrinsic diffusion, whereas the extrinsic region is not observed with the samples of Edwards, et al which seem to have a higher impurity content. Ando, et al suggest that the cause for extrinsic diffusion may not be simply attributed to point defects formed as a result of the presence of an impurity or impurities but may be due to a high density of dislocations in the single crystal material.

Nevertheless, considering the scatter of the data, the high temperature data of both Edwards, et al and Ando, et al are not only in good agreement with each other but agree reasonably well with the data for oxygen diffusion in UO_2, particularly with the data of Marin and Contamin (Reference 63). The similarities in the magnitudes of both the pre-exponential terms and the activation energies give support to the interpretation that the oxygen diffusion processes in both ThO_2 and stoichiometric UO_2 are similar. This result is not surprising since these two actinide oxides have similarities in crystal structure and physical properties.

Similar behavior has been observed for oxygen self-diffusion in $^{238}PuO_2$. Deaton and Wiedenheft (Reference 64) reported the following equation from results of isotopic exchange measurements on PuO_2 microspheres:

$$D = 1.19 \times 10^{-3} \exp(-42.2 \times 10^3/RT) \text{ cm}^2/\text{sec} .$$

The activation energy (42.2 kcal/mole) is close to the value of 49.9 by Ando, et al.

Concerning the lower temperature portion of their data, Ando, et al interpreted the activation energy for extrinsic diffusion, 17.6 kcal/mole, to be the energy required for the migration of oxygen ions in the ThO_2 lattice. On the assumption that the oxygen defects in ThO_2 are of the anti-Frenkel* type these authors calculated, following a similar calculation made by Belle, et al (Reference 61), the value of the formation energy for oxygen defects as 65 kcal/mole from the experimentally determined intrinsic and extrinsic activation energies. This value is close to that calculated by Belle, et al for UO_2 (~70 kcal/mole).

---

*A Frenkel defect consists of an interstitial atom together with a vacant lattice point or hole; a Schottky defect is a vacant lattice point only. Anti refers to the anion as the defect.

A Schottky-type vacancy can be ruled out for ThO_2 because of the large differences in the self-diffusion coefficients between the cation and anions (see Figure 16 and discussion below).

2. Thorium Self-Diffusion in ThO_2

Poteat and Morgan (Reference 65) studied the diffusion of ^{230}Th in ThO_2 over the temperature range of about 1300 to 2300°C. Diffusion coefficients were determined on single crystals, sintered powder specimens, and specimens prepared from ThO_2 sol, giving a range of grain sizes from extremely large to a few microns. An organic chelate of ^{230}Th was placed on the specimen surface and dried; the specimen was then annealed in air below 1800°C and in argon at the higher temperatures. Penetration of the isotope was determined by sectioning the specimen, by measuring the degradation in the alpha-particle energy spectra, or both. Although the diffusion coefficients represented a measure of the rate of movement of the isotope through the specimen, differentiation was not made between volume diffusion and grain boundary or some other short-circuit diffusion. The experimental data for single crystals were fit to the equation,

$$D = 2.0 \times 10^{-7} \exp(-74.0 \times 10^3/RT) \text{ cm}^2/\text{sec} ,$$

and those for sintered powder specimens were fit to the equation,

$$D = 2.6 \times 10^{-7} \exp(-69.0 \times 10^3/RT) \text{ cm}^2/\text{sec} .$$

Two distinctive features were observed: First, diffusion was increased by decreasing grain size. Second, the results indicated an increase in the diffusion coefficient as the measurement zone moved deeper into the specimens. Thus, a substantial part of the observed diffusion was believed to be grain boundary rather than lattice or volume diffusion.

Hawkins and Alcock (Reference 66) carried out diffusion studies on ThO_2 pellets of large grain size (100μm). The pellets were prepared by sintering in vacuum for 5 hours at 1900°C followed by a 4-hour anneal in vacuum at 2000°C. Presumably the pellets were of high density, but no values were given. The pellets were polished and plated with $^{230}ThO_2$ by vacuum evaporation or by evaporation of a solution containing the same isotope. Diffusion anneals were performed in vacuum, in air, and in CO/CO_2 mixtures. Alpha-ray spectrometry was used to determine the concentration of the diffusing tracer as a function of the distance below the surface.

Diffusion in ThO_2 was found to be independent of oxygen pressure in the temperature range investigated (1600 to 2100°C). Unlike their results for UO_2

which constituted the bulk of information reported in Reference 66, grain-boundary diffusion was not observed, presumably because the grains were very much larger than those in the uranium dioxide specimens. The diffusion equation for volume diffusion of ^{230}Th in ThO_2 was given as

$$D = 1.25 \times 10^{-7} \exp(-58.8 \times 10^3/RT) \text{ cm}^2/\text{sec}$$

King (Reference 67) questioned whether the data of Hawkins and Alcock (Reference 66) represent volume diffusion in the light of King's experiments on thorium diffusion (^{228}Th) in single crystal ThO_2. King developed a precision sectioning technique (Reference 68) which allowed the determination of diffusion distances as small as 0.04μm and applied this method to determine diffusion profiles in single crystal ThO_2 using the α-spectrum degradation technique. For his data, which covered the temperature range 1850 to 2050°C, King was able to separate short circuit enhanced diffusion, presumably arising from dislocations, from apparent volume diffusion. That is, at small penetration distances (x) within the single crystal, a plot of log C (concentration of tracer isotope) versus x^2 was linear, suggestive of volume diffusion, whereas at large penetration distances log C was approximately linear with distance, suggesting some short circuit path, for example, sub-grain boundaries or dislocations, for diffusion. The respective equations from Arrhenius plots were given as:

$$D_v = 0.35 \exp(-149.5 \times 10^3/RT) \text{ cm}^2/\text{sec}$$

for volume diffusion and

$$D_d\delta = 8 \times 10^{-14} \exp(-37.3 \times 10^3/RT) \text{ cm}^2/\text{sec}$$

for dislocation diffusion, where D_d is the dislocation diffusion coefficient and δ is the sub-grain boundary width. The values of the apparent volume diffusion coefficients were obtained from the slopes of the log C versus x^2 plots near the surface.

It thus appears that even in single crystal material short circuit diffusion can be an important factor in cation diffusion, at least at the temperatures investigated. King also suggested (as did Reimann and Lundy in Reference 69) that much of the data for UO_2 believed to be volume diffusion may also be suspect. The data of King for a single crystal ThO_2 and that of Reimann and Lundy (Reference 69) for single crystal UO_2 are plotted along with the oxygen diffusion data in Figure 16. Note the considerably greater mobility of the uranium cation in UO_2 compared with the thorium cation in ThO_2. The large

differences between cation and anion diffusion for both UO_2 and ThO_2 are also apparent. This result is typical for fluorite-type lattices; see, for example, results for CaF_2 (Reference 70) and for stabilized ZrO_2 (Reference 71).

3. Diffusion of Uranium in ThO_2 and ThO_2-UO_2

It can be surmised from the evidence presented above and from simple considerations that the mobility of uranium should be greater than that for thorium in ThO_2 and that the mobility of uranium should be enhanced with increase in lattice dimensions of the host lattice, since in the former case the size of the uranium (U^{+4}) cation is smaller than the thorium (Th^{+4}) cation (0.97 and 1.02Å) and in the latter case, the lattice spacing decreases from pure ThO_2 through ThO_2-UO_2 solid solution to pure UO_2. That this supposition is likely is evident from the results of Furuya (Reference 72) who was able to separate lattice diffusion from grain boundary diffusion in the case of uranium diffusion in both ThO_2 and an equimolar solid solution of ThO_2-UO_2. Furuya used ^{237}U as the tracer isotope incorporated in UO_2, which was evaporated onto the ground surfaces of high density pellets (>98% theoretical density) having an average grain size over 60μm. Gamma ray spectrometry was used to determine the amount of ^{237}U penetration. Typical penetration curves showed that the logarithm of the ^{237}U concentration varied linearly with distance in the deeper region of penetration, characteristic of grain-boundary diffusion. Near the surface, however, volume diffusion was indicated from a linear plot of the log concentration versus the square of diffusion depth. These results were similar for both ThO_2 and ThO_2-UO_2. The data are summarized in the following equations:

For volume diffusion

$$D\ (U \text{ in } ThO_2) = 1.10 \times 10^{-4} \exp\ (-76.4 \times 10^3/RT)\ cm^2/sec$$

at 1800 to 2000°C and

$$D\ (U \text{ in } ThO_2\text{-}UO_2) = 7.59 \times 10^{-4} \exp\ (-85.9 \times 10^3/RT)\ cm^2/sec$$

at 1800 to 2300°C.

For grain boundary diffusion

$$D'2a\ (U \text{ in } ThO_2) = 2.35 \times 10^{-9} \exp\ (-47.9 \times 10^3/RT)\ cm^3/sec$$

at 1800 to 2000°C and

$$D^{1}2a\ (U \text{ in } ThO_2\text{-}UO_2) = 1.04 \times 10^{-7} \exp(-64.2 \times 10^{3}/RT)\ cm^3/sec$$

at 1800 to 2300°C.

As part of a broader effort concerned with attempts to understand the mechanism of rare gas diffusion in UO_2 and ThO_2 (see Section E below), Matzke (Reference 73) measured the diffusion of ^{233}U at 1400 to 1550°C in both doped and undoped ThO_2. The materials used to dope ThO_2 were at a level of 0.1 mole percent Y_2O_3 and Nb_2O_5. The former material was added to incorporate the trivalent Y^{+3} ion, whose presence would serve to decrease the cation vacancy concentration and at the same time increase the concentration of anion vacancies. Similarly, incorporation of the pentavalent Nb^{+5} ion would be expected to increase the cation vacancy concentration and decrease the concentration of anion vacancies. On the assumption that uranium mobility in ThO_2, as well as in UO_2, proceeds by a vacancy diffusion mechanism, a decrease in the cation vacancy concentration should decrease the uranium diffusion rate in ThO_2 and an increase in the cation vacancy concentration should increase the uranium diffusion rate in ThO_2.

The experimental results confirmed the general assumptions. Diffusion coefficients for ^{233}U, calculated from plots of log C (concentration) versus X^2 (X = penetration distance) showed a considerable reduction in uranium diffusion in the Y_2O_3-doped oxide and a considerable increase in the Nb_2O_5-doped oxide.

4. Diffusion of Other Actinides in ThO2 and ThO2-UO2

Measurements were made of the diffusion of protactinium in ThO_2 and ThO_2-UO_2 in the temperature range 1800 to 2000°C by Furuya and Yajima (Reference 74) in a manner similar to that made for uranium diffusion by Furuya (Reference 72).

The evaluated diffusion equations were reported as follows:

For volume diffusion

$$D\ (Pa \text{ in } ThO_2) = 2.91 \times 10^{-5} \exp(-75.4 \times 10^{3}/RT)\ cm^2/sec$$

$$D\ (Pa \text{ in } ThO_2\text{-}UO_2) = 1.88 \times 10^{-3} \exp(-91.8 \times 10^{3}/RT)\ cm^2/sec$$

For grain boundary diffusion

$$D^{1}2a\ (Pa \text{ in } ThO_2) = 6.66 \times 10^{-11} \exp(-30.6 \times 10^{3}/RT)\ cm^3/sec$$

$$D^{1}2a\ (Pa \text{ in } ThO_2\text{-}UO_2) = 5.64 \times 10^{-8} \exp(-59.7 \times 10^{3}/RT)\ cm^3/sec$$

where D^{1} and 2a are the grain-boundary diffusion coefficient and the grain-boundary width, respectively.

5. Comparison of Activation Energies for Volume Diffusion

On the assumption that the measured diffusion coefficients for the various cations in the several host lattices (ThO_2, UO_2, and ThO_2-UO_2) indeed reflect volume or lattice diffusion, a comparison can be made of the activation energies for the various species in the host lattices. Such a comparison, shown in Table 16, indicates that, for a given diffusing species, the energetic requirements increase as the size of the unit cell of the host oxide lattice decreases. This effect is much greater than the effect of cation size.

C. Surface Diffusion

Surface diffusion, which can be described simply as diffusion in two dimensions on the surface of a solid, provides an important mechanism for the movement of bubbles in nuclear fuel materials. Nichols (References 75 and 76) presented a mathematical derivation showing that the coalescence of spherical gas bubbles should occur at a rate dependent on the surface diffusion coefficient.

Berman (Reference 77) presented results of surface diffusion measurements on ThO_2, UO_2, and ThO_2-UO_2. In this work, surface diffusion coefficients were measured using the grain-boundary grooving technique of Mullins (Reference 78). Specimens suitable for this technique were prepared by annealing high-density polycrystalline sintered pellets of the oxides in hydrogen at 1750°F for 24 to 48 hours to effect grain growth. This sample preparation tended to minimize grain growth during subsequent heat treatment when grooves were being developed.

For ThO_2 over the temperature range 1560 to 2500°C, the measurements fit the equation

$$D_S = 5.21 \times 10^{9} \exp(-Q/RT) \text{ cm}^2/\text{sec},$$

where Q is 141,900 ± 17,200 cal/mole. For the stoichiometric solid solutions, the data over the temperature range 1510 to 2050°C fit the equation

$$D_S = 8.89 \times 10^{-1} \exp(-Q/RT),$$

where Q = 51,800 + 11,100 cal/mole. Within the scatter of the data, no effect of composition between 3 and 30 w/o UO_2 in ThO_2-UO_2 solid solutions could be found. The UO_2 data over the temperature range 1525 to 1710°C were fit to the equation

$$D_S = 5.74 \times 10^{f} \exp(-Q/RT),$$

where Q = 121,400 ± 13,900 cal/mole.

The surface diffusion activation energy for the solid solutions is 51,800 cal/mole, less than half the values for either of the pure end members ThO_2 and UO_2. The value for D_o, the pre-exponential term, is many orders of magnitude less than the values for the pure end members. These drastic changes in the coefficients apparently occur between the composition of ThO_2 and ThO_2-3 w/o UO_2. The coefficients remain essentially unchanged, within the limits of error of measurement from ThO_2-3 w/o UO_2 to ThO_2-30 w/o UO_2. This surprising result has not been satisfactorily explained.

D. Thermal Diffusion

There is no information for oxygen thermal diffusion in ThO_{2-x} or $Th_{1-y}O_{2\pm x}$ analogous to the type of data obtained by Aitken (Reference 79) and by Adamson and Carney (Reference 80) for the $UO_{2\pm x}$ and UO_2-PuO_2 systems.

E. Fission Gas Diffusion

Unlike the case for UO_2, fission gas or rare gas diffusion measurements on ThO_2 or ThO_2-UO_2 are very limited. Felix, et al (Reference 81) reported results of experiments on ^{133}Xe diffusion from single crystals of ThO_2. For a temperature range of 1200 to 2000°C, they reported an activation energy (Q) of 81 ± 6 kcal/mole with the pre-exponential term (D_o) ranging from 1×10^{-4} to 2×10^{-2} on single crystal ThO_2 grown from a sodium tetraborate melt and irradiated to about 0.3×10^{7} n/cm^2 (fast). Kelly and Matzke (Reference 82) reported a tabulation of diffusion parameters for Kr and Rn diffusion in ThO_2 and for Kr diffusion in ThO_2-12 w/o UO_2. The reported activation energies were 104 ± 6 kcal/mole for krypton in ThO_2, 93 ± 6 kcal/mole for radon in ThO_2 and 110 ± 7 kcal/mole for krypton in ThO_2-12 w/o UO_2.

An attempt to gain a better insight into the mechanism of rare gas diffusion in UO_2 and ThO_2 was made by Matzke (Reference 73). In this work, which also included a study of the mechanism of cation diffusion discussed above in Section D, ThO_2 was chosen to avoid the complications associated with potential valence changes in the uranium ion when small amounts of additives of different valence (Y_2O_3 or Nb_2O_5) were added. The argument, as discussed previously, was that addition of Y_2O_3 should result in a decrease and addition of Nb_2O_5 should result in an increase in vacancy-controlled diffusion processes. The rare gas that was studied as representative of fission gas behavior was xenon, which was introduced into the ThO_2 specimens by bombardment with 40 keV xenon ions. Three different gas concentrations were achieved corresponding to intergrated doses of 8×10^{10}, 4×10^{13}, and 2×10^{16} ions/cm^2.

At the low bombardment dose, doping did not appreciably affect the gas release on subsequent annealing at temperatures from about 600 to 1800°C. This result indicated, in contrast to ^{233}U diffusion in ThO_2, that xenon does not diffuse by a simple vacancy mechanism. Temporary trapping, that is, retarded gas release, was observed at the higher levels of xenon concentration. Additions of Nb_2O_5 decreased and additions of Y_2O_3 increased this retardation effect, thus showing that impurities can affect this trapping phenomenon.

In a brief note (Reference 83) Thomas and Lindner reported some preliminary results on the diffusion of non volatile fission products in fine-grained UO_2 (0.5μm) and ThO_2 (0.2μm) powders. After irradiation of the powders, diffusion was measured by the uptake of fission products by a dry melt of NaCl under a protective argon atmosphere as a function of time. These workers stated that "the uptake of fission products by the melt followed the time law to be expected for rate determining diffusion in the grains." Results are shown in Table 17.

F. Fission Product Distribution

The distribution of fission products in irradiated UO_2 and UO_2-PuO_2 nuclear fuels has been studied by a number of investigators (References 84 to 100). In contrast to this vast effort, there is only one report of measurements of the fission product distribution in ThO_2 and ThO_2-UO_2 fuels (Reference 101).

The general findings of the work on UO_2 and UO_2-PuO_2 show that an irradiated oxide fuel contains the following phases:

1. A matrix consisting of a mixture of actinide and lanthanide oxides having the fluorite lattice;
2. Gas bubbles containing xenon and krypton;
3. Metallic inclusions containing ruthenium, rhodium, technetium and palladium, at least some of the molybdenum, and perhaps uranium;
4. Nonmetallic inclusions consisting of $BaZrO_3$ and $SrZrO_3$.

High volatile CsI and CsBr condensed in the cooler parts of the fuel element. Tellurium may also be associated with this fraction.

In the work reported on ThO_2 and ThO_2-UO_2 (Reference 101), Berman made radial electron probe traverses on irradiated ThO_2 and ThO_2-20 w/o UO_2 after approximately 15 and 21 x 10^{20} fissions/cm^3, respectively. Concentration profiles of ^{233}U and fission products in the thoria sample, which had not developed columnar grains, varied approximately linearly with the pellet radius. The slope of the profile varied with the volatility of the nuclide being measured;

for xenon the average concentration at the outside diameter of the pellet was about 6 percent above that at the center, and for molybdenum it was about 11 percent below. The slope observed for uranium did not differ significantly from zero.

When columnar grains were developed, as was the situation for the ThO_2-20 w/o UO_2 sample, much larger effects were superimposed on those described above. The region of the columnar grains was depleted of uranium and fission products, which tended to develop a parabolic composition profile with a minimum, at the center, of one-third to one-half the average content. Material removed from the columnar grains was relocated in a band at the interface between the columnar and equiaxed grains. This interface marks the outer radial limit at which the mechanism of vapor transport which is responsible for the formation of the columnar grains is effective. As the columnar grains are formed by vapor transport, the matrix material of the fuel is distilled and recondensed on the hot side of a moving pore, leaving the fission products it already contains on the cold side. (More fission products form inside the columnar grains as irradiation continues after their formation.) The result is comparable to zone refining, with a moving vapor zone rather than a moving liquid zone. As with zone refining, the impurities collect in the last portion of the "ingot" to move through the process. Technetium and the noble metals formed alloy ingots in this region with molybdenum. The composition of these ingots was not uniform, with some ingots lacking one or more of the noble metals.

VIII. MECHANICAL PROPERTIES

A. Introduction

Data on the mechanical properties of ThO_2 and ThO_2-UO_2 are reviewed and summarized in this section. An evaluation is made, where possible, of the effects of major variables such as temperature, stress, composition, porosity, and grain size. This summary is primarily a condensation of an earlier Bettis report by Wolfe and Kaufman (Reference 102); a more detailed discussion of the mechanical properties of non-irradiated nuclear oxides (UO_2 and ZrO_2-UO_2 as well as ThO_2 and ThO_2-UO_2) can be found there.

B. Elastic Deformation

The macroscopic elastic properties of polycrystalline ThO_2 and ThO_2-UO_2 can be characterized by first determining a reference set of elastic constants for

fully dense oxide at a reference temperature (25°C), and then correcting these values for the effects of porosity, temperature, and other variables by appropriate empirical or theoretical expressions.

1. Reference Properties

The elastic constants of single crystals of ThO_2 were measured by Macedo, et al (Reference 103). Their results are shown in Table 18 along with data on single crystal UO_2 obtained by Wachtman, et al (Reference 104). Both oxides are anisotropic, with UO_2 showing the greater anisotropy, and both have anisotropy factors less than one. For cubic crystals with an anisotropy factor less than one, Young's modulus varies from a maximum in the [100] direction to a minimum in the [111] direction. The Young's moduli for these directions are listed in Table 18.

The elastic moduli of randomly oriented polycrystalline oxides can be determined from direct measurements on polycrystalline samples or they can be calculated from the single crystal data. Various theoretical relations have been derived to predict the gross elastic constants of an aggregate of crystalline grains from the stiffness constants or compliance constants of an individual grain (Reference 105). Relations for calculating the bulk and shear moduli have been obtained assuming either uniform local strain (Reference 106) or uniform local stress (Reference 107). For cubic crystals the bulk modulus is the same for both the former (Voigt, Reference 106) and the latter (Reuss, Reference 107) calculations and is equal to the bulk modulus of the single crystal. The shear moduli, however, are not identical. It has been shown (Reference 108) that the Voigt shear modulus is an upper bound and the Reuss modulus is a lower bound with the true value lying between the two. Furthermore, if the orientations of the polycrystalline grains are random, the arithmetic mean of the two bounds is the best estimate of the true value. The isotropic elastic constants of the polycrystalline material can thus be calculated from the bulk modulus and the Voigt-Reuss average for the shear modulus. Elastic constants calculated in this manner for polycrystalline UO_2 and ThO_2 are listed in Table 19 along with those determined by direct experimentation on polycrystalline samples (Reference 109). The polycrystalline samples were fabricated by sintering and contained at least 3 percent porosity so that it was necessary to determine first the effect of porosity at 25°C and then extrapolate to zero porosity. Wolfe and Kaufman (Reference 102) used only those experimental results with sufficient data for a reliable extrapolation; these are included in Table 19.

Elastic constants of fully dense, polycrystalline ThO_2 were reported by Spinner, et al (Reference 109) from an investigation of the effect of porosity on elastic constants of this material. Their results, included in Table 19, were obtained by fitting the data to a quadratic equation,

$$E_R = E_S(1 + aP + bP^2) \quad , \qquad \text{(Eq. 2)}$$

where P is volume fraction porosity, E_R is Young's modulus at 25°C for porous material, and E_S is Young's modulus for fully dense solid at 25°C obtained by extrapolating to zero porosity. Wolfe and Kaufman showed, however, that better agreement could be obtained with the values calculated from the single crystal data if the data of Spinner were fit by a linear expression; this is shown in the next section. Because of the close agreement, either the Spinner values (linear extrapolation) or the values obtained from single crystal data can be used for fully dense ThO_2.

There are no data on elastic constants for ThO_2-UO_2 solid solutions, but an estimate can be made of the variation of bulk modulus with composition from a correlation by Anderson (Reference 110). Anderson proposed, primarily on the basis of empirical surveys, that the bulk moduli of crystalline solids can be correlated with specific volume, regardless of whether a change in volume results from temperature, pressure, or compositional effects. Thus, for many solids

$$K_R = \text{const} \times V^{-k} \qquad \text{(Eq. 3a)}$$

where K_R is the bulk modulus at ambient temperature, V is specific volume, and k is a coefficient that varies with crystal type and is predicted to have a value of 4/3 for ionic crystals. The observed empirical values of k are 1 for alkali metals, alkali halides, and zinc blend type compounds; 4/3 for covalent semiconductor materials; and between 3 and 4 for oxides of lighter elements. A correlation between the bulk moduli and specific volumes of ThO_2 and UO_2, based on this equation, gives a value of 1.41 for k, close to the 4/3 predicted for ionic solids. In this calculation, the cubes of the lattice parameters for ThO_2 and UO_2 (see Table 5) were used for the specific volumes of ThO_2 and UO_2, and the bulk moduli, taken from Table 19, were 1930 kilobars for ThO_2 and 2127 kilobars for UO_2. If Vegard's law is assumed the bulk modulus can be related to the lattice parameter, using a value of 1.41 for k as determined from the end members of the ThO_2-UO_2 system. The expression for the modulus becomes

$$\log K_x = 6.449 - 4.23 \log a_x \qquad \text{(Eq. 3b)}$$

where K_x is the bulk modulus at room temperature in kilobars for a ThO_2-UO_2 oxide of given composition and a_x is the lattice parameter for the same composition.

2. Effect of Porosity

The elastic moduli decrease with increasing amounts of porosity in a manner that depends not only on the amount but also on the type and distribution of the porosity. An extensive investigation of the effect of porosity on the elastic moduli of ThO_2 was carried out by Spinner, et al (Reference 109). Their samples were fabricated by isostatic pressing followed by sintering at 1750°C for 17 hours. The variation in porosity was achieved by either varying the ThO_2 particle size or using an additive which burned out during sintering. The total of 293 samples consisted of three groups with the following characteristics:

Group	Particle Size (microns)	Additive (%)	Porosity (%)
I	less than 2	6 to 30	8.0 to 33.4
II	2 to 4	6 to 36	12.3 to 39.4
III	2 to 44	0	3.7 to 26.2

They found good agreement between the data of Groups II and III, but the data of Group I were significantly lower. This the authors attributed to a greater departure from spherical porosity in the samples of Group I.

Young's modulus as a function of porosity is shown in Figure 17 with the data points representing subgroups of samples with nearly the same porosity. Included are data for a cold-pressed and sintered ThO_2 sample (Reference 111), and for a hot-molded sample (Reference 112). The data are represented in Figure 17 by a linear equation from least squares analysis of the data of Groups II and III and the zero porosity point obtained from single crystal data. It is seen from Figure 17 that (1) there is very good agreement between the data of Wachtman and Whittemore and the data of Groups II and III; (2) there is excellent agreement between the single crystal prediction for zero porosity (2497 kilobars) and the extrapolation of the linear least squares equation to zero porosity (2491 kilobars); and (3) a linear relationship gives a good fit to the data, excluding Group I, particularly in the range of interest for sintered oxide fuel materials, that is, less than 30 percent porosity. That a linear equation is equally applicable to the shear modulus data is shown in Figure 18. Again the

data from Group I were excluded from the least squares analysis. The equations obtained in this manner for the data of Figures 17 and 18 are

$$E_R = 2491\ (1 - 2.21\ P) \qquad \text{(Eq. 4)}$$

$$G_R = 969\ (1 - 2.12\ P) \qquad \text{(Eq. 5)}$$

for the Young's modulus and shear modulus, respectively.

The porosity dependence of the bulk modulus and Poisson's ratio can be determined from Equations 4 and 5 and the general relations for isotropic solids. Poisson's ratio is given by the relation

$$\mu = \frac{E}{2G} - 1 \qquad \text{(Eq. 6)}$$

Combining Equations 4, 5, and 6 gives the following relation for the porosity dependence of Poisson's ratio of polycrystalline ThO_2,

$$\mu_R = \frac{E_S}{2G_S} \times \frac{(1 - 2.21\ P)}{(1 - 2.12\ P)} - 1 \qquad \text{(Eq. 7)}$$

where E_S and G_S are the moduli for zero porosity material at 25°C. The data are compared in Figure 19 with the curve described by this equation. A reasonably good fit is observed, again excluding the data for Group I, particularly at porosities less than 25 percent. Poisson's ratio decreases with increasing porosity because the rate of decrease is greater for Young's modulus than the shear modulus, as shown by the magnitudes of the slopes of Equations 4 and 5. Although quantitative expressions are not included here for the data of Group I, it is evident that the relative rate of decrease of Young's modulus, compared to the shear modulus, is even greater for this material.

The lack of agreement of the data of Group I with those of the other two groups was considered by Spinner, et al (Reference 109) to be related to a greater departure from spherical porosity and the possibility of more open porosity in the Group I samples. The absence of metallographic evidence does not allow a more quantitative comparison of results with microstructure. Note also that, while the data (other than that of the Group I samples) are well fit by Equations 4 and 5, these correlations were made from data obtained on samples with a particular type of porosity and cannot be used to predict ThO_2 properties without considering the type of porosity involved. However, it is expected that the influence of the type of porosity will increase with increasing porosity.

3. Temperature Dependence

The effects of temperature on the elastic moduli of a polycrystalline solid are characterized by three main features. First, the derivative of an elastic modulus with respect to temperature approaches zero as the temperature approaches absolute zero. Second, it has been observed for many materials, both metals and non-metals, that at elevated temperatures the elastic modulus decreases approximately linearly with increasing temperature. Third, at still higher temperatures the dynamic elastic modulus begins to decrease more rapidly than the linear extrapolation. This latter effect results from stress relaxation at grain boundaries.

Consider first the elastic constants of ThO_2 and UO_2 at temperatures at which grain boundary relaxation is not significant. Wachtman, et al (Reference 111) proposed that the transition from linear behavior at elevated temperature to zero slope at absolute zero can be described by an empirical function of the form

$$\frac{E_T}{E_R} = \frac{E_o}{E_R} - \frac{B}{E_R} T \exp(-T_o/T) \qquad \text{(Eq. 8)}$$

where E_o is Young's modulus at absolute zero; T_o and B are empirical parameters with the significance that T_o is a characteristic temperature, and B is the slope (dE/dT) at high temperatures where the term $\exp(-T_o/T)$ approaches one; E_T is Young's modulus at temperature T; and E_R is Young's modulus at a reference temperature, usually 25°C. It has since been shown (Reference 113) that Equation 8 can be derived from theory. However, this equation actually describes the temperature dependence of the bulk modulus rather than Young's modulus as proposed by Wachtman, and should be applicable to Young's modulus only for those materials for which the variation of Poisson's ratio with temperature is small. To test the applicability of this equation, Wachtman measured Young's modulus on single-crystal Al_2O_3 and polycrystal Al_2O_3, MgO, and ThO_2 at temperatures from -200 to 580°C by means of a dynamic resonance technique and found that Equation 8 gave a very good fit to the data. The ThO_2 sample, which was fabricated by cold pressing and sintering, had a density of 90.7 percent of theoretical.

Young's modulus for this sample at 25°C (1997 kilobars) was previously shown (Figure 17) to agree well with other data for ThO_2. The temperature dependence of ThO_2 sample was found to be

$$\frac{E_T}{E_R} = 1.0223 - 1.367 \times 10^{-4} \exp(-181/T) \qquad \text{(Eq. 9)}$$

with E in kilobars and T in °K.

Spinner, et al (Reference 114) made an extensive investigation of the effect of temperature on elastic constants of ThO_2 in the range 25 to 1300°C. They measured both the shear modulus and Young's modulus by a dynamic resonance method. The samples were from the same batch that was used for the investigation of the effect of porosity (Reference 109) and included porosities from 3.7 to 39.4 percent. Their results were typical of polycrystalline samples for temperatures of 25°C and above. There was an approximately linear decrease in modulus up to a higher temperature (about 1100°C) where the rate of decrease became more rapid. Rather than describe the data with a linear equation, they compared the results with the temperature dependence observed by Wachtman, that is, Equation 9. Included in the analysis were the Young's modulus values from room temperature to 600°C, which was about the maximum temperature of Wachtman's investigation. Assuming the same characteristic temperature, 181°K, they obtained the following equation:

$$\frac{E_T}{E_R} = 1.0230 - 1.405 \times 10^{-4} \exp(-181/T) \quad . \qquad \text{(Eq. 10)}$$

When compared with Equation 9 it is seen that the value of B/E_R (1.405×10^{-4} °K^{-1}) is somewhat higher for the data of Spinner. This was attributed to differences in experimental technique and a small effect of porosity on the rate of decrease of E with temperature. Because Equation 10 represents a wide range of porosities, it is considered more appropriate for a general reference equation.

Since the temperature range of interest for oxide fuel materials is room temperature and above, it is satisfactory, and more convenient, to describe the temperature dependence of Young's modulus by a linear equation. This can be done for Spinner's data by finding a linear equation having the same slope as the limiting slope of Equation 10. The linear equation will have the form

$$\frac{E_T}{E_R} = C + 1.405 \times 10^{-4} (T - T_R) \qquad \text{(Eq. 11)}$$

where C is a constant giving the estimated value of E_T/E_R at the reference temperature, T_R. If Equations 10 and 11 are solved simultaneously at 600°C, the result is

$$\frac{E_T}{E_R} = 1.003 - 1.405 \times 10^{-4} (T - 298) \quad . \qquad \text{(Eq. 12)}$$

For applications above room temperature, the linear Equation 12 is satisfactory up to the temperature where grain boundary effects become significant. As will be shown later, this temperature is not well defined but occurs at about 1100°C for the data of Spinner.

Additional investigations of the effect of temperature on the elastic constants of ThO_2 have been reported (References 115 to 118). In some of these the material studied was ThO_2-0.5 w/o CaO. From a study (Reference 119) of the sinterability of ThO_2, it was observed that densification could be greatly enhanced by the addition of 0.5 to 1 percent CaO. Consequently, much of the literature on ThO_2 includes properties obtained on ThO_2 with CaO additions to achieve high density. In Figure 20 are shown the combined results of the effect of temperature on the relative modulus, M_T/M_R, where M designates the modulus, either E or G. In general, these data show the expected behavior of an approximately linear decrease up to the point where the modulus begins to fall off rapidly. For ThO_2-0.5 w/o CaO, the data of Wachtman and Lam agree well with the results of Lang and Knudsen (Reference 118). The addition of 0.5 w/o CaO exerts only a small effect, if any, on elastic properties. The temperature at which grain boundary effects become appreciable is about 1100°C for the dynamic measurements of both Spinner on ThO_2 and Wachtman and Lam on ThO_2-0.5 w/o CaO. It is expected that this break should occur at a lower temperature for static moduli, and this is observed. It should be noted that the composition of the material investigated by Wygant is uncertain, being reported as approximately 98 percent ThO_2. This may account, in part, for the lower moduli of this material since any impurities or additives that enhance grain boundary sliding will lower the temperature at which the break in linearity occurs.

Spinner, et al (Reference 114) observed that the temperature dependency was the same for both the shear modulus and Young's modulus. That is, Equation 10 (or Equation 12) can be used to describe either the shear or Young's modulus, with the use of the appropriate reference modulus. This means that

Poisson's ratio was found to be independent of temperature in the full range investigated, 25 to 1300°C. A similar result was found for ThO_2-0.5 w/o CaO (Reference 118). In fact a single symbol was used in Figure 20 for both E_T/E_R and G_T/G_R for the data of Lang and Knudsen, since the two relative moduli nearly coincide at any measurement of temperature. This lack of a temperature dependence for Poisson's ratio accounts for the fact that the Young's modulus for ThO_2 obeys Equation 8.

4. Effect of Grain Size

Except at temperatures where grain boundary relaxation is important, the grain size does not affect the elastic moduli (Reference 120). At high temperatures, where relaxation occurs, the apparent Young's modulus determined at a given frequency decreases more rapidly with temperature for smaller-grained material as discussed previously. In addition, the composition (impurity content) of the grain boundary can influence the extent of grain boundary sliding at the elevated temperatures. These grain boundary effects have not been quantitatively evaluated for any nuclear oxide.

C. Plastic Deformation

1. Crystallography of Slip

Investigations of the crystallographic modes of slip in compounds having the fluorite structure have included CaF_2 (References 121 to 123), BaF_2 (Reference 124), UO_2 (References 125 and 126), and ThO_2 (Reference 127 and 128). The results of these experiments can be summarized as follows. The slip direction was found to be <100>. The primary slip planes were found to be {100} with the {100} planes becoming active at elevated temperatures. There is also evidence that slip occurs on {111} planes at high temperatures in both UO_2 (Reference 125) and ThO_2 (Reference 128).

The slip deformation modes of ThO_2 single crystals were investigated by Edington and Klein (Reference 127). They used etch pit techniques to study slip line traces on {111} cleavage faces of single crystals that were deformed either by compression at 900°C or by means of hardness indentations made from room temperature to 900°C. They found that slip occurred on {100} planes in this temperature range. Electron microscopy of slip bands in thin foils produced by cleavage indicated the slip direction to be <110>.

Evidence of slip on {111} and {110} planes in ThO_2 at 1600°C was reported by Gilbert (Reference 128). The specimens were platelets of ThO_2 that were removed from the fracture surfaces of W-5 Re-2.2 ThO_2 tensile specimens tested at room temperature. The thoriated alloy containing 2-micron diameter ThO_2 particles had been cross-rolled at 1600°C to sheet, from which the tensile samples were machined. During rolling at this elevated temperature, the ThO_2 particles had been reduced to platelets approximately 0.1 micron thick. From electron transmission micrography and electron diffraction examination, information on cleavage and slip modes was obtained. Of the nine platelets investigated, three showed evidence of slip in the form of dislocations arranged along slip bands. Trace analysis of these planes showed that two were {111} and one was {110} type. No evidence of {100} slip was observed in this investigation.

2. Plastic Flow - Single Crystals

The ductility of oxide crystals depends on the type of crystal structure. Single crystals of MgO, which is an ionic solid with the rocksalt (cubic) structure, are ductile at room temperature. Single crystals of oxides with more complex crystal structures and covalent bonding, for example Al_2O_3 and TiO_2, are brittle at room temperature and show significant ductility only at elevated temperatures. The yielding and flow properties of single crystals of fluorite-type oxides are not well characterized. Other fluorite-type compounds have been found to be brittle at room temperature, but show ductility and plastic flow at moderate temperatures.

It can be expected that single crystals of UO_2 and ThO_2 will be brittle at room temperature with a transition to ductile behavior at elevated temperature when yielding on the {100} planes occurs, with the temperature of transition depending on strain rate. It should occur at a higher temperature for ThO_2 than for ThO_2-UO_2 solid solutions or UO_2 because of the higher melting point for ThO_2. Rapperport and Huntress (Reference 125) noted plastic flow of UO_2 single crystals at 700°C, primarily on {100} planes, but no lower limit was determined for plasticity. As expected, the {110} planes, and possibly {111} planes, become active at higher temperatures, in the range of 1275°C and above.

3. Plastic Flow - Polycrystals

Even at temperatures where single crystals exhibit plastic deformation, polycrystalline samples may fracture in a brittle manner. For example, polycrystalline MgO is brittle at room temperature, although it is ductile in single crystal form.

A brittle-ductile transition at 1500°C was reported for ThO_2 from compression measurements in the range 1100 to 1900°C (Reference 129). This temperature is about 0.5 T_m for ThO_2, where T_m is the melting point in degrees Kelvin. The brittle-ductile transition temperature for UO_2 is reported (Reference 1) as 1250 to 1500°C; if the lower temperature is assumed, the transition temperature is also about 0.5 T_m. Thus, it appears that the brittle-ductile transition occurs at about the same homologous temperature for polycrystalline UO_2 and ThO_2.

4. Hardness

The hardness of a material is a measure of its resistance to deformation. For most purposes, it is determined from the load and the size of the indentation impressed into the material by means of a hard indenter. For conditions where a suitable hard indenter is not available, such as at high temperatures, mutual indentation of two pieces of the subject material is an alternate method.

a. Room Temperature Hardness - The microhardness of high density (99 percent theoretical density) ThO_2-0.5 w/o CaO was reported (Reference 117) to be 640 KHN (500 g). This value is the same as that reported by Bates (Reference 130) for UO_2 and is in fair agreement with the value of 666 ± 14 KHN given in Reference 11. However, in more recent work Smid (Reference 131) reported the hardness of high density (98 percent theoretical density) ThO_2 pellets as 760 KHN (1 kg), which is appreciably higher than the other values.

b. Hot Hardness: Pyramid Indentation Hardness - Vickers hardness measurements have been made on ThO_2, UO_2, and ThO_2-8 w/o UO_2 with sapphire indenters in vacuum up to 1000°C (Reference 102); on UO_2 with a W_2C indenter in vacuum up to 1400°C (Reference 132); and on ThO_2 and ThO_2-UO_2 solid solutions for compositions containing 6, 13, 20, and 30 w/o UO_2 over a temperature range of 1000 to 1800°C in vacuum with a TaC indenter (Reference 133).

Shown in Figure 21 from the work of Wolfe and Kaufman (Reference 102) is a plot of the logarithm of the Vickers hardness number (VHN) against homologous temperature (T/T_M)*. It is seen that (1) the hardness decreases with increasing temperature; (2) there is evidence that the hardness is about the same for high density UO_2 and ThO_2 at equivalent temperature; and (3) the ThO_2-UO_2 solid solutions have higher hardnesses than ThO_2, particularly at intermediate temperatures.

---

*Note that Wolfe and Kaufman (Reference 102) used values of 2800°C and 3277°C for the melting points of UO_2 and ThO_2, respectively, for their plot shown in Figure 21. This review has suggested that 2850°C and 3370°C are more accurate values. However, this does not affect the basic conclusions derived from the data in Figure 21.

The data points from the investigation of Koester, et al (Reference 133) for ThO_2 and ThO_2-UO_2 oxides were too numerous to be included in Figure 21; therefore, only the average values for ThO_2-6, -13, -20, and -30 w/o UO_2 were shown. More detail can be found in the original report (Reference 133) and also in Figure 22, which shows the variation in hardness with UO_2 content. The hardening effect of the UO_2 becomes less with increasing temperature and is relatively small at 1800°C. Below 1200°C there is an apparent hardness peak at about 6 w/o UO_2.

c. Hot Hardness: Mutual Indentation Hardness - The mutual indentation hardness (MIH) is defined as the applied load divided by the projected area of the indentation which is formed between two specimens of the same material loaded orthogonally. The hardness number depends not only on the properties of the material, but also on the applied load, the type of specimen (whether cylinders or wedges), the size of the specimens (the diameter of cylinders or the included angle or wedges), and the rate of loading. It is necessary, therefore, to describe the conditions of testing when reporting MIH values.

MIH measurements made on two batches of high density ThO_2 at temperatures from 1000 to 2000°C were reported in Reference 102. The samples were cylinders with a diameter of 0.167 inch and the time of loading was 10 seconds. Results are shown in Table 20. Batch 2 generally showed lower hardness values for equivalent temperatures and loads, probably as a result of the larger grain size.

d. Correlations between Hardness and Stress-Strain Properties - Tabor and coworkers (Reference 134) derived empirical correlations, substantiated in part by theory, between indentation hardness numbers for metals and flow stresses determined by uniaxial testing. The relationship for Vickers hardness is

$$VHN \cong 3\sigma_o \qquad \text{(Eq. 13)}$$

where σ_o is the flow stress at 0.08 true strain. The relationship for mutual indentation of crossed cylinders is

$$MIH \cong 2.3\sigma_o \qquad \text{(Eq. 14)}$$

where σ_o is the flow stress for a true strain given by

$$\varepsilon = 0.27\ d/D \qquad \text{(Eq. 15)}$$

where d is the indentation diameter and D is the sample diameter. For fully work-hardened materials, the flow stress is equivalent to the yield stress.

While these relationships are applicable for metals (copper, aluminum, steel, and a tellurium-lead alloy), they do not necessarily hold true for ceramics. For example, it was shown (Reference 135) that, for ceramics with a rock-salt structure, the coefficient in Equation 13 is 35 rather than 3. Thus, these relationships should be applied to nuclear oxides with some caution. An analysis of the available data indicates, however, that these equations are at least approximately applicable to ThO_2, and presumably other fluorite-type oxides as well, as discussed below.

Atkins and Tabor (Reference 134) have also shown that the mutual indentation hardness of crossed cylindrical specimens is related to the sample and indentation diameters by

$$MIH = \frac{4W}{\pi d^2} = \frac{4A}{\pi}\left(\frac{d}{D}\right)^{n'} \qquad \text{(Eq. 16)}$$

where W is the applied load, A is a material constant, and n' is the work hardening coefficient. For constant sample diameter, the work-hardening coefficient can be obtained from the slope of a plot of log W versus log d. The work-hardening coefficients determined in this manner from the data of ThO_2 Batch 1 (Table 20) were 0.40 (1000°C), 0.40 (1250°C), 0.91 (1515°C), 0.49 (1800°C), and 0.12 (2000°C). Work-hardening coefficients could not be determined from the data for Batch 2 because a tendency for crack formation limited the range of loads that could be used.

The variation of work hardening for ThO_2 as a function of temperature can be compared with that calculated from the compressive yield stress-strain data for polycrystalline CaF_2 (Reference 121). The CaF_2 data were fit to a curve of the form $\sigma = K\varepsilon^n$, and the results are shown in Figure 23, where values of n are plotted vs T/T_m from the CaF_2 data along with the values of n for ThO_2 determined from mutual indentation hardness testing. As shown, the values of CaF_2 are described by a straight line at temperatures between 0.30 and 0.43 T_m/T and are mildly temperature dependent. The ThO_2 data are displaced higher than the CaF_2 data, implying that, for a given homologous temperature, ThO_2 has a higher work hardening coefficient. The ThO_2 data are approximated by the dashed line, since the results obtained at 1500 and 1800°C gave high values for n. Comparison may not be appropriate because of inaccuracies in determining the work hardening exponent and because of the effect of strain rate or loading rate. The CaF_2

data were obtained at a constant strain rate of 0.9 hr^{-1}, whereas the minimum strain rate is estimated to be approximately 15 to 30 hr^{-1} for mutual indentation hardness testing. The actual strain rate may, in fact, be much higher if indentation takes place in a fraction of the total loading time of 10 seconds. It has been shown that the indentation diameter resulting from mutual indentation is a function of the loading rate (Reference 136). Thus, the results have an additional uncertainty, since the loading rate was not controlled.

A comparison was made (Reference 102) between compressive strengths for ThO_2 and flow stresses determined from the two types of indentation hardness tests, using equations of the form given in Equations 13 and 14.

The ThO_2 mutual indentation hardness data of Batch 2 were extrapolated to a value of d = 1.26 mm, corresponding to a value of $\varepsilon = 0.08$, using Equation 15 and the estimated work-hardening exponent for ThO_2 at the appropriate value of T/T_m from Figure 23. These corrected data are shown in Table 21 along with Vickers hardness data obtained on pellets from the same batch, and compressive yield stress data obtained from other ThO_2 samples. Average correlation factors of 3.0 for the Vickers hardness and 2.0 for mutual indentation hardness rather that 2.3 were obtained from these data, and the results are plotted in Figure 24. The good agreement may be fortuitous because of some uncertainties. The hardness test samples had a larger grain size than the compression test samples and, therefore, should have a lower yield stress. This means that the correlation factors should be higher than those used. However, since the effect of grain size on yield stress has not been determined, the magnitude of the difference cannot be estimated.

e. Effect of Irradiation - There is no information on the effect of irradiation on the hardness of ThO_2 or ThO_2-UO_2, but there are some data for UO_2 (see Reference 102) which would suggest a similar behavior. The room temperature hardness of UO_2 is increased by exposure to neutron irradiation as shown by the Knoop microhardness data for irradiated single crystal and polycrystalline samples. Significant amounts of hardening are observed at low exposures with the hardness increasing with increasing exposure. The increment of hardness increase depends on the type of microstructure and the temperature of irradiation, in addition to total burnup. Bates (Reference 130) found that the average microhardness across the transverse section of an irradiated UO_2 pellet (initial hardness of 93.2% TD pellets was 600 KHN) was 800 KHN in the region where no

grain growth occurred, 770 in the region of small columnar grains, and 700 in the region of large columnar grains. It was postulated that the lower hardness in the higher-temperature columnar region was due to recovery effects. The irradiation-induced increase of approximately 33 percent in the region of no grain growth agrees well with the unpublished observations of Padden at Bettis who found a 33 percent increase in hardness of a high density UO_2 pellet (97 percent TD) after irradiation at 450°C to 2 x 10^{20} fissions/cm^3.

D. Creep Deformation

At high temperatures the time-dependent strain that constitutes permanent deformation of a solid under conditions of constant load, or constant stress, generally has the following characteristics. After an instantaneous strain upon load application, the creep curve shows three different regions or stages. The first stage, known as primary or transient creep, usually is characterized by a continually decreasing slope or creep rate. The second stage, known as secondary or steady-state creep, is a linear region with a constant, minimum creep rate. With continued deformation, the rate begins increasing again in the third or tertiary stage, which is terminated by fracture. While all three stages have been observed in the deformation behavior of oxides, the primary effort has been on the investigation of factors affecting steady-state creep. No quantitative characterization of primary or tertiary creep has been made for any oxide, and consequently these stages of creep are not included in the following discussion.

1. Steady-State Creep

The temperature creep of oxides has been found to be best described by an equation of the form

$$\dot{\varepsilon}_s = A\sigma^n \exp(-Q/RT) \qquad \text{(Eq. 17)}$$

where $\dot{\varepsilon}_s$ is the steady-state creep rate, A is a material-dependent parameter, σ is the applied stress, n is the stress exponent, and Q is an apparent activation energy. Both A and n depend strongly on the mechanism that dominates the deformation process, and a change in primary mode of deformation can alter these parameters significantly. For high temperature creep, the apparent activation energy is less affected by change in deformation mode and is usually found to be similar to the activation energy for self-diffusion of the more slowly diffusing species.

Three types of deformation can contribute to the overall, high-temperature creep; these are (1) diffusional (Nabarro-Herring) creep, (2) dislocation motion, and (3) grain boundary sliding. Boundary sliding alone cannot account for gross deformation without some accompanying intragranular deformation by one of the other two modes to maintain continuity among grains during deformation. It is probable that all three mechanism occur simultaneously to some extent.

Investigations of the steady-state creep properties of oxide fuels have involved a variety of materials, fabrication procedures, and testing methods, including bending, compression, and tension testing. The results for UO_2, UO_{2+x}, and UO_2-base mixed oxides have been reviewed (Reference 102) and are not discussed here.

The creep properties of ThO_2 were measured by compression testing in two separate investigations. Poteat and Yust (Reference 137) used constant load compression tests to determine creep rates at temperatures of 1400 to 1800°C with initial stresses from 2000 to 15,000 psi. Their specimens were fabricated by isostatic pressing at 35,000 psi and air sintering for 2 hours at 1800°C. The average grain diameter of these specimens was 10 microns and the density was 97.5 percent of theoretical. Most of the porosity was in the form of fine pores, less than one micron in diameter, located at grain boundaries. Additional data on creep of ThO_2 were obtained by constant stress compression testing at Bettis (Wolfe and Kaufman, Reference 102). The samples used in this investigation were fabricated by cold pressing and sintering; the density was 98.5 percent of theoretical. Data were obtained on as-sintered samples with an average grain diameter of 15 microns and on samples with an average grain diameter of 220 microns obtained by annealing at 2300°C for four hours in a helium atmosphere.

The results of these two investigations are summarized in Figure 25, which shows the stress dependence of the steady-state creep rates. The fine-grained material exhibited approximately linear stress dependence out to 11,000 psi, with evidence of a transition at higher stresses. There is reasonably good agreement between the results for the fine-grained materials of the two investigations. The somewhat lower creep rates of the specimens with 15-micron grains is expected, since the larger grain size and higher density of this material would both tend to decrease creep rates relative to the material with 10-micron grains. While the stress dependence of the latter material was approximately linear, the stress exponent was greater than one and was found to increase with increasing temperature

from a value of 1.04 at 1430°C to 1.59 at 1790°C. The coarse-grained material showed a much higher stress dependence, having a stress exponent of about four. At lower stresses, the coarse-grained material had significantly lower creep rates than the fine-grained material at equivalent temperatures. However, extrapolation to higher stresses would indicate the coarse-grained material to be more plastic. This same behavior was reported previously for UO_2 (see Reference 102).

The effect of temperature was determined by Poteat and Yust and is shown in Figure 26. From these results they reported an activation energy of 112 ± 7 kcal/mole. This is actually an average value since, as evident in Figure 26, the activation energy increases with increasing stress, from 104 kcal/mole at 4000 psi to 118 kcal/mole at 11,000 psi. This variation of apparent activation energy with stress results from application of Equation 17 to describe the data. This equation shows that the apparent activation energy will vary with stress if the stress exponent varies with temperature, as in the case of the data shown in Figure 25. This does not mean that the data must represent a single thermally activated process with a stress-dependent activation energy, since several mechanisms probably contribute to the temperature dependence of the deformation. Comparison of this measured apparent activation energy for creep (112 ± 7 kcal/mole) with that for "true" self-diffusion in single crystal ThO_2 (see Section VI, where an activation energy of 149.5 kcal/mole for cation self-diffusion in ThO_2 is reported) suggests that the high temperature steady-state creep of ThO_2 may be partially controlled by cation diffusion.

The stress dependence shown in Figure 25 indicates that, in the range of stresses and temperatures investigated, the coarse-grained material (220-micron grains) deforms primarily by dislocation motion. The mode or modes of deformation for the fine-grained material are uncertain. Poteat and Yust observed both grain boundary sliding (shifting in surface scratches at grain boundaries) and void formation at grain boundaries. The voids appeared to form first as a necklace type of porosity at boundaries aligned parallel to the compression axis with these pores becoming interconnecting to form cracks. Density measurements showed that about 3 percent decrease in density for 10 percent deformation was associated with this pore and crack formation. They attributed the deformation to grain boundary sliding with pore growth resulting from local Nabarro-Herring type diffusion currents at the grain boundaries. The deviation of stress

dependence from linearity and the increase in stress exponent with temperature was attributed to intragranular deformation by dislocation motion with increasing contributions from this mode of deformation as the temperature increases.

It is also possible that nonlinearity of stress dependence for the fine-grained ThO_2 results from grain boundary porosity. Creep rates are increased by the presence of porosity, particularly grain boundary porosity, as shown by the work on UO_2 (Reference 102). For the fine-grained ThO_2, increasing the temperature gave higher creep rates and higher total strains in the samples; consequently, there would be greater intergranular pore and void formation at the higher temperatures. This strain-generated void formation should itself result in increased creep rates. This could account for the increase in stress exponent with increasing temperature. Under creep conditions such as these, where grain boundary void formation occurs during second stage creep, Equation 17 would have to be modified by a porosity term which, in addition to being dependent on the distribution of porosity, may also be dependent on total strain.

Note that there are similarities in the creep behavior of UO_2 and ThO_2. These include the nearly linear stress dependence for fine-grained materials and the power law stress dependence for coarse-grained materials, the apparent transition in behavior with increasing stress, and similar activation energies. This similarity is not surprising, since both materials crystallize in the fluorite type structure. It is probable that these two materials would exhibit the same creep behavior at homologous temperatures, other conditions being the same.

Wolfe and Kaufman (Reference 102) made compression creep measurements on ThO_2-10 w/o UO_2 using constant stresses from 1000 to 7500 psi at temperatures from 1700 to 2100°C. The specimens, which were fabricated by cold-pressing and sintering, had an average grain diameter of 30 microns and a density of 97 percent theoretical. Coarser-grained specimens with average grain diameters of 85 and 120 microns were obtained by annealing in helium for four hours at 2200 and 2600°C, respectively. The steady-state creep rates are shown in Figures 27 to 29. The creep characteristics of this material were found to be similar to those of UO_2 and ThO_2. The specimens with 30-micron grains had a linear stress dependence at lower stresses (Figure 27) with a transition to higher stress dependence at higher stresses. Increasing the grain size was found to decrease creep rates in the range of stresses investigated, as shown in Figure 28. Extrapolation to higher stresses would indicate a reversal of the grain size effect, similar to

the behavior of UO_2. The coarse-grained material exhibited power law stress dependence with a stress exponent of about 4 (Figure 29). The temperature dependence of the data for the 120-micron material yielded an activation energy of 120 kcal/mole, and the steady-state creep rates were fit by the expression

$$\dot{\varepsilon}_S = 9.2 \times 10^{-6} \sigma^4 \exp(-120{,}000/RT) \qquad \text{(Eq. 18)}$$

where the strain rate is in hr^{-1} and the stress in psi. No expression was derived for the materials with smaller grains because the data were apparently in the region of transition in primary mode of creep.

It is difficult to determine the effect of UO_2 additions on the creep rates of ThO_2 because of lack of samples for which composition (w/o UO_2) is the only variable and grain size and porosity are constant. However, an estimate of the effect of UO_2 content can be based on the data for coarse-grained ThO_2 and ThO_2-10 w/o UO_2. Since these materials have a stress exponent of 4, their deformation is primarily by dislocation motion. It is believed (Reference 138) that steady-state creep rates for high temperature creep by dislocation motion are proportional to the square of the average grain diameter. It is seen in Figure 30 that the creep data at 1800°C for both the ThO_2 with 220-micron grains and the ThO_2-10 w/o UO_2 with 120-micron grains fall on the same line when the strain rate is divided by the grain diameter squared. This indicates that the difference in creep rates between these two materials is primarily due to grain size effects and that the addition of 10 w/o UO_2 has little effect on creep behavior. This is in agreement with Vickers hardness data at 1800°C which showed only a minor hardness increase with increasing UO_2 content.

2. Hot Pressing

Results of an investigation of the densification of low density nuclear oxides under the influence of an external pressure were reported by Kaufman (Reference 139). Creep rates for the high density material surrounding the as-fabricated pores were calculated on the basis of the MacKenzie-Shuttleworth model of pore closure (Reference 140). Wolfe (Reference 141) assumed that the deformation resulting in pore closure is steady-state creep given by the expression

$$\dot{\varepsilon} = A\sigma^n , \qquad \text{(Eq. 19)}$$

and showed (Reference 141) that the densification rates are related to the creep properties by

$$\frac{dP}{dt} = -\frac{A}{n^n}\left(\frac{3}{2}\right)^{n+1} \frac{P(1-P)}{(1-P\,1/n)^n}\left(g\sigma_a + \frac{2\gamma}{r} - p\right)n \ . \qquad \text{(Eq. 20)}$$

In this equation, P is volume fraction porosity, γ is the surface tension of the pore interface, r is the radius of the pore, p is the gas pressure within the pore, g is a stress correction factor to account for the effect of porosity on stress distribution, and σ_a is the external applied pressure. Assuming negligible effects of surface tension and internal gas, the integrated form of this equation becomes

$$\int_P^{Po} \frac{(1-p^{1/n})n}{P\,(1-p)g^n}\,dP = A\left(\frac{3}{2}\right)^{n+1}\left(\frac{\sigma a}{n}\right)^n t \ . \qquad \text{(Eq. 21)}$$

Low density pellets (80 to 90 percent theoretical density) of various oxides, (UO_2, ThO_2, ThO_2-UO_2, and ZrO_2-UO_2) were pressed uniaxially in a hot pressing apparatus at temperatures from 1600 to 2150°C and pressures of 1000 to 10,000 psi. The densification kinetics were analyzed by means of Equation 19 to determine the creep parameters A and n. General agreement was obtained between the hot-pressing of low density pellets and creep testing of high density pellets. Transitional hot-pressing behavior from a linear to non-linear stress dependence was found to be a function of stress, grain size, composition, and temperature.

3. Effect of Irradiation

Oxide fuel materials can deform plastically during irradiation of operating fuel elements. This is evident from observations of the densification of fabricated porosity under the action of the external loop pressure, the extrusion of fuel through cladding defects, and the healing of cracks as observed in various types of fuel element irradiation tests. In many cases, the in-pile deformation has occurred at relatively low temperatures where thermal creep is negligible. These observations have led to the conclusion that, at high temperatures, such as those at the central regions of fuel elements, the deformation characteristics are thermal while at the cooler regions, less than about 1000°C, there is a fission-induced creep behavior that is dominant (Reference 142).

E. Fracture

1. Crystallography of Fracture

Investigations of the crystallography of fracture in fluorite type compounds have included CaF_2 (Reference 122), BaF_2 (Reference 124), UO_2 (Reference 125), and ThO_2 (Reference 128). It has been found that, depending on loading conditions, fracture can occur on several families of planes. The (111) planes are the most prominent with fracture also occurring on (110) and (100) planes.

2. Fracture Strength

Under certain conditions of loading, particularly with regard to temperature and state of stress, oxide fuel materials will fracture in a brittle manner with little prior plastic deformation. Bend tests of UO_2 (Reference 143) and compression tests on ThO_2 (Reference 129) indicated that brittle fracture occurs for these materials below about 0.5 T_m for the modes of deformation used in the investigations. This result for UO_2 agrees well with the evidence that insufficient slip systems are available below 0.5 T_m for continuous macroscopic plastic flow in polycrystalline samples. Under combined states of stress, on the other hand, these materials can deform plastically prior to deformation at relatively low temperatures. For example, plastic deformation is observed in an indentation hardness test, even at room temperature. In this section, the fracture strengths of oxide fuels under conditions resulting in the brittle type of fracture are discussed.

The fracture strength in the brittle range is sensitive to material and environmental conditions including temperature, state of stress, strain rate, porosity, grain size, specimen dimensions, surface conditions, and atmosphere. It is, therefore, not a simple matter to characterize the strength of a given oxide fuel composition. The greatest advance in relating the strength, or modulus of rupture, of oxide fuels to these various parameters has been in the correlation of strength with grain size and porosity. On the basis of a review of the available data on the effects of these two parameters on strength of brittle, polycrystalline metals and ceramics, Knudsen proposed that these effects could be described by the empirical expression (Reference 144)

$$S = kG^{-a}e^{-bP} \qquad \text{(Eq. 22)}$$

where S is the strength of a specimen (psi), G is the average grain diameter (microns), P is the volume fraction of porosity, and k, a, and b are empirical constants. Knudsen, et al investigated the effects of grain size and porosity on the strength of UO_2 (Reference 145) and ThO_2 (Reference 144) at room temperature and 1000°C. They found a reasonably good correlation of the data with Equation 22, which is believed (Reference 144) to be valid down to porosities of 5 percent and grain sizes of 5 microns. The empirical constants for the various experimental conditions are listed in Table 22.

The results for ThO_2 show that Equation 22 is applicable for different stress systems (both bending and compression tests were included) and for different temperatures. As expected, the empirical constants (k, a, and b) vary with temperature and type of loading. In fact, these empirical parameters will vary with all of the material and environmental factors listed earlier, except G and P, and it is necessary to determine these parameters relative to the particular test conditions. The porosity parameter, b, was found to decrease with sintering temperature for the room temperature bend tests on ThO_2. This variation is apparently related to pore shape and distribution so that the porosity effect is not related to volume fraction porosity alone but varies also with pore morphology. Thus, the empirical constants, particularly b, can depend on fabrication history.

F. Engineering Properties

Results of some pellet performance tests are reviewed in this section. These tests were carried out on samples of thoria pellets representative of the manufactured LWBR core to confirm that the manufactured product met certain minimum requirements of thermochemical and mechanical behavior. The specific "engineering property" tests included: (1) a test to measure resistance to thermal shock, (2) a test to measure dimensional stability, and (3) a test to characterize compression load.

1. Thermal Shock Tests

Fracture occurs in ceramics after a sudden change in temperature. This fracture, known as thermal shock, results from stresses that arise from nonlinear temperature gradients or any restraints to thermal expansion (Reference 146). These stresses are more significant in ceramics than in metals because there is a lack of ductility to relieve the stresses; consequently, cracking and fracture

are more common. In addition when a uniform steady heat flow is disturbed by the presence of internal cracks and crack-like imperfections, whose thermal conductivity differs from that of the ceramic matrix, there is local intensification of the temperature gradient. Associated with this temperature gradient is an increase of thermal stresses which may cause catastrophic spreading of the imperfections. Internal cracks, therefore, aggravate the tendency of ceramics to fracture when thermally shocked.

A constant rate of temperature change can also lead to temperature gradients and thermal stresses. When the sample surface is cooled at a constant rate, a parabolic temperature distribution occurs. The surface temperature is lower than the average temperature, and surface tensile stresses result. The center temperature is higher than the average temperature, and central compressive stresses occur. When the sample is heated, these stresses are reversed. Tensile stresses are thus present during both heating and cooling; since ceramics are much weaker in tension than under compression, failure is considered to occur once the thermal stress concentrations exceed the tensile strength of the ceramic locally. In other words, it is assumed that under the influence of a complex system of stresses imposed on a solid body, its failure would result from overstressing its weakest kind of mechanical strength. In brittle materials, it is the tensile strength.

The thermal stresses causing fracture or cracking depend on the rate of temperature change and on the shape of the ceramic body being shocked. For cylinders, for example, whose length to diameter ratio (L/D) is unity, an average thermal tensile stress can be calculated from the following equation (Reference 146):

$$\sigma_a = \frac{E\alpha}{1-\mu}\frac{K\phi r^2}{d} \qquad \text{(Eq. 23)}$$

where

σ_a = average thermal tensile stress
E = modulus of elasticity
α = thermal expansion coefficient
μ = Poisson's ratio
ϕ = rate of temperature change
d = thermal diffusivity
r = pellet radius
K = constant = 0.105 for cylindrical geometry (L/D = 1).

A more exact method of calculating thermal stresses, based on a determination of the actual temperature distribution across a pellet, yields higher (peak) thermal stress values; these are calculated from the equation

$$\sigma_P = \frac{E\alpha}{1 - \mu} (T_a - T_s) \qquad \text{(Eq. 24)}$$

where $T_a - T_s$ = difference between the pellet average and surface temperatures.

Peak thermal stresses ranging from about 11,000 psi to about 28,000 psi were calculated for various pellet geometries and assumed temperature distributions using the known thermal and mechanical property data for ThO_2. These calculated stresses were found to be of the same magnitude as the only reported (Reference 115) value for the tensile strength of thoria at room temperature, 14,000 psi. Nevertheless, empirical thermal shock tests were designed to characterize pellets having various microstructures. Bettis Laboratory measurements using these gross tests of pellet cracking showed that the manufactured pellets did not fracture under thermal shock conditions that exceeded a 12,000 psi minimum stress limit. In the majority of the tests, the pellet samples were intact after thermal shocks greater than 25,000 psi.

2. Thermal Stability Tests

The purpose of these tests was to establish the limits of dimensional change and density increase associated with post-sintering heat treatments given the as-manufactured high density ThO_2 pellets. Sintered and centerless-ground thoria pellets were dimensionally characterized and then recycled through a repeat sintering in hydrogen at 1750° or 1800°C. Results are summarized in Table 23. As seen from the tabulation, diametral shrinkage ranged from a low of 0.1 mil to a high of 1.3 mills, depending on the pellet size and initial density. Additional densification was as low as 0.05 percent density absolute and as high as 0.89 percent density absolute.

3. Compression Tests

The purpose of the compression test was to characterize the load required to fragment a pellet. Sintered and centerless-ground ThO_2 pellets were end ground to provide flat perpendicular end surfaces. Axial compression tests were performed at room temperature; the loading rate was 0.15 cm/minute. Considerable variation was evident in both the gauge load values corresponding to initial cracking (when it occurred) and complete pellet pulverization. The

gauge load for the latter condition was defined as the crush strength. The point of initial crack formation probably resulted from deviations in flatness and parallelism on the ground surfaces.

Results from numerous measurements are summarized in Table 23. Mean crush strength appears to increase with pellet diameter.

IX. CHEMICAL PROPERTIES

A. Thermal Stability in Air

As was discussed in Section II, thoria is exceedingly stable to high temperatures and is nonreactive to gases up to its melting point. It can, however, adsorb water and CO_2 on exposure to air; this property is discussed in Section X. The ThO_2-UO_2 solid solution, on the other hand, can be oxidized in air to limits which depend on the UO_2 content in the solid solution. These limits were discussed in Section IV.

Furuya (Reference 147) made a thermogravimetric study of the low temperature oxidation behavior of ThO_2-UO_2 powders. Solid solutions of $Th_yU_{1-y}O_2$ were oxidized in air under conditions of linearly increasing temperature from room temperature to 600°C. For UO_2-rich compositions (y = 0 to 0.20), oxidation occurred in two distinct stages, as was the case for UO_2 reported by Aronson, et al, in Reference 148. In the first stage, oxidation proceeded to an O/M ratio of 2.33 with the material remaining cubic in contrast to the tetragonal U_3O_7 formed on oxidation of pure UO_2. The O/M ratios attained after the second stage of oxidation ranged from 2.65 in the case of pure UO_2 to 2.40 for the 20 mole percent ThO_2 solid solution. A mixture of orthorhombic and cubic phases was observed in these oxidized solid solutions.

For the intermediate compositions (y = 0.25 to 0.40) the two oxidation stages merged into essentially one stage; there was an initial plateau at an oxidation level of O/M = 2.32 to 2.34 followed almost immediately by another plateau at an oxidation level equivalent to an O/M of 2.35 to 2.37. And finally for the ThO_2-rich compositions (y = 0.50 to 0.80) there was a single oxidation stage resulting in O/M values that ranged from 2.24 in the case of the 50 mole percent ThO_2 solid solution to 2.10 in the case of the 80 mole percent ThO_2 solid solution.

One kinetic study performed at 250°C (isothermal annealing) in air on $Th_{0.1}U_{0.9}O_2$ showed kinetic behavior very similar to that observed by Aronson, et al (Reference 148) for pure UO_2.

B. Stability in High-Temperature Water

The corrosion behavior of ThO_2 and various ThO_2-UO_2 compositions up to 50 weight percent UO_2 was studied in high temperature (360°C), alkaline (pH 10) flowing water, both degassed and oxygenated (5 and 100 ppm) as part of a study of the behavior in such media of various oxide nuclear fuels including UO_2 (Reference 17). The results of the exposure tests confirmed earlier work (Reference 11) in showing that sintered compacts of UO_2 are extremely resistant to corrosive or erosive attack in high temperature water in the absence of oxygen but corrode rapidly in the flowing, oxygenated high pH water system. The ThO_2 samples displayed good corrosion resistance even in oxygenated high temperature water; this result is not surprising since thorium forms no higher oxide than ThO_2. In the case of the ThO_2-UO_2 solid oxides, no corrosion attack was noted for any of the oxide compositions in either the nonoxygenated water or in the water containing 5 ppm O_2.

Exposure of ThO_2-UO_2 of two compositions (ThO_2-20 w/o UO_2 and ThO_2-50 w/o UO_2) to water oxygenated to 100 ± 10 ppm, the highest level tested, showed high weight gains. However, all the specimens retained their mechanical integrity throughout the test period of 140 days, forming a surface oxidized phase. This oxidized phase was found, by x-ray diffraction analysis, to be cubic, probably of the M_4O_9 type. This result suggests than an M_4O_9-type of single phase region exists in the low temperature ternary phase diagram for ThO_2-UO_2-O_2, a result consonant with the air oxidation studies of similar compositions discussed above.

C. Compatability Behavior

A tabulation of miscellaneous chemical interactions of thoria with liquid and solid metals has been made by Peterson and Curtis (Reference 1) and is not repeated here. In addition to these tabulated data, Grossman and Kaznoff (Reference 149) reported that thoria did not react with cesium vapor after a 300 hour test at 4 torr at temperatures up to 1600°C. It has also been reported (Reference 150) that thoria shows essentially no corrosion with liquid sodium containing 10 ppm oxygen at temperatures of 800 to 1500°C. Comparable data for ThO_2-UO_2 do not exist.

X. SURFACE PROPERTIES

A. Surface Energy

Estimates of the surface energies for ThO_2 and UO_2 made from experimental measurements or from theoretical considerations show considerable variation. Kolar (Reference 151) measured the rise in temperature on wetting a fine UO_2 powder of measured surface area and arrived at a figure of 490 ergs/cm^2 for the heat of immersion in water of UO_2. This quantity represented the difference in energy between a UO_2-air interface and a UO_2-water interface. Similarly, heats of immersion in water of ThO_2 were measured by Holmes and co-workers (References 152 to 154) but, as is discussed in Section B below, the data revealed complex behavior suggesting that surface energies estimated from such measurements may be in gross error.

Livey and Murray (Reference 155) reported a value of 642 ergs/cm^2 for UO_2 from measurements of contact angles of wetting of liquid metals. They also estimated a value of 530 ergs/cm^2 for ThO_2 from an assumed straight line relationship between surface energy and the reciprocal of molar volume for "similar compounds", e.g., alkali halides.

Benson, et al, (Reference 6) estimated the surface energies of both thorium dioxide and uranium dioxide theoretically by applying the Born-Haber cycle to these oxides. Implicit in these calculations is the assumption of negligible convalency in the bonding of UO_2 and ThO_2, the same assumption made in the calculation of cohesive energies, as was discussed in Section II.E. Benson, et al calculated values of 1150 ergs/cm^2 for ThO_2 and 1030 ergs/cm^2 for UO_2. They also estimated values of 810 and 150 ergs/cm^2 for ThO_2 and UO_2, respectively, from compressibility data, but concluded that this set of values was too low. Benson, et al also questioned the suitability of the Livey and Murray approximation and recommended the values calculated from the Born-Haber cycle method. It appears that surface energy values near 1000 ergs/cm^2 for these oxides are not unreasonable.

B. Gas Adsorption

1. Water Vapor Adsorption on ThO_2

The nature of the surface adsorption of liquid water and of water vapor by thoria has been studied extensively by Holmes, et al (References 156 and

157) and by Gammage, et al (References 158 and 159). A variety of techniques, including calorimetric, gravimetric, and infrared adsorption measurements, have been used. Results of these experimental observations have shown that adsorption of water vapor on thoria is tenacious and the binding of water to the oxide surface is complex.

In the first paper in the series of reports (References 152 to 154), Holmes and Secoy (Reference 152) measured the heats of immersion in water at 25.0°C of a series of ThO_2 powders whose specific surface areas varied considerably. This variation in surface area was accomplished by calcining at different temperatures the same lot of thorium oxalate powder prepared by precipitation from a nitrate solution with oxalic acid. All calcined powders were pretreated before the calorimetric measurements by vacuum outgassing for 24 hours at temperatures ranging from 100 to 500°C.

Two important observations were made from data on heat of immersion in water of the powders as a function of outgassing temperature. First, there was a general increase in the heat of immersion with increase of the outgassing temperature given the powders; values ranged from about 450 to 575 ergs/cm^2 for a degassing temperature of 100°C to values of 550 to 1100 ergs/cm^2 for a degassing temperature of 500°C. Second, the various powder samples had remarkably different energetics with respect to the solid-water interface. One powder, for example, showed not only a low heat of immersion but one that was less dependent on the outgassing temperature. Holmes and Secoy explained the variation in the measured heats of immersion as a result of the progressive removal of strongly bound chemisorbed water vapor from the powder as the outgassing temperature was increased; on subsequent exposure of the powder to liquid water during the immersion process this chemisorbed water is replaced, accompanied by a large net heat of adsorption as large as 22 kcal/mole.

The complexity of the water vapor adsorption process on thoria was clarified in a number of subsequent papers. A "bare" thoria powder surface adsorbs water in an amount equivalent to three chemisorbed layers. The first water layer is "dissociatively" chemisorbed to form two surface hydroxyl groups per surface thorium ion. Subsequent adsorption is controlled by the slow hydration of each of these surface hydroxyl groups to form the second and third layers. Thus, the total quantity of water involved is the weight equivalent of three chemisorbed monolayers.

It was also shown that in vacuum a temperature as high as 1000°C was required to obtain a "dry" weight of thoria; heating in vacuum to 500°C left the oxide surface in a partially hydrated state. Presumably, various degrees of partial hydration are possible depending on the degassing temperature to which the powder is subjected.

An infrared spectroscopic analytical technique was used by Fuller, et al (Reference 159) to elucidate the structure of the adsorbed water layer on thoria surfaces. The results were found to be in accord with the structures proposed on the basis of gravimetric and calorimetric data, namely that there is considerable hydrogen bonding with one water molecule strongly associated with each of two surface hydroxyl groups in the adsorbed layer.

Some results obtained at Bettis Atomic Power Laboratory are in qualitative agreement with the extent of water adsorption by ThO_2 powder discussed above. The moisture content and the gas adsorption (BET) surface areas of six lots of LWBR production ThO_2 powder were measured and compared. The ThO_2 powders were prepared at National Lead of Ohio (NLO) by air calcination of the thorium oxalate precipitate (Reference 160). Initial analyses for both water moisture content and surface area were performed at NLO some time after the powders were prepared at that location. Measurements tabulated in Table 24 show that the water contents of the "as-fabricated" powders were equivalent to about 0.5 to 1.3 monomolecular layers of adsorption. Subsequent analyses of the powders made at the Bettis Atomic Power Laboratory after the powders were exposed to the ambient air for about one month showed water adsorption equivalent to 1.4 to 2.3 monolayers.

In a similar manner, measurements were made of the amount of moisture pickup by degassed, high density ThO_2 pellets as a function of relative humidity and exposure time. The data showed that the moisture adsorbed by the pellets increased with increasing humidity and increasing time of exposure to a level approximately equivalent to 1 to 3 monolayers; the uncertainty arises from the uncertainty in the specific surface area of the pellet.

Thorium dioxide is apparently not unique in its interaction with adsorbed water. The work of Anderson, et al (References 161 and 162) showed that a clean surface of magnesium oxide is first covered by a layer of hydroxyl ions. Water is then physically adsorbed onto the hydroxylated surface and slowly converts to a more strongly bound species in an amount corresponding to about a monolayer.

2. Adsorption of CO_2 Gas on ThO_2 Powders

Adsorbed CO_2 gas can influence the adsorptive characteristics of the thoria surface. For example, for some thoria powders that apparently adsorbed less water vapor, it was found that these powders evolved CO_2 when heated above 600°C. It was thought at first that the surface CO_2 originated from residual carbon from the original oxalate decomposition. It was subsequently reported (Reference 163) from infrared analysis that thorium dioxide rapidly chemisorbs CO_2 from the atmosphere at room temperature and that this CO_2 can be removed by evacuation only if the temperature is raised to 900°C. However, Clayton (Reference 160) found that adsorbed CO_2 equivalent to about 0.5 of a monolayer is essentially released at 500°C.

C. Gas Release from Pellets

Measurements of the gas released from unirradiated thoria-base oxide fuel pellets were reported by Smid (Reference 36). Mass spectrographic techniques were used to identify the gaseous species evolved after heating at various temperatures up to 2000°C. The major gases released were CO and H_2 in approximate ratio of 4 to 1. There was also evidence of much smaller amounts of CO_2 released. Of the quantity of hydrogen gas presumably present in sintered pellets of ThO_2 and ThO_2-UO_2 (as measured by extraction at 2000°C) approximately 75 percent and 90 percent, respectively, were released by vacuum extraction at 1000°C. A degassing temperature of 1200°C was required to effect complete release of the contained gas (H_2 and CO_2).

ACKNOWLEDGMENTS

This work was performed under Contract EY-76-C-11-0014 of the U. S. Department of Energy in support of the LWBR development program. The authors are grateful to the U. S. Department of Energy and the Westinghouse Electric Corporation for permission to publish this work.

REFERENCES

1. S. Peterson and C. E. Curtis, "Thorium Ceramics Data Manual, Vol. I - Oxides," ORNL-4503, Volume I, September 1970.
2. J. H. Kittel, et al, "Properties of Fuels For Alternate Breeder Fuel Cycles," ANL-AFP-38, September 1977.
3. R. Benz, "Thorium-Thorium Dioxide Phase Equilibria," J. Nucl. Mat. 29, 43-49 (1969).

4. R. W. G. Wyckoff, Crystal Structures, 2nd edition, Vol. I, p. 241, Interscience Publishers (Wiley), New York 1963.
5. B. G. Childs, "The Cohesive Energy of Uranium and Thorium Dioxides," CRMET 788 (1958).
6. G. G. Benson, P. I. Freeman, and E. Dempsey, "Calculation of Cohesive and Surface Energies of Thorium and Uranium Dioxides," J. Am. Ceram. Soc. 46, 43-47 (1963).
7. R. C. Weast, ed. Handbook of Chemistry and Physics, 57th edition, 1976-1977, pp. F-213 and F-214.
8. R. D. Baybarz and R. G. Haire, "Investigation of the Transplutonium Oxides by X-Ray and Electron Diffraction," Conf. 720931-4 (1972).
9. E. W. I. Roeder and H. S. C. Wilson, "The System CaO-ThO_2-ZrO_2," J. Am. Ceram. Soc. 58, 161-163 (1975).
10. C. Keller, U. Berndt, H. Enserer, and L. Leitner, "Phasensleuchsewichte in den Systemen Thoriumoxid-Lanthanoxid," J. Solid State Chem. 4, 453-465 (1972).
11. J. Belle, ed. Uranium Dioxide: Properties and Nuclear Applications, U. S. Government Printing Office, 1961.
12. W. A. Lambertson, M. H. Mueller, and F. H. Gunzel, Jr., "Uranium Oxide Phase Equilibrium Systems: IV, UO_2-ThO_2," J. Am. Ceram. Soc. 36, 397-399 (1953).
13. J. A. Christensen, "UO_2-ThO_2 Phase Studies," HW-76559, January 1963, pp. 11.5-11.6.
14. I. Cohen and R. M. Berman, "A Metallographic and X-Ray Study of the Limits of Oxygen Solubility in the UO_2-ThO_2 System," J. Nucl. Mat. 18 (2) 77-107 (1966).
15. J. S. Anderson, D. N. Edgington, L. E. J. Roberts, and E. Wait, "The Oxides of Uranium Part IV, The System UO_2-ThO_2-O," J. Chem. Soc. (London) 3, 3324-3331 (1954).
16. L. O. Gilpatrick, H. H. Stone, and C. H. Secoy, "Equilibrium Studies in the System ThO_2-UO_2-UO_3," ORNL-3591, January 1964.
17. J. M. Markowitz and J. C. Clayton, "Corrosion of Oxide Nuclear Fuels in High Temperature Water (LWBR Development Program)," WAPD-TM-909, February 1970.
18. R. M. Berman, "The Homogenization of ThO_2-UO_2 (LWBR Development Program)," WAPD-TM-1051, December 1972.

19. L. Darken, "Diffusion, Mobility and Their Interrelation Through Free Energy in Binary Metallic Systems," Trans AIME 175, 184-190 (1948).
20. R. M. Berman, "Methods For Assessing Homogeneity in ThO_2-UO_2 Fuels (LWBR Development Program)," WAPD-TM-1377, June 1978.
21. R. E. Latta, E. C. Duderstadt, and R. E. Fryxell, "Solidus and Liquidus Temperatures in the UO_2-ThO_2 System," J. Nucl. Mat. 35, 347-349 (1970).
22. J. A. Christensen, R. J. Allio, and A. Biancheria, "Melting Point of Irradiated Uranium Dioxide," WCAP-6065, February 1965.
23. W. R. Mott, "Relative Volatilaties of Refractory Materials," Trans. Am. Electrochem. Soc. 34, 255-295 (1916).
24. B. Ohnysty and F. K. Rose, "Thermal Expansion Measurements on Thoria and Hafnia to 4500°F," J. Am. Ceram. Soc. 47, 398-400 (1964).
25. C. P. Kempter and R. O. Elliott, "Thermal Expansion of UN, UO_2, and UO_2-ThO_2," J. Chem. Phys. 30, 1524-1526 (1959).
26. A. Brown and A. Chitty, "Thoria as a Fertile Component for a Liquid Metal Breeder Blanket," J. Nucl. Energy Pt. B1., 145-152 (1960).
27. F. A. Mauer and L. H. Bolz, Measurement of Thermal Expansion of Cermet Components by High Temperature X-Ray Diffraction, WADC-TR-55473 (December 1955).
28. B. J. Skinner, "Thermal Expansions of Thoria, Periclase and Diamond," Am. Mineralogist 42, 39-55 (1957).
29. J. R. Springer, E. A. Eldridge, M. U. Goodyear, T. R. Wright, and J. F. Lagedrost, "Fabrication, Characterization, and Thermal Property Measurements of ThO_2-UO_2 Fuel Materials," BMI-X-10210, October 1, 1967.
30. M. Hoch and A. C. Momin, "High Temperature Thermal Expansion of UO_2 and ThO_2," High Temperature - High Pressures, 1, 410-417 (1969).
31. K. Hirata, K. Moriya, and Y. Waseda, "High Temperature Thermal Expansion of ThO_2, MgO and Y_2O_3 by X-Ray Diffraction," J. Materials Science 12, 839-839, 1977 - Letters.
32. R. M. Berman, T. S. Tully, J. Belle, and I. Goldberg, "The Thermal Conductivity of Polycrystalline Thoria and Thoria-Urania Solid Solutions (LWBR Development Program)," WAPD-TM-908, December 1972.
33. J. R. Springer and J. F. Lagedrost, "Thermal Properties of Bettis-Fabricated ThO_2-UO_2 Fuel Materials (LWBR Development Program)," BMI-X-10231, March 1, 1968.

34. J. Belle, R. M. Berman, W. F. Bourgeois, I. Cohen, and R. C. Daniel, "Thermal Conductivity of Bulk Oxide Fuels," WAPD-TM-586 (Rev.), April 1967.

35. G. P. Marino, "The Porosity Correction Factor for the Thermal Conductivity of Porous Materials (LWBR Development Program)," WAPD-TM-807, February 1970; see also J. Nucl. Mat. 38, 178-190 (1971). (The published version in J. Nucl. Mat., however, has significant misprints in its Equations 8 and 9).

36. R. J. Smid, "Gas Release From Thoria-Base Oxide Fuel Pellets (LWBR Development Program)," WAPD-TM-850, April 1971.

37. D. W. Osborne and E. F. Westrum, Jr., "The Heat Capacity of Thorium Dioxide from 10 to 305°K. The Heat Capacity Anomalies in Uranium Dioxide and Neptunium Dioxide," J. Chem. Phys. 21, 1884-1887 (1953).

38. T. G. Godfrey, J. A. Wooley, and J. M. Leitnaker, "Thermodynamic Functions of Nuclear Materials: UC, UC_2, UO_2, ThO_2 and UN," ORNL-TM-1596 (Rev.), December 1966.

39. A. C. Victor and T. B. Douglas, "Thermodynamic Properties of Thorium Dioxide from 298 to 1200°K," J. Res. Natl. Bur. Std. A 65, 105-111 (1961).

40. J. C. Southard, "A Modified Calorimeter for High Temperatures. The Heat Content of Silicon, Wollastonite and ThO_2 Above 25°," J. Am. Chem. Soc. 63, 3142-3146 (1941).

41. M Hoch and H. L. Johnston, "The Heat Capacity of Aluminum Oxide from 1000 to 2000° and Thorium Dioxide from 1000 to 2500°," J. Phys. Chem. 65, 1184-1185 (1961).

42. E. J. Huber, C. E. Holley, Jr., and E. H. Meierkord, "The Heats of Combustion of Thorium and Uranium," J. Am. Chem. Soc. 74, 3406-3408 (1952).

43. R. Hultgren, et al, Selected Values of Thermodynamic Properties of Metals and Alloys, p. 281 John Wiley & Sons, Inc. New York, 1963.

44. D. R. Stull and G. C. Sinke, Thermodynamic Properties of the Elements, p. 143 American Chemical Society, Washington, D.C., 1956.

45. M. H. Rand, "Part I. Thermochemical Properties" in Thorium: Physico-Chemical Properties of Its Compounds and Alloys, ed. by O. Kubaschewski, Atomic Energy Review, Special Issue No. 5, IAEA (1975).

46. E. Shapiro, "Vapor Pressure of Thorium Oxide from 2050 to 2225°K," J. Am. Chem. Soc. 74, 5233-5235 (1952).

47. M. Hoch and J. L. Johnston, "The Reaction Occurring on Thoriated Cathodes," J. Am. Chem. Soc. 76, 4833-4835 (1954).

48. A. J. Darnell and W. A. McCollum, High Temperature Reactions of Thorium and Thoria and the Vapor Pressure of Thoria, NAA-SR-6498 (September 15, 1961).

49. E. G. Wolff and C. B. Alcock, "The Volatilization of High-Temperature Materials in Vacuo," Trans. Brit. Ceram. Soc. 61, 667-687 (1962).

50. R. J. Ackermann, E. G. Rauh, R. J. Thorn, and M. C. Cannon, "A Thermodynamic Study of the Thorium-Oxygen System at High Temperatures," J. Phys. Chem. 67, 762-769 (1963).

51. C. A. Alexander, J. S. Ogden, and G. W. Cumminghan, Thermal Stability of Zirconia- and Thoria-Base Fuels, BMI-1789 (January 6, 1967).

52. R. J. Ackermann, E. G. Rauh, "High Temperature Properties of the Thorium-Oxygen System: A Revision of the Thermodynamic Properties of ThO(g) and ThO_2(g)," High Temperature Science 5, 463-473 (1973).

53. S. Aronson and J. C. Clayton, "Thermodynamic Properties of Non-stiochiometric Urania - Thoria Solid Solution," J. Chem. Phys. 32, 749-752 (1960).

54. L. E. Roberts, et al, "The Actinide Oxides," Proc. Intern. Conf. Peaceful Uses Atomic Energy, 2nd, Geneva, 1958, 28, 215-222.

55. E. A. Aitken, J. A. Edwards, and R. A. Joseph, "Thermodynamic Study of Solid Solutions of Uranium Oxide. I. Uranium Oxide-Thorium Oxide," J. Phys. Chem. 70, 1084-1090 (1966).

56. A. L. Dragoo, IV Diffusion in Thorium: Physico-Chemical Properties of its Compounds and Alloys in Atomic Energy Review Special Issue No. 5, ed. O. Kubaschewski, IAEA, Vienna, 1975.

57. C. S. Morgan and C. S. Yust, Metals and Ceramics Div. Ann. Prog. Report May 31, 1961, ORNL 3160, pp. 41-42.

58. H. S. Edwards, A. I. Rosenberg, and J. T. Bittel, "Thorium Oxide - Diffusion of Oxygen, Compatability with Borides, and Feasibility of Coating Borides by Pyrohydrolysis of Metal Halides," Tech. Doc. Rep. ASD-TDR-63-635, July 1963.

59. K. Ando, Y. Oishi, and Y. Hidaka, "Self-Diffusion of Oxygen in Single Crystal Thorium Oxide," J. Chem. Phy. 65, 2751-2755 (1976).

60. A. B. Auskern and J. Belle, "Oxygen Ion Self-Diffusion in Uranium Dioxide," J. Nucl. Mat. 3, 267-276 (1961).

61. J. Belle, A. B. Auskern, W. A. Bostrom, and F. S. Susko, "Diffusion Kinetics in Uranium Dioxide" in Reactivity of Solids, ed. J. H. DeBoer Elsevier Publishing Company, 1961, pp. 452-465.

62. J. Belle, "Oxygen and Uranium Diffusion in Uranium Dioxide (A review)," J. Nucl. Mat. 30, 3-15 (1969).

63. J. F. Marin and P. Contamin, "Uranium and Oxygen Self-Diffusion in UO_2," J. Nucl. Mat. 30, 16-25 (1969).

64. R. L. Deaton and C. J. Wiedenheft, "Self-diffusion of Oxygen in $^{238}PuO_2$," J. Inorg. Nucl. Chem. 35, 649-650 (1973).

65. L. E. Poteat and C. S. Morgan, Metals and Ceramics Div. Ann. Prog. Rept. June 30, 1968, ORNL-4370, pp. 31-33.

66. R. J. Hawkins and C. M. Alcock, "A Study of Cation Diffusion in UO_{2+x} and ThO_2 Using α-Ray Spectrometry," J. Nucl. Mat. 26, 112-122 (1968).

67. A. D. King, "Thorium Diffusion in Single Crystal ThO_2," J. Nucl. Mat. 38, 347-349 (1971).

68. A. D. King, "Thorium Diffusion in Thoria and Urania," Chalk River (Canada), Report AECL-3655 (1970).

69. D. K. Riemann and T. S. Lundy, "Diffusion of ^{233}U in UO_2," J. Am. Ceram. Soc. 52, 511-512 (1969).

70. R. W. Ure, Jr., "Ionic Conductivity of Calcium Fluoride Crystals," J. Chem. Phys. 26, 1363-1373 (1957).

71. W. H. Rhodes and R. E. Carter, "Cationic Self-Diffusion in Calcia Stabilized Zirconia," J. Am. Ceram. Soc. 49, 244-249 (1966).

72. H. Furuya, "Lattice and Grain Boundary Diffusion or Uranium in ThO_2 and ThO_2-UO_2 Solid Solution," J. Nucl. Mat. 26, 123-128 (1968).

73. H. Matzke, "Xenon Migration and Trapping in Doped ThO_2," J. Nucl. Mat. 21, 190-198 (1967).

74. H. Furuya and S. Yajima, "Lattice and Grain Boundary Diffusions of Protactinium in ThO_2 and in a ThO_2-UO_2 Solid Solution," J. Nucl. Mat. 25, 38-44 (1968).

75. F. A. Nichols, "Measurement of Surface Diffusion Coefficients by Coalescence of Inert Gas Bubbles," Acta Met. 15, 365-367 (1967).

76. F. A. Nichols, "Coalescence of Two Spheres by Surface Diffusion," J. Appl. Phys. 37, 2805-2808 (1966).

77. R. M. Berman, "Surface Diffusion Measurements in ThO_2, UO_2, and ThO_2-UO_2 (LWBR Development Program)," WAPD-TM-843, July 1969.

78. W. W. Mullins, "Theory of Thermal Grooving," J. App. Phys. 28, 333-339 (1957).

79. E. A. Aitken, "Thermal Diffusion in Closed Oxide Fuel Systems," J. Nucl. Mat. 30, 62-73 (1969).

80. M. G. Adamson and R. F. A. Carney, "Mechanistic Study of Oxygen Thermal Diffusion in Hyperstichiometric Urania and Urania-Plutonia Solid Solutions," J. Nucl. Mat. 54, 121-137 (1974).

81. F. Felix, T. Lagerwall, P. Schmeling, and K. E. Zimen, "Rare Gas Release From Solids with Special Attention of Nuclear Fuel Materials," Proc. 3rd Int. Conf. Peaceful Uses Atomic Energy (Proc. Conf. Geneva 1964) 11, UN, NY, pp 363-367 (1965).

82. R. Kelly and H. Matzke, "A Study of Inert Gas Diffusion in Ionic Crystals and Sinters with Emphasis on the Ion-Bombardment Technique," J. Nucl. Mat. 17, 179-191 (1965).

83. R. Thomas and L. Lindner, "Diffusion of Non-Volatile Fission Products in UO_2 and ThO_2, as Determined by Leaching into Molten Salts," Radiochemica Acta 4, 170-171 (1965).

84. J. L. Bates, "Fission Product Distribution in Irradiated UO_2," BNWL058 (1965).

85. B. T. Bradbury, J. T. Demant, P. M. Martin, and D. M. Poole, "Electron Probe Microanalysis of Irradiated UO_2," J. Nucl. Mat. 17, 227-236 (1965).

86. H. Kamogawa, H. Tomishima, H. Nagami, K. Ogawa, N. Io, N. Wakabayashi, T. Ohno, and K. Naito, "Irradiation Tests of UO_2 Fuel," A/Conf. 28/P 430 (1964).

87. N. Oi and J. Takagi, "Diffusion of Non-gaseous Fission Products in UO_2 Single Crystals," Z. Naturforsch 19A, 1331-1332 (November 1974).

88. N. Oi and J. Takagi, "Distribution of Fission Products in Irradiated UO_2," J. Nucl. Sci. and Technol. (Japan) 2, 127-131 (1965).

89. N. Oi and I. Tanabe, "Fission Product Segregation at the Surface of Irradiated UO_2 Particles," J. Nucl. Mat. 25, 288-295 (1968).

90. F. Anselin, "The Role of Fission Products in the Swelling of Irradiated UO_2 and $(U, Pu)O_2$ Fuel," GEAP-5583 (1969).

91. J. K. Bahl and M. D. Freshley, "Plutonium and Fission Product Redistribution in Mixed-Oxide Fuels During Irradiation," Nucl. Technol. 15, 114-124 (1972).

92. J. H. Davies and F. T. Ewart, "Electron Microprobe Analysis of Metallic Inclusions Formed in Irradiated $PuO_{2.0}$ and $Pu_{1.7}$ at High Burnups," AERE-R6310 (1970).

93. C. E. Johnson, D. V. Steidl, and C. E. Crouthamel, "Distribution of Gaseous Fission Products in Irradiated Mixed-Oxide Fuels," in "Fast Reactor Fuel Element Technology," R. Farmakes, ed., pp. 603-613, ANS, 1971.

94. R. O. Meyer, E. M. Butler, and D. R. O'Boyle, "Actinide Redistribution in Mixed-Oxide Fuels Irradiated in a Fast Flux," ANL-7929 (1972).

95. D. R. O'Boyle, F. L. Brown, and J. E. Sanecki, "Solid Fission Product Behavior in Uranium-Plutonium Oxide Fuel Irradiated in a Fast Neutron Flux," J. Nucl. Mat. 29, 27-42 (1969).

96. G. Camozzo, "Physico-Chemical State of Fission Products in Irradiated Oxide $(U, Pu)O_2$ Fuels," EUR-4613 (1971).

97. J. T. Bramman, R. M. Sharpe, and G. Yates, "Metallic Fission-Product Inclusions in Irradiated Oxide Fuels," J. Nucl. Mat. 25, 201-215 (1968).

98. C. E. Johnson and C. E. Crouthamel, "Cladding Interactions in Mixed-Oxide Irradiated Fuels," J. Nucl. Mat. 34, 101-104 (1970).

99. D. R. O'Boyle and R. O. Meyer, "Redistribution of Uranium and Plutonium in Mixed-Oxide Fuels during Irradiation," in "Behavior and Chemical State of Irradiated Ceramic Fuels," pp. 41-66, IAEA, Vienna, 1974.

100. M. G. Adamson and E. A. Aitken, "Pu, U Redistribution in $(U, Pu)O_2$ Fuels by Temperature Gradients," in "Behavior and Chemical State of Irradiated Ceramic Fuels," pp. 225-235, IAEA, Vienna, 1974.

101. R. M. Berman, "Fission Product Distribution in Oxide Fuels (LWBR Development Program)," WAPD-TM-1236, December 1976.

102. R. A. Wolfe and S. F. Kaufman, "Mechanical Properties of Oxide Fuels," WAPD-TM-587, October 1967.

103. P. M. Macedo, W. Capps, and J. B. Wachtman, Jr., "Elastic Constants of Single Crystal ThO_2 at 25°C," J. Am. Ceram. Soc. 47, 651-655 (1964).

104. J. B. Wachtman, Jr., M. L. Wheat, H. J. Anderson, and J. L. Bates, "Elastic Constants of Single Crystal UO_2 at 25°C," J. Nucl. Mat. 16, 39-41 (1965).

105. H. B. Huntington, "The Elastic Constants of Crystals" in "Solid State Physics," F. Seitz and D. Turnbull, Eds., Vol. 7, pp. 213-351, Academic Press, New York, 1958.

106. W. Voigt, "Lehrbuch der Krystallphysik (Mit Ausschluss der Krystalloptik)," Teubner, Leipzig, 1910.

107. A. Reuss, "Calculation of Flow Limits of Mixed Crystals on the Basis of Plasticity of Single Crystals," Z. Angew. Math. Mech. 9, 49-58 (1929).

108. R. Hill, "The Elastic Behavior of a Crystalline Aggregate," Proc. Phys. Soc. (London) 65A, 349-354 (1952).

109. S. Spinner, F. P. Knudsen, and L. Stone, "Elastic Constant - Porosity Relations for Polycrystalline Thoria," J. Res. Natl. Bur. Std. 67C, 39-46 (1963).

110. O. L. Anderson and J. E. Nafe, "The Bulk Modulus-Volume Relationship for Oxide Compounds and Related Geophysical Problems," J. Geophysical Res. 70, 3951-3960 (1965).

111. J. B. Wachtman, Jr., W. E. Tefft, D. G. Lam, Jr., and C. S. Astein, "Exponential Temperature Dependence of Young's Modulus for Several Oxides," Phys. Rev. 122, 1754-1759 (1961).

112. O. J. Whittemore, personal communication referenced as 103 in R. J. Runck, "Oxides," in "High-Temperature Technology," I. E. Campbell, Ed., p. 48, John Wiley and Sons, Inc., New York, 1956.

113. O. L. Anderson, "Derivation of Wachtman's Equation for the Temperature Dependence of Elastic Moduli of Oxide Compounds," Phys. Rev. 144, 553-557 (1966).

114. S. Spinner, L. Stone, and F. P. Knudsen, "Temperature Dependence of the Elastic Constants of Thoria Specimens of Varying Porosity," J. Res. Natl. Bur. Std. 67C, 93-100 (1963).

115. E. Ryshkewitch, Oxide Ceramics: Physical Chemistry and Technology, Academic Press, New York, 1960.

116. J. B. Wachtman, Jr., and D. G. Lam, Jr., "Young's Modulus of Various Refractory Materials as a Function of Temperature," J. Am. Ceram. Soc. 42, 254-260 (1959).

117. J. F. Wygant, "Elastic and Flow Properties of Dense, Pure Oxide Refractories," J. Am. Ceram. Soc. 34, 374-380 (1951).

118. S. M. Lang and F. P. Knudsen, "Some Physical Properties of High Density Thorium Dioxide," J. Am. Ceram. Soc. 39, 415-424 (1956).

119. C. E. Curtis and J. R. Johnson, "Properties of Thorium Oxide Ceramics," J. Am. Ceram. Soc. 40, 63-68 (1957).

120. R. J. Stokes, "Correlation of Mechanical Properties with Microstructure," in Microstructure of Ceramic Materials, U. S. National Bureau of Standards Miscellaneous Publication 257, pp. 41-72, U. S. Government Printing Office, Washington, D. C., 1964.

121. A. G. Evans, C. Roy, and P. L. Pratt, "The Role of Grain Boundaries in the Plastic Deformation of Calcium Fluoride," Proc. Brit. Ceram. Soc. 6, 173-189 (1966).

122. W. L. Phillips, Jr., "Deformation and Fracture Processes in Calcium Fluoride Single Crystal," J. Am. Ceram. Soc. 44, 499-506 (1961).

123. R. Burn and G. T. Murray, "Plasticity and Dislocation Etch Pits in CaF_2," J. Am. Ceram. Soc. 45, 251-252 (1962).

124. T. S. Liu and C. H. Li, "Plasticity of Barium Fluoride Single Crystals," J. Appl. Phys. 35, 3325-3330 (1964).

125. E. J. Rapperport and A. M. Huntress, "Deformation Modes of Single Crystal Uranium Dioxide from 700°C to 1900°C," NMI-1242, August 24, 1960.

126. K. H. G. Ashbee, reported in "Conference on Inorganic and Intermetallic Crystals, Birmingham, April 1963," by B. Beagley and J. W. Edington, Brit. J. Appl. Phys. 14, 609-613 (1963).

127. J. W. Edington and M. J. Klein, "Slip and Fracture in Single Crystals of Thoria," J. Appl. Phys. 37, 3906-3908 (1966).

128. A. Gilbert, "Deformation and Fracture of Thoria," Phil. Mag. 12, 139-144 (1965).

129. C. S. Yust and L. E. Potcat, "Compressive Strength of Thoria" in "Metals and Ceramic Division Annual Progress Report for Period Ending June 30, 1965," S. Peterson, Ed., ORNL-3870, November 1965, pp. 41-42.

130. J. L. Bates, "Microhardness of Uranium Dioxide," HW-SA-3014, 1962.

131. R. J. Smid, "Grain Growth in Thoria and Thoria-Base Fuel Pellets," WAPD-TM-1311, January 1976.

132. T. R. Wright, D. E. Kizer, and D. L. Keller, "Studies in the UO_2-ZrO_2 System," BMI-1689, August 27, 1964.

133. R. D. Koester, D. E. Price, and D. P. Moak, "Hot-Hardness Measurements of ThO_2 + UO_2 Fuel Pellets," BMI-X-447, August 1967.

134. D. Tabor, "The Hardness of Metals," Clarendon Press, Oxford, 1951; G. Atkins and D. Tabor, "The Plastic Deformation of Crossed Cylinders and Wedges," J. Inst. Metals 94, 107-115 (1966).

135. J. H. Westbrook, "Flow in Rock Salt Structures," WADC-TR-304, August 1958. Also available as AD-155651.

136. A. G. Atkins, A. Silverio, and D. Tabor, "Indentation Hardness and the Creep of Solids," J. Inst. of Metals 94, 369-378 (1966).

137. L. E. Poteat and C. S. Yust, "Creep of Polycrystalline Thorium Dioxide," J. Am. Ceram. Soc. 49, 410-414 (1966).

138. O. D. Sherby, "Factors Affecting the High Temperature Strength of Polycrystalline Solids," Acta Met. 10, 135-147 (1962).

139. S. F. Kaufman, "The Hot Pressing Behavior of Sintered Low Density Pellets of UO_2, ZrO_2 + UO_2, ThO_2, and ThO_2 + UO_2," WAPD-TM-751, 1969.

140. J. K. MacKenzie and R. Shuttleworth, "A Phenomenological Theory of Sintering," Proc. Phys. Soc. (London) 62B, 833-852 (1949).

141. R. A. Wolfe, "The Theory of Hot Pressing for a Solid with Nonlinear Viscosity," WAPD-T-2021, June 1967.

142. E. Duncombe, "Comparisons with Experiment of Calculated Dimensional Changes and Failure Analysis of Irradiated Bulk Oxide Fuel Test Rods Using the CYGRO-1 Computer Program," WAPD-TM-583, September 1966.

143. C. R. Tottle, "Mechanical Properties of Uranium Compounds," ANL-7070, November 1965.

144. F. P. Knudsen, "Dependence of Mechanical Strength of Brittle Polycrystalline Specimens on Porosity and Grain Size," J. Am. Ceram. Soc. 42, 376-387 (1959).

145. F. P. Knudsen, H. S. Parker, and M. D. Burdick, "Flexural Strength of Specimens Prepared from Several Uranium Dioxide Powders; Its Dependence on Porosity and Grain Size and the Influence of Additions of Titania," J. Am. Ceram. Soc. 43, 641-647 (1960).

146. W. D. Kingery, H. K. Bowen, and D. R. Uhlmann, Introduction to Ceramics, 2nd edition John Wiley & Sons, New York, 1976.

147. H. Furuya, "Oxidation Behavior of ThO_2-UO_2 Solid Solutions," J. Nucl. Mat. 34, 315-324 (1970).

148. S. Aronson, R. B. Roof, Jr., and J. Belle, "Kinetic Study of the Oxidation of Uranium Dioxide," J. Chem. Phys. 27, 137-144 (1957).

149. L. N. Grossman and A. I. Kaznoff, "Insulators for Thermionic Energy Converter Application," pp. 421-423 in Proceedings of the Conference on Nuclear Applications of Nonfissionable Ceramics, Washington, D. C. May 9-11, 1966, American Nuclear Society, Hindsdale, Ill. June 1966.

150. E. L. Reed, "Stability of Refractories in Liquid Metals," J. Am. Ceram. Soc. 37, 146-153 (1954).

151. D. Kolar, "Heats of Immersion of Uranium Dioxide in Water," Croat Chem. Acta 35, 123-127 (1963).

152. H. F. Holmes and C. H. Secoy, "Heats of Immersion in the Thorium Oxide Water System," J. Phys. Chem. 69, 151-158 (1965).

153. H. F. Holmes, E. L. Fuller, Jr., and C. H. Secoy, "Heats of Immersion in the Thorium Oxide-Water System. II. Net Differential Heats of Adsorption," J. Phys. Chem. 70, 436-444 (1966).

154. E. L. Fuller, Jr., H. F. Holmes, C. H. Secoy, and J. E. Stuckey, "Heats of Immersion in the Thorium Oxide-Water System. III. Variation With Specific Surface Area and Outgassing Temperature," J. Phys. Chem. 72, 573-577 (1968).

155. D. T. Livey and P. Murray, "Surface Energies of Solid Oxides and Carbides," J. Am. Ceram. Soc. 39, 363-372 (1956).

156. E. L. Fuller, Jr., H. F. Holmes, and C. H. Secoy, "Gravimetric Adsorption Studies of Thorium Oxide. II. Water Adsorption at 25.0°," J. Phys. Chem. 70, 1633-1636 (1966).

157. H. F. Holmes, E. L. Fuller, Jr., and C. H. Secoy, "Gravimetric Adsorption Studies on Thorium Oxide. III. Adsorption of Water on Porous and Non-porous Samples," J. Phys. Chem. 72, 2293-2300 (1968).

158. R. B. Gammage, W. S. Brey, Jr., and B. H. Davis, "Adsorption of Water Vapor by Thorium Oxide and the Effects of Water on the Oxide," J. Colloid Interface Sic. 32, 256-269 (1970).

159. E. L. Fuller, Jr., H. F. Holmes, and R. B. Gammage, "Infrared Studies of Thorium Oxide Surface," ORNL-4378, March 1969.

160. J. C. Clayton, "Thorium Oxide Powder Properties which are Important to ThO_2 and ThO_2-UO_2 Fuel Pellet Fabrication," WAPD-TM-1230, January 1976.

161. R. K. Webster, T. L. Jones, and P. J. Anderson, "Proton Magnetic Resonance Studies of Adsorbed Water on Magnesium Oxide," Proc. Brit. Ceram. Soc. 5, 153-165 (1965).

162. P. J. Anderson, R. F. Horlock, and J. F. Oliver "Interaction of Water with the Magnesium Oxide Surface," Trans. Faraday Soc. 61, 2754-2760 (1965).

163. C. S. Shoup and C. H. Secoy, Private Communication quoted in Reference 158.

TABLE 1. BRAGG ANGLE (DEGREES) AND INTENSITY VALUES FOR PURE THORIA IN MOST-USED X-RAY WAVELENGTHS

	HKL		D, Angstroms	Cu Kα		Fe Kα		Cr Kα	
				2 Theta	I	2 Theta	I	2 Theta	I
1	1	1	3.23172	27.58	100.00	34.86	100.00	41.50	100.00
2	0	0	2.79875	31.95	48.82	40.47	48.13	48.29	47.52
2	2	0	1.97902	45.81	42.56	58.57	40.34	70.69	39.53
3	1	1	1.68771	54.31	54.66	70.00	51.87	85.43	54.7
2	2	2	1.61586	56.94	16.58	73.61	15.88	90.23	17.5
4	0	0	1.39938	66.80	7.22	87.54	7.58	109.79	11.1
3	3	1	1.28415	73.72	24.54	97.84	29.59	126.13	59.6
4	2	0	1.25164	75.96	21.83	101.32	27.91	132.32	64.35
4	2	2	1.14258	84.78	18.18	115.82	31.26	0.00	0.00
5	1	1	1.07724	91.29	20.87	127.95	48.03	0.00	0.00
3	3	3	1.07724	91.29		127.95		0.00	
4	4	0	0.98951	102.24	7.05	156.08	39.34	0.00	0.00
5	3	1	0.94615	109.00	28.91	0.00	0.00	0.00	0.00
6	0	0	0.93292	111.31	18.31	0.00	0.00	0.00	0.00
4	4	2	0.93292	111.31		0.00		0.00	
6	2	0	0.88504	120.99	15.25	0.00	0.00	0.00	0.00
5	3	3	0.85361	128.94	18.51	0.00	0.00	0.00	0.00
6	2	2	0.84385	131.79	18.92	0.00	0.00	0.00	0.00
4	4	4	0.80793	144.88	8.95	0.00	0.00	0.00	0.00

"0.00" Entries indicate that peak cannot be obtained in this radiation.

TABLE 1. (Cont)

	HKL		D, Angstroms	Mo Kα 2 Theta	Mo Kα I	Ni Kα 2 Theta	Ni Kα I	Co Kα 2 Theta	Co Kα I
1	1	1	3.23172	12.60	100.00	29.73	100.00	32.14	100.00
2	0	0	2.79875	14.56	49.87	34.46	48.62	37.28	48.39
2	2	0	1.97902	20.65	47.09	49.53	41.84	53.74	41.08
3	1	1	1.68771	24.26	63.61	58.84	53.50	64.01	52.48
2	2	2	1.61586	25.36	19.58	61.73	16.23	67.22	15.96
4	0	0	1.39938	29.36	8.88	72.65	7.14	79.46	7.21
3	3	1	1.28415	32.06	30.46	80.41	24.82	88.30	26.13
4	2	0	1.25164	32.92	27.03	82.95	22.30	91.23	23.91
4	2	2	1.14258	36.17	21.65	93.02	19.65	103.05	23.14
5	1	1	1.07724	38.44	23.33	100.62	23.92	112.27	30.80
3	3	3	1.07724	38.44		100.62		112.27	
4	4	0	0.98951	42.01	6.60	113.81	9.14	129.37	14.30
5	3	1	0.94615	44.03	23.25	122.36	41.04	141.96	77.64
6	0	0	0.93292	44.69	13.90	125.39	26.90	146.99	56.28
4	4	2	0.93292	44.69		125.39		146.99	
6	2	0	0.88504	47.25	8.86	138.99	26.95	0.00	0.00
5	3	3	0.85361	49.10	8.41	152.39	43.34	0.00	0.00
6	2	2	0.84385	49.70	7.83	158.43	54.02	0.00	0.00
4	4	4	0.80793	52.08	2.32	0.00	0.00	0.00	0.00

"0.00" Entries indicate that peak cannot be obtained in this radiation.

TABLE 2. CALCULATIONS OF LATTICE ENERGY OF UO_2 and ThO_2 BY THE BORN-HABER CYCLE

Symbol from Equation 1	Childs (Ref. 5)		Benson, et al (Ref. 6)	
	UO_2	ThO_2	UO_2	ThO_2
H	-258.4	-292.1	-342	-270
L	116.6	134.7	117	153
D	117.2	117.2	117	117
A	-179	-179	-170	-170
$\sum I_i$	1611	1511	1515	1515
Lattice Energy, Kcal/mole	-2461	-2413	-2431	-2398

TABLE 3. SUMMARY OF CERTAIN PROPERTIES OF THE CRYSTAL STRUCTURES OF UO_2 AND ThO_2

	UO_2	ThO_2
Space Group	Fm3m	Fm3m
Cell Size, Å, 25°C	5.4605	5.5975
Theoretical Density, g/cm^3	10.97	10.00
Inter-atomic Distances,		
M-M	2.735	2.799
O-O	3.868	3.958
M-O	2.518	2.576
Lattice Energy, kcal/mole	-2431	-2398

TABLE 4. VEGARD'S LAW COEFFICIENTS (ANGSTROMS) FOR FLUORITE-TYPE OXIDE SOLID SOLUTIONS

Measured on pure dioxide end-members

Th	5.5975
U^{+4}	5.4705
Pr	5.394
Ce	5.408
Am	5.376
Cm	5.372
Pa	5.505
Np	5.434
Pu	5.396
Tb	5.220
Hf	5.115

Extrapolated from measurements on solid solutions

Zr	5.163
Y	5.235
U^{+5}	5.400
U^{+6}	5.49
Sm	5.539
Eu	5.512
Ca	5.331
Gd	5.126
□	-0.061

Calculated from tabulated ionic radii (radii of +4 ions assumed 0.866 of +3 ions)

Nd	5.35
Pm	5.39
Dy	5.11
Ho	5.09
Er	5.01
Tm	5.01
Yb	4.99
Lu	4.97

TABLE 5. LATTICE CONSTANTS AND THEORETICAL DENSITIES OF UO_2-ThO_2 SOLID SOLUTIONS

Composition (mole % UO_2)	Lattice Parameter* (Å)	Theoretical density (g/cm^3)
100	5.4704	10.96
90.1	5.4841	10.85
80.1	5.4969	10.75
69.9	5.5098	10.65
60.1	5.5225	10.55
50.1	5.5355	10.46
40.3	5.5475	10.37
30.1	5.5590	10.28
20.2	5.5726	10.18
10.1	5.5846	10.09
0	5.5975	10.00

*Standard error of deviation ± 0.0003 Å.

TABLE 6. LATTICE CONSTANTS OF HIGH UO_2-LOW ThO_2 SOLID SOLUTIONS

Mole % UO_2	a_o, Å
94.9	5.4783
95.4	5.4775
96.0	5.4768
96.5	5.4756
97.0	5.4752
97.3	5.4744
97.8	5.4735
98.1	5.4704

TABLE 7. COMPARISON OF X-RAY LATTICE PARAMETER MEASUREMENTS WITH DILATOMETRIC MEASUREMENTS

Temperature, °C	Lattice Parameter, Å	% Increase	
		a_o	Dilatometry
20	5.5963	-	-
200	5.6048	0.15	0.13
400	5.6146	0.33	0.30
600	5.6248	0.51	0.49
800	5.6353	0.70	0.70
1000	5.6463	0.89	0.92
1200	5.6576	1.04	1.14
1400	5.6693	1.30	1.37
1600	5.6814	1.52	1.60
1800	5.6938	1.74	1.84
2000	5.7066	1.97	2.08

TABLE 8. THERMAL EXPANSION VALUES FOR ThO_2, ThO_2-10 w/o UO_2, AND ThO_2-20 w/o UO_2

Temperature, °C	Linear Expansion, Percent		
	ThO_2	ThO_2-10 w/o UO_2	ThO_2-20 w/o UO_2
20	-	-	-
200	0.13	0.17	0.16
400	0.30	0.36	0.35
600	0.49	0.57	0.55
800	0.70	0.77	0.76
1000	0.92	0.99	0.99
1200	1.14	1.21	1.22
1400	1.37	1.44	1.47
1600	1.60	1.67	1.72
1800	1.84	1.90	1.98
2000	2.08	2.14	2.24

TABLE 9. VALUES FOR β IN THE MAXWELL-EUCKEN EQUATION
(According to References 32 and 35)

Temperature, °K	Density, % of Theoretical				
	97	96	95	94	93
1200	1.174	1.173	1.172	1.172	1.171
1300	1.163	1.162	1.161	1.160	1.159
1400	1.152	1.151	1.150	1.149	1.148
1500	1.141	1.140	1.139	1.138	1.137
1600	1.130	1.129	1.128	1.127	1.125
1700	1.120	1.118	1.117	1.116	1.114
1800	1.109	1.108	1.106	1.105	1.104
1900	1.098	1.097	1.096	1.094	1.093
2000	1.088	1.087	1.085	1.084	1.082
2100	1.078	1.076	1.075	1.073	1.071
2200	1.067	1.066	1.064	1.063	1.061
2300	1.057	1.056	1.054	1.052	1.050
2400	1.047	1.045	1.044	1.042	1.040

TABLE 10. THERMAL CONDUCTIVITY (W/cm°C) OF 100 PERCENT DENSE ThO_2-UO_2
(According to Equations of Reference 32)

Temperature, °C		Mole Percent UO_2							
		0	2	5	10	15	20	25	30
25		0.1571	0.1453	0.1372	0.1323	0.1399	0.1376	0.1264	0.1100
100		0.1294	0.1204	0.1136	0.1080	0.1103	0.1080	0.1015	0.0923
200		0.1047	0.0980	0.0924	0.0867	0.0861	0.0839	0.0804	0.0760
300		0.0879	0.0827	0.0779	0.0725	0.0706	0.0686	0.0666	0.0645
400		0.0758	0.0715	0.0673	0.0622	0.0598	0.0580	0.0568	0.0561
500		0.0666	0.0630	0.0592	0.0545	0.0519	0.0503	0.0495	0.0496
600		0.0594	0.0563	0.0529	0.0485	0.0458	0.0443	0.0439	0.0445
800		0.0488	0.0464	0.0436	0.0398	0.0371	0.0359	0.0358	0.0369
1000		0.0414	0.0394	0.0371	0.0337	0.0312	0.0301	0.0302	0.0315
1200		0.0360	0.0343	0.0322	0.0292	0.0269	0.0260	0.0261	0.0274
1400	*	0.0318	0.0304	0.0285	0.0258	0.0237	0.0228	0.0230	0.0243
1600	*	0.0285	0.0272	0.0256	0.0231	0.0211	0.0203	0.0206	0.0219
1800	*	0.0258	0.0247	0.0232	0.0209	0.0191	0.0184	0.0186	0.0198
2000	*	0.0236	0.0226	0.0212	0.0191	0.0174	0.0167	0.0170	0.0182

*Exclusive of any radiative contribution.

TABLE 11. THERMODYNAMIC FUNCTIONS OF ThO_2

Temperature, °K	C_p°, Heat Capacity, cal/mole °K	$H^\circ - H_o^\circ$, Enthalpy, cal/mole	S°, Entropy, cal/mole °K	$-(G^\circ - H_o^\circ)/T$, cal/mole °K
10.00	0.032	0.08	0.011	0.003
50.00	2.430	38.60	1.068	0.296
100.00	6.246	257.3	3.948	1.375
150.00	9.546	655.1.	7.129	2.762
200.00	11.97	1196.5	10.227	4.244
250.00	13.64	1839.1	13.088	5.732
298.15	14.76	2524.4	15.593	7.126
300.00	14.79	2551	15.68	7.18
400.00	16.08	4103	20.14	9.88
500.00	16.80	5750	23.81	12.31
600.00	17.29	7456	26.92	14.49
700.00	17.68	9205	29.61	16.46
800.00	18.01	10990	32.00	18.26
900.00	18.30	12806	34.13	19.91
1000.00	18.58	14650	36.08	21.43
1100.00	18.84	16521	37.86	22.85
1200.00	19.09	18417	39.15	24.17
1300.00	19.34	20338	41.05	25.40
1400.00	19.58	22284	42.49	26.58
1500.00	19.81	24254	43.85	27.68
1600.00	20.05	26247	45.13	28.73
1700.00	20.28	28264	46.36	29.74
1800.00	20.51	30304	47.52	30.69
1900.00	20.74	32366	48.64	31.60
2000.00	20.97	34452	49.71	32.48
2100.00	21.20	36561	50.74	33.33
2200.00	21.43	38693	51.73	34.14
2300.00	21.66	40847	52.69	34.92
2400.00	21.88	43024	53.61	35.69
2500.00	22.11	45224	54.51	36.42
2600.00	22.34	47446	55.38	37.13
2700.00	22.56	49691	56.23	37.83
2800.00	22.79	51958	57.05	38.50
2900.00	23.01	54248	57.86	39.19
3000.00	23.24	56560	58.64	39.79

TABLE 12. HEAT AND FREE ENERGY OF FORMATION OF ThO_2

Temperature, °K	$-\Delta H_f$, kcal/mole	$-\Delta G_f$, kcal/mole
298.15	293.2	279.4
400	293.0	274.7
500	292.8	270.2
600	292.6	265.7
700	292.4	261.2
800	292.2	256.8
900	292.0	252.4
1000	291.8	248.0
1100	291.7	243.6
1200	291.6	239.0
1300	291.4	234.9
1400	291.3	230.6
1500	291.2	226.0
1600	291.1	221.9
1700	291.7	217.5
1800	291.6	213.2
1900	291.6	208.8
2000	296.0	204.3
2500	295.4	181.5
3000	294.2	158.8

TABLE 13. SPECIFIC HEAT VALUES FOR ThO_2, ThO_2-10 w/o UO_2, and ThO_2-20 w/o UO_2

Temperature, °C	Specific Heat of Oxide, cal/g°C		
	ThO_2	ThO_2-10 w/o UO_2	ThO_2-20 w/o UO_2
0	0.057_2	0.056_5	0.056_1
100	0.060_7	0.061_1	0.061_5
200	0.062_7	0.063_5	0.064_2
400	0.065_5	0.066_8	0.067_2
600	0.067_7	0.068_0	0.069_1
800	0.069_7	0.069_6	0.070_7
1000	0.071_6	0.071_1	0.072_2
1200	0.073_5	0.072_5	0.073_5
1400	0.075_4	0.073_8	0.074_9
1600	0.077_2	0.075_2	0.076_2
1800	0.079_1	0.076_5	0.077_5
2000	0.080_9	0.077_8	0.078_7

TABLE 14. PARTIAL MOLAR THERMODYNAMIC QUANTITIES FOR SOLUTION OF OXYGEN AT 1250°K IN $Th_{1-y}U_yO_{2+x}$

(From Reference 53)

y	x	$-\bar{G}_{O_2}$, kcal/mole	$-\bar{S}_{O_2}$, cal/mole °K	$-\bar{H}_{O_2}$ kcal/mole
0.90	0.042	51.8	8	62
0.90	0.042	52.4	13	69
0.90	0.076	48.7	17	70
0.90	0.081	48.4	17	70
0.90	0.123	44.7	23	73
0.90	0.126	44.7	21	71
0.90	0.157	40.7	29	77
0.71	0.046	50.9	14	68
0.71	0.049	50.9	14	68
0.71	0.084	47.2	21	74
0.71	0.092	46.9	28	82
0.71	0.121	44.0	34	85
0.71	0.133	42.9	29	80
0.71	0.152	40.3	34	83
0.71	0.154	40.2	35	84
0.52	0.044	47.5	20	72
0.52	0.045	46.8	22	74
0.52	0.079	43.4	22	72
0.52	0.087	44.4	31	83
0.52	0.119	39.8	35	84
0.52	0.122	39.5	34	82
0.52	0.152	35.7	40	85
0.52	0.152	35.2	35	78
0.29	0.019	45.4	22	72
0.29	0.027	43.2	19	67
0.29	0.046	37.3	24	67
0.29	0.053	36.2	26	69
0.29	0.053	36.8	30	74
0.29	0.069	33.5	30	71
0.29	0.073	33.1	34	76

TABLE 15. VOLATILITY OF UO_3 AT 1200 TO 1600°C AND UO_2 ACTIVITY AT 1300°C FOR $Th_{1-y}U_yO_{2+x}$

(Reference 55)

Composition				
2 + x	2.24	2.13	2.10	2.03
y	0.5	0.25	0.20	0.063
Partial pressure, stm				
in P = A - B/T,A	15.20	13.02	11.43	8.32
in P = A - B/T,B	42,568	39,808	37,313	33,198
Heat of sublimation				
Value, cal/mole	84,580	79,100	74,143	65,960
Standard deviation	1,400	800	1,500	1,900
Entropy of sublimation				
Value, cal/mole °K	30.20	25.87	22.71	16.53
Standard deviation	0.85	0.45	0.95	1.2
UO_2 activity in 0.2 atm O_2 at 1300°C				
For given composition	0.091	0.061	0.059	0.036
Corrected to x = 0	0.5	0.24	0.20	0.05
UO_2 activity coefficient				
for x = 0	1.0	0.96	1.0	0.83

TABLE 16. CATION VOLUME DIFFUSION IN ThO_2, ThO_2-UO_2, and UO_2

Diffusing Cation	HOST Lattice	Activation Energy for Volume Diffusion, kcal/mole	Reference
U^{+4}	UO_2	98.3	Reimann and Lundy
U^{+4}	ThO_2-UO_2	85.9	Furuya
U^{+4}	ThO_2	76.4	Furuya
Th^{+4}	ThO_2	149.5	King
Pa^{+4}	UO_2	107.6	Schmitz and Landner
Pa^{+4}	ThO_2-UO_2	91.8	Furuya and Yajima
Pa^{+4}	ThO_2	75.4	Furuya and Yajima

TABLE 17. DIFFUSION OF NON-VOLATILE FISSION PRODUCTS IN UO_2 AND ThO_2

Matrix	Fission Product	Integrated flux, n/cm^2	Temperature Range, °C	Q, kcal/mole	D_o, cm^2/sec
UO_2	Ru	1.8×10^{17}	800 to 970	94.9 ± 3.0	4.2
UO_2	Ru	1.8×10^{17}	690 to 800	32.4 ± 1.7	2.0×10^{-13}
UO_2	Zr	1.8×10^{17}	800 to 950	45.6 ± 1.9	1.2×10^{-9}
UO_2	Zr	1.1×10^{18}	720 to 950	52.5 ± 2.0	2.6×10^{-8}
UO_2	Nb	1.8×10^{17}	800 to 950	46.6 ± 2.0	1.2×10^{-8}
UO_2	Nb	1.1×10^{18}	720 to 950	55.4 ± 1.6	9.8×10^{-7}
U_3O_8	Ru	1.1×10^{18}	690 to 980	56.1 ± 1.6	1.1×10^{-4}
ThO_2	Zr	3.8×10^{17}	<840	20.0	
ThO_2	Zr	3.8×10^{17}	840 to 960	62.3 ± 7.4	6.9×10^{-7}
ThO_2	Nb	3.8×10^{17}	<820	22.0	
ThO_2	Nb	3.8×10^{17}	820 to 960	65.4 ± 5.5	8.3×10^{-6}
ThO_2	Ce	3.8×10^{17}	910 to 1010	70.0 ± 2.2	5.5×10^{-7}

TABLE 18. ELASTIC CONSTANTS OF SINGLE CRYSTAL OXIDES AT 25°C

	UO_2 (Reference 104)	ThO_2 (Reference 103)
C_{11} (10^{12} dynes/cm^2)	3.96	3.67
C_{12} (10^{12} dynes/cm^2)	1.21	1.06
C_{44} (10^{12} dynes/cm^2)	0.641	0.797
S_{11} (10^{-13} cm^2/dyne)	2.96	3.13
S_{12} (10^{-13} cm^2/dyne)	-0.697	-0.703
S_{44} (10^{-13} cm^2/dyne)	15.59	12.5
Anistotropy factor*	0.47	0.61
E_{100} (10^{12} dynes/cm^2)	3.38	3.20
E_{111} (10^{12} dynes/cm^2)	1.75	2.10

*Anisotropy factor = $2C_{44}/(C_{11} - C_{12})$ = 1.0 for isotropic crystal.

Note: 1 kilobar = 10^9 dynes/cm^2 = 14.5×10^3 psi.

TABLE 19. ISOTROPIC ELASTIC CONSTANTS FOR FULLY DENSE POLYCRYSTALLINE OXIDES AT 25°C

Oxide	Young's Modulus, E_S, kilobars	Shear Modulus, G_S, kilobars	Bulk Modulus, K_S, kilobars	Poisson's Ratio, μ_S	Experimental Method	References
ThO_2	2497	972	1930	0.284	Pulse-single crystal	Macedo, et al (Reference 103)
ThO_2*	2610	1006	2153	0.297	Resonance-polycrystal	Spinner, et al (Reference 109)
ThO_2†	2491	969	1928	0.285		
UO_2	2305	875	2127	0.316	Pulse-single crystal	Wachtman, et al (Reference 104)

*Values reported in reference from empirical fit of data to equation of form $E = E_S(1 + aP + bP^2)$.
†Values obtained by fitting data to linear equation of form $E = E_S(1 - cP)$.

Note: 1 kilobar = 10^9 dynes/cm^2 = 14.5×10^3 psi.

TABLE 20. MUTUAL INDENTATION HARDNESS OF CYLINDRICAL SAMPLES OF ThO_2

Batch 1: 96.5% TD, 17-micron Grain Diam.					Batch 2: 97.5% TD, 32-micron Grain Diam.				
Run No.	Temp, °C	Load, lb	Avg Indent Diam, d, mm	MIH, kg/mm^2	Run No.	Temp, °C	Load, lb	Avg Indent Diam, d, mm	MIH, kg/mm^2
248	1000	42.7	0.57	75.9	283	1010	32.8	0.53	76.5
243	1000	72.2	0.73	78.2	251	1010	32.6	0.63	47.5
238	1250	32.7	0.685	40.3	284	1010	52.5	0.70	62.0
234	1250	47.7	0.765	47.1	252	1010	52.5	0.74	55.4
228	1250	62.7	0.90	44.7	289	1010	63.5	0.73	68.8
226	1250	82.5	0.985	49.1	253	1015	82.5	0.94*	54.0
216	1515	28.4	0.765	28.0	254	1240	33.3	0.70	39.2
239	1515	33.1	0.85	26.5	255	1255	52.6	0.87	40.1
235	1515	48.4	0.93	32.3	285	1250	52.6	0.87	40.1
212	1505	52.6	0.915	36.3	290	1250	63.5	1.00*	36.7
217	1530	72.2	1.07	36.4	256	1255	81.7	0.97*	50.1
219	1805	32.7	0.935	21.6	265	1520	32.6	0.79	30.2
240	1795	32.9	0.90	23.5	258	1520	32.6	0.87	24.9
236	1815	47.5	1.09	23.1	266	1515	52.7	0.93	35.3
218	1800	52.6	1.00	30.4	286	1500	52.7	0.93	35.3
220	1800	82.5	1.30	28.2	249	1520	53.1	1.00	30.7
241	2000	32.7	0.985	19.5	275	1795	32.7	0.90	23.3
223	2010	33.3	1.01	18.9	276	1810	52.7	1.03	28.7
237	2000	47.5	1.14	21.1	281	1800	52.5	1.03	28.6
222	2000	53.3	1.27	19.1	287	1805	52.6	1.13	23.7
232	2000	91.9	1.60	20.7	267	1990	32.0	1.13†	14.5
					268	2000	32.2	1.17	13.6
					270	1990	52.3	1.43	14.8
					288	2005	52.5	1.43	14.9

*Diameter of all samples was 0.167 inch.
†Microcracking was observed.

TABLE 21. COMPARISON OF MUTUAL INDENTATION AND VICKERS HARDNESS TESTING WITH THE YIELD STRESS OF ThO_2

Temp, °C	σ_y,[1] psi	H_v,[2] kg/mm^2	H,[3] kg/mm^2	Computed Yield Stresses from Hardness Data, psi $\left(\frac{1420}{3.0} \times H_v\right)$	$\left(\frac{1420}{2.0} \times H\right)$
1000		122.5	80.6	56,400	57,000
1100	50,500	107.5		49,400	
1200		87.5		41,600	
1210	44,000				
1250			46.8		33,200
1300		74.5		33,300	
1325	37,500				
1400		62.7		28,700	
1425	29,500				
1500		58.2	35.3	26,700	25,800
1550	26,500				
1600		55.7		25,600	
1650	24,000				
1700		50.7		23,300	
1770	16,500				
1800		44.0	29.7	20,200	21,000
1850					
1900	13,500				
2000			14.4		10,200

(1) 97.5 percent TD, grain size - 10μ, $\dot{\varepsilon} = 3\ hr^{-1}$
(2) 97.5 percent TD, grain size - 32μ, $\dot{\varepsilon} = 15\ hr^{-1}$
(3) 97.5 percent TD, grain size - 32μ, $\dot{\varepsilon} = 12$ to $32\ hr^{-1}$

TABLE 22. EFFECT OF GRAIN SIZE AND POROSITY ON STRENGTH OF UO_2 AND ThO_2*

Material	Sinter Temp, °C	Type Test	Test Temp, °C	k x 10^{-3}	a	b
ThO_2	1650	Bend	RT	69.7	0.39	5.5
	1725	Bend	RT	69.7	0.39	4.7
	1800	Bend	RT	69.7	0.39	3.8
	1850	Bend	RT	69.7	0.39	3.7
	1800	Bend	1000	113.5	0.46	6.6
	1800	Comp	RT	1666.0	0.50	6.6
UO_2	2000	Bend	RT	23.7	0.119	3.17
	2000	Bend	1000	409.0	0.837	5.84

*Data from Knudsen and Knudsen, et al.

Note: $S = kG^{-a}e^{-bP}$

where S is strength in psi, G is average grain diameter in microns, and P is volume fraction porosity.

TABLE 23. SUMMARY OF RESULTS OF THERMAL STABILITY AND COMPRESSION TESTS ON ThO_2 PELLETS

Attributes of Pellets Tested		Re-sintering at 1750°C		Re-sintering at 1800°C		Crush Strength, psi	
Nominal Diameter, in.	Density Range % T.D.	Diametral Shrinkage, mils	Densification % T.D. Absolute	Diametral Shrinkage, mils	Densification % T.D. Absolute	Mean	Standard Deviation
0.255	94.9 - 98.5	0.1 - 0.3	0.12 - 0.50	0.1 - 0.4	0.10 - 0.35	75,878	7,602
0.510	96.4 - 99.1	0.1 - 0.9	0.05 - 0.53	0.1 - 0.8	0.02 - 0.89	81,039	3,455
0.742	96.0 - 98.1	0.5 - 1.3	0.10 - 0.60	-	-	89,214	1,359

TABLE 24. MOISTURE CONTENTS OF NLO-FABRICATED THORIA POWDERS

Lot* No.	BET Surface Area, m^2/g	Moisture, w/o	Adsorbed Monolayer*	4 Weeks' Exposure to Ambient Air		
				BET Surface Area, m^2/g	Moisture, w/o	Adsorbed Monolayer**
005	7.57	0.19	0.9	7.99	0.41	1.9
015	7.51, 7.70	0.13, 0.14	0.6	7.76	0.31	1.4
025	7.45, 7.64	0.11, 0.12	0.5	8.38	0.34	1.5
034	7.44, 7.49	0.15, 0.15	0.7	8.00	0.37	1.7
043	6.93, 7.04	0.17, 0.13	0.9	7.69	0.38	1.8
054	6.36, 6.89	0.20, 0.23	1.3	6.62	0.43	2.3

*Powder preparation and measurements were made over an 18 month period. Moisture measured by moisture analyzer technique.

**Calculated on the basis that a monomolecular layer of adsorbed water vapor is equivalent to 2.84×10^{-8} gH_2O/cm^2, i.e., the mass of one water molecule (3×10^{-23} g) divided by its area (10.6 A^2).

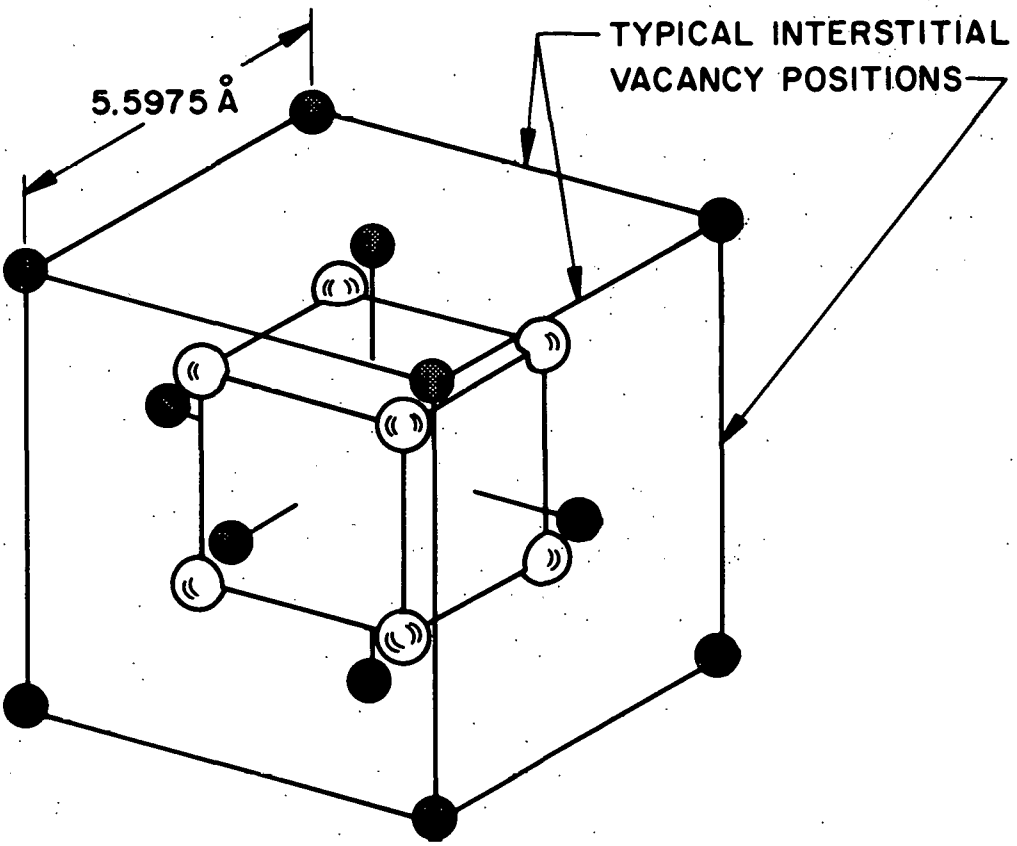

Figure 1. Crystal Structure of Thorium Dioxide

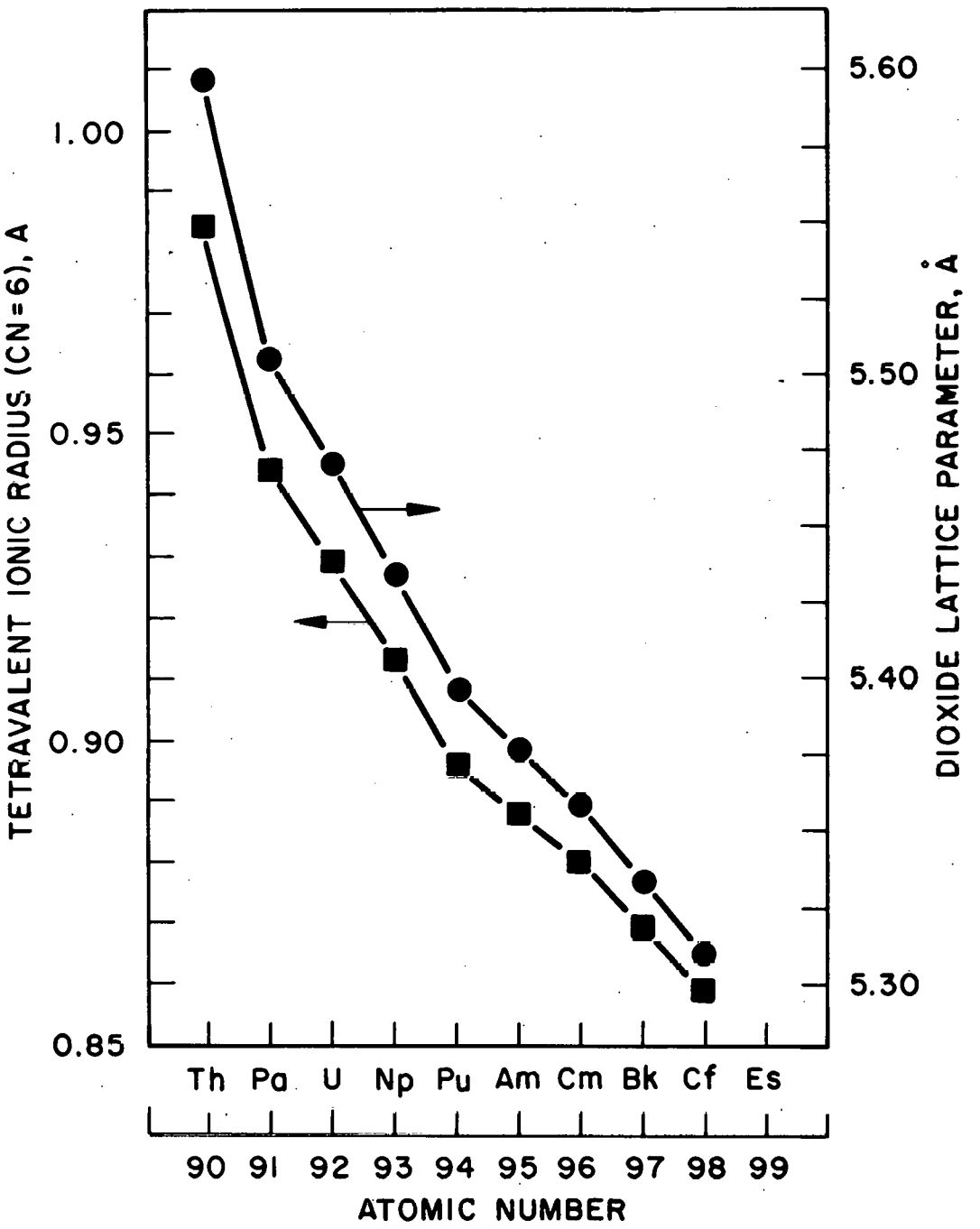

Figure 2. Radii of Quadrivalent Actinide Ions and Cell Sizes of Their Fluorite-Type Dioxides (From Reference 8)

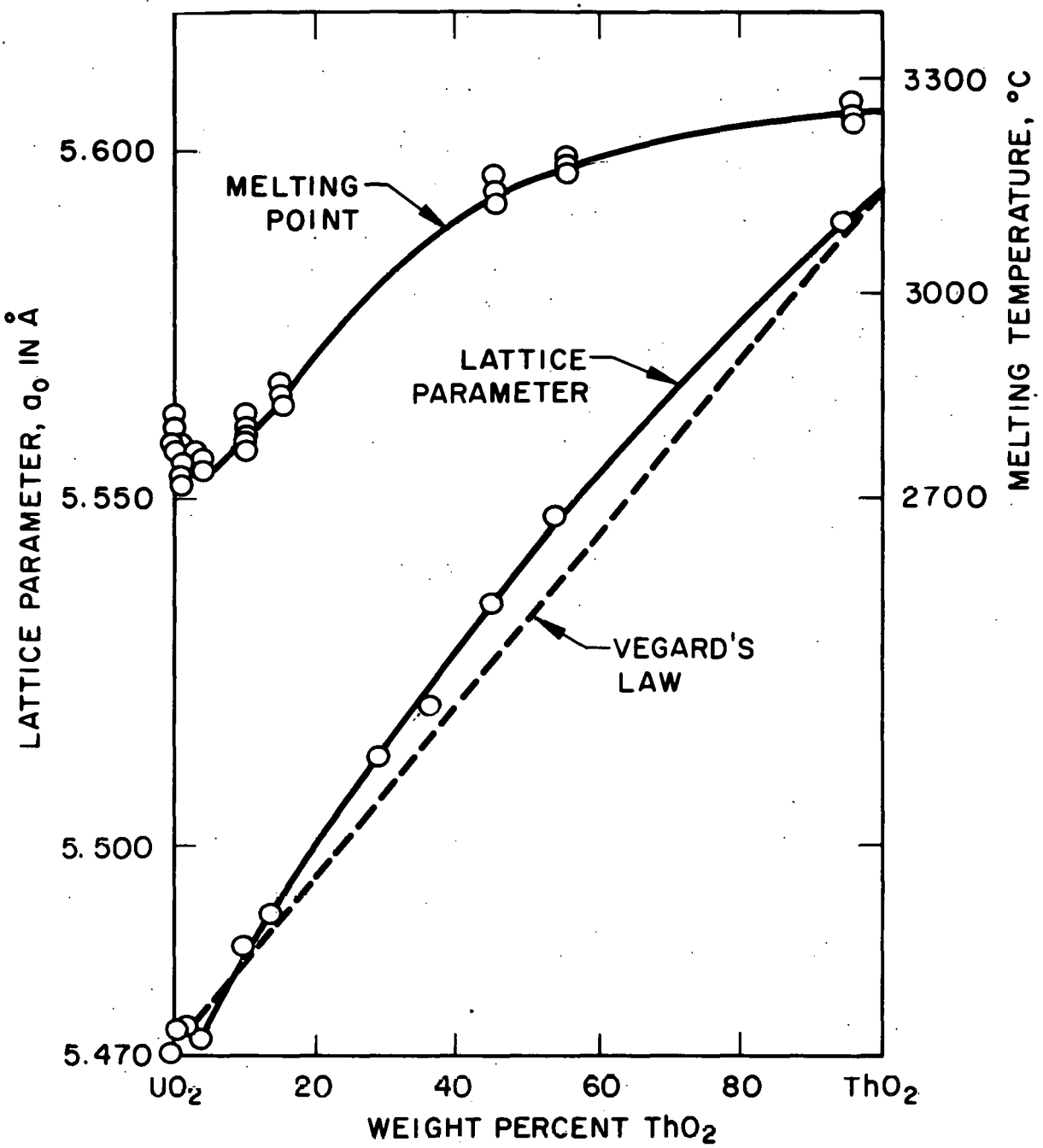

Figure 3. Phase Relationships for the UO_2-ThO_2 System According to Christensen

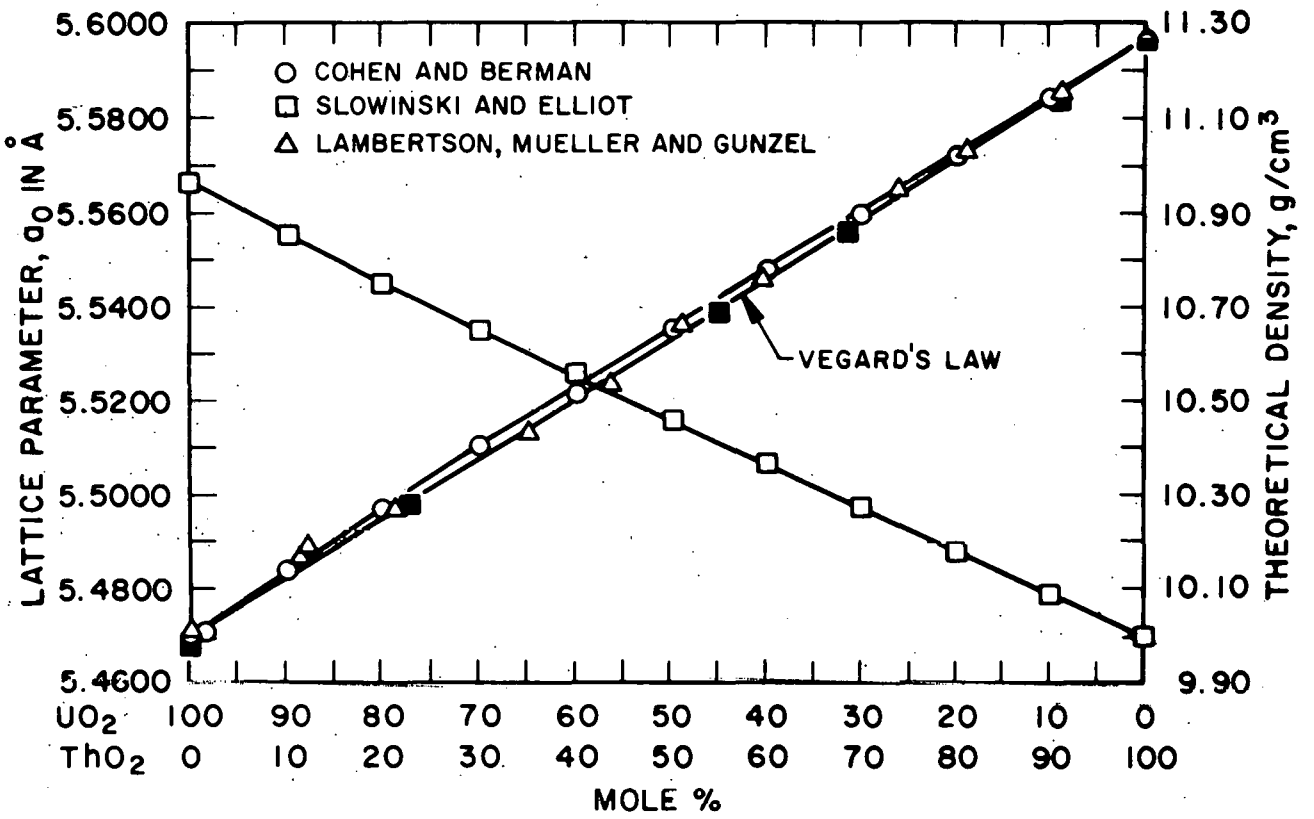

Figure 4. Lattice Parameter and Density of $U_yTh_{1-y}O_2$

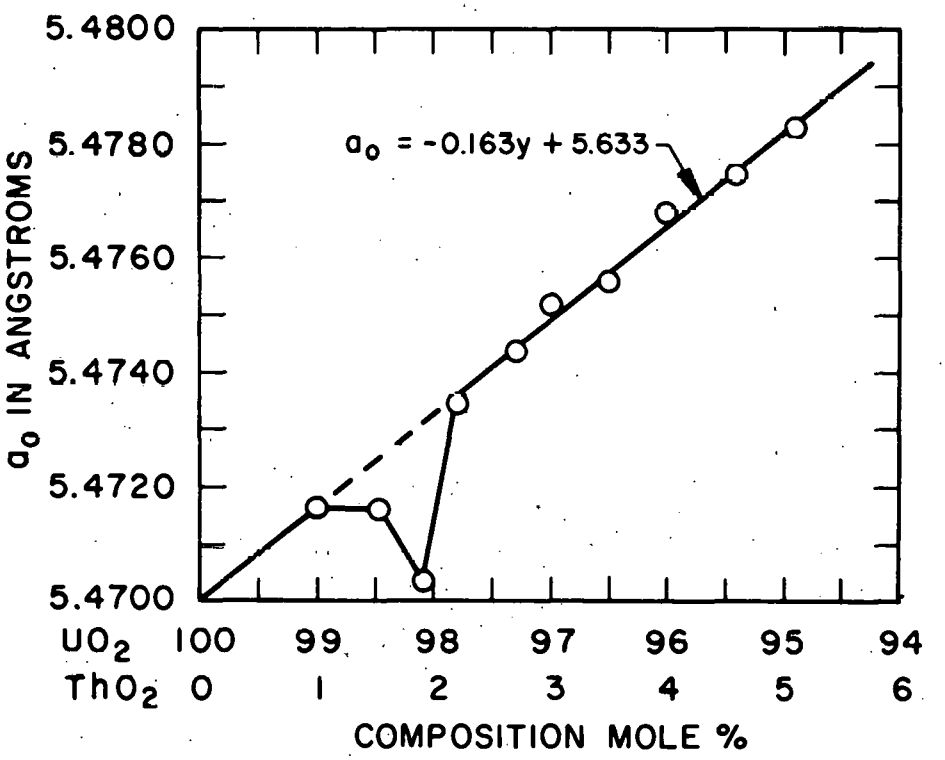

Figure 5. Anomalous Behavior of High UO_2 - Low ThO_2 Compositions

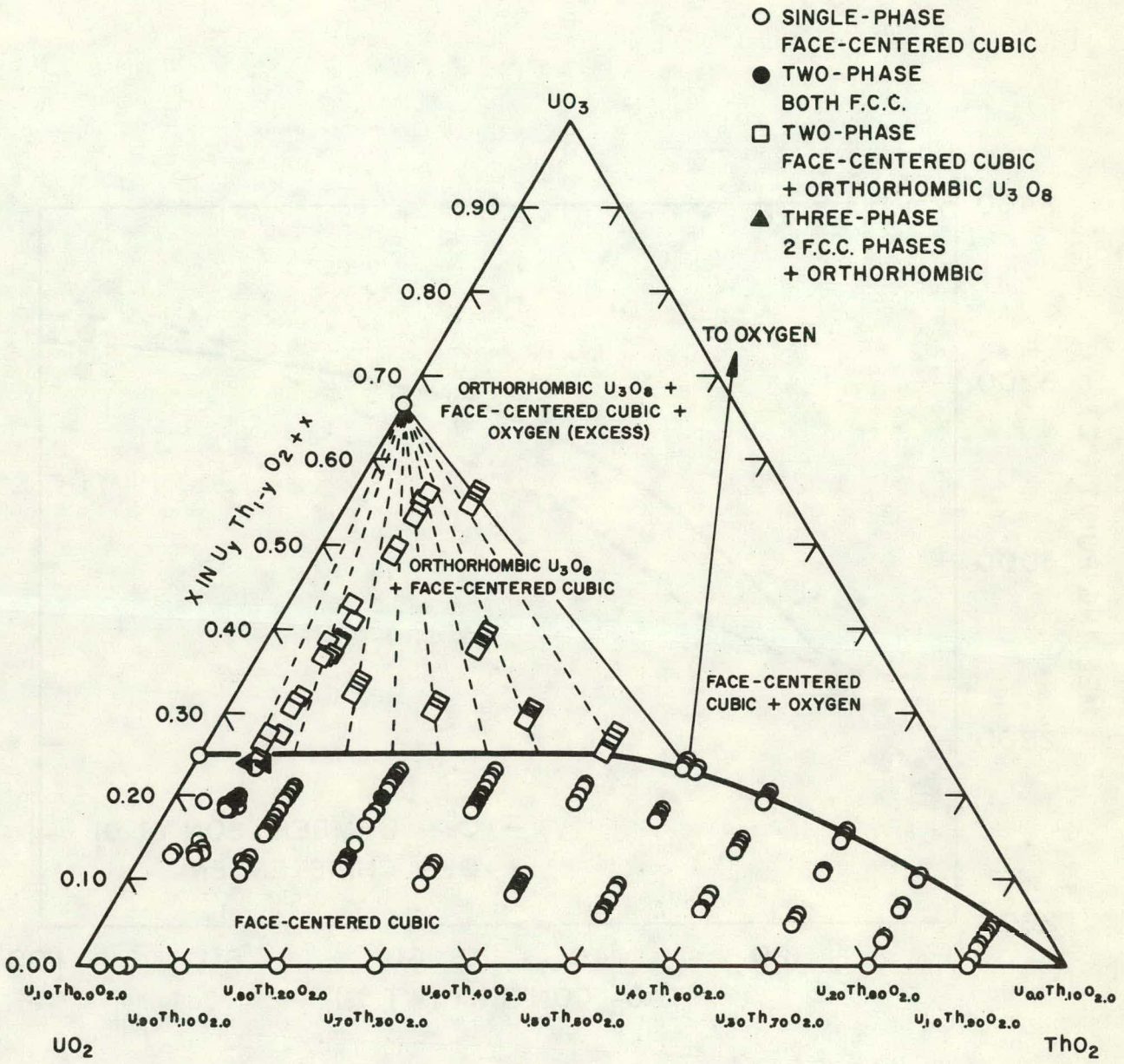

Figure 6. The UO_2-UO_3-ThO_2 Ternary at 1200°C, According to Reference 14 Showing the Wedge-Shaped Stability Region of the Face-Centered Cubic Phase

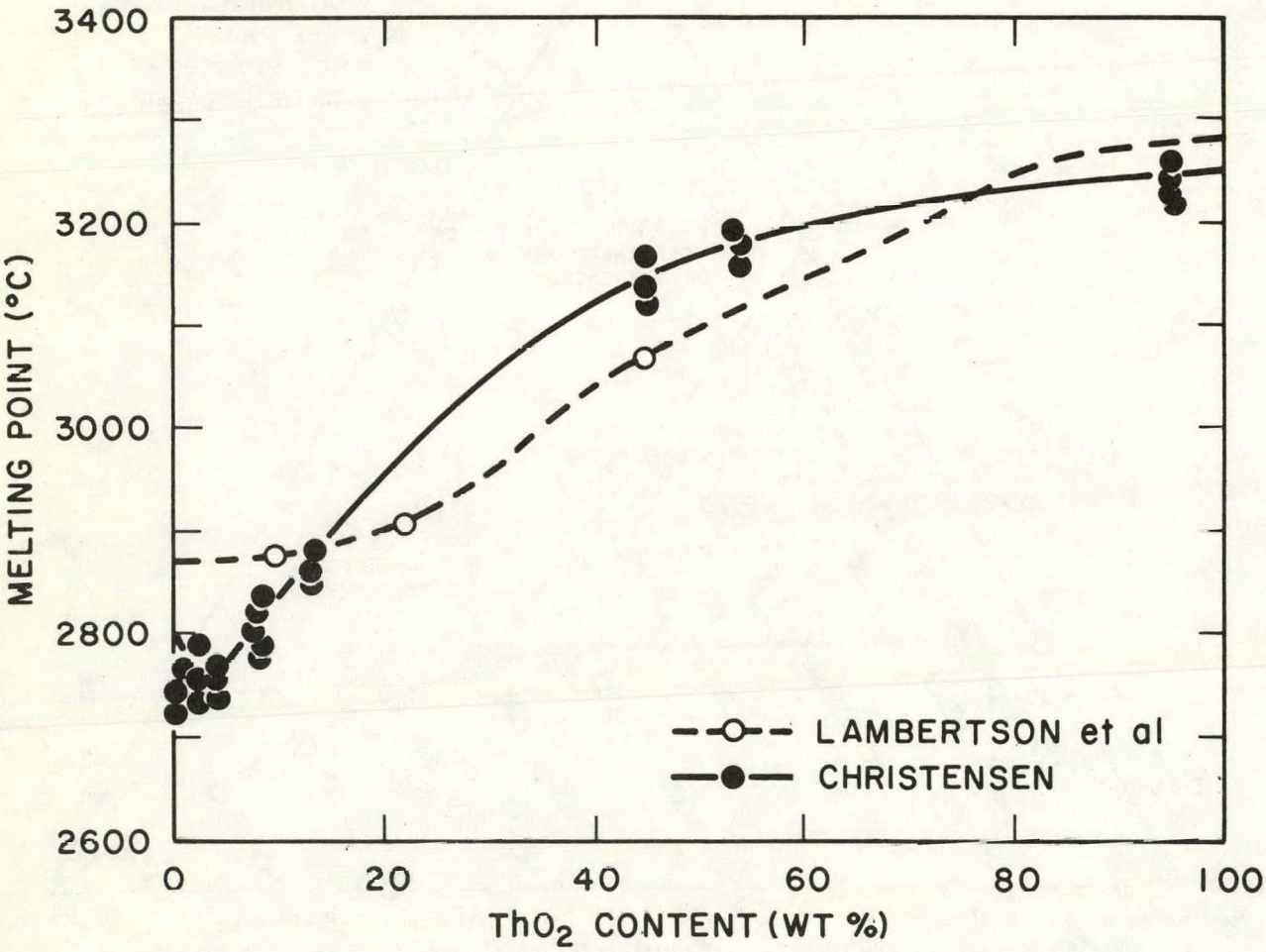

Figure 7. Melting Point of ThO_2-UO_2 (Data from Lambertson, et al and Christensen)

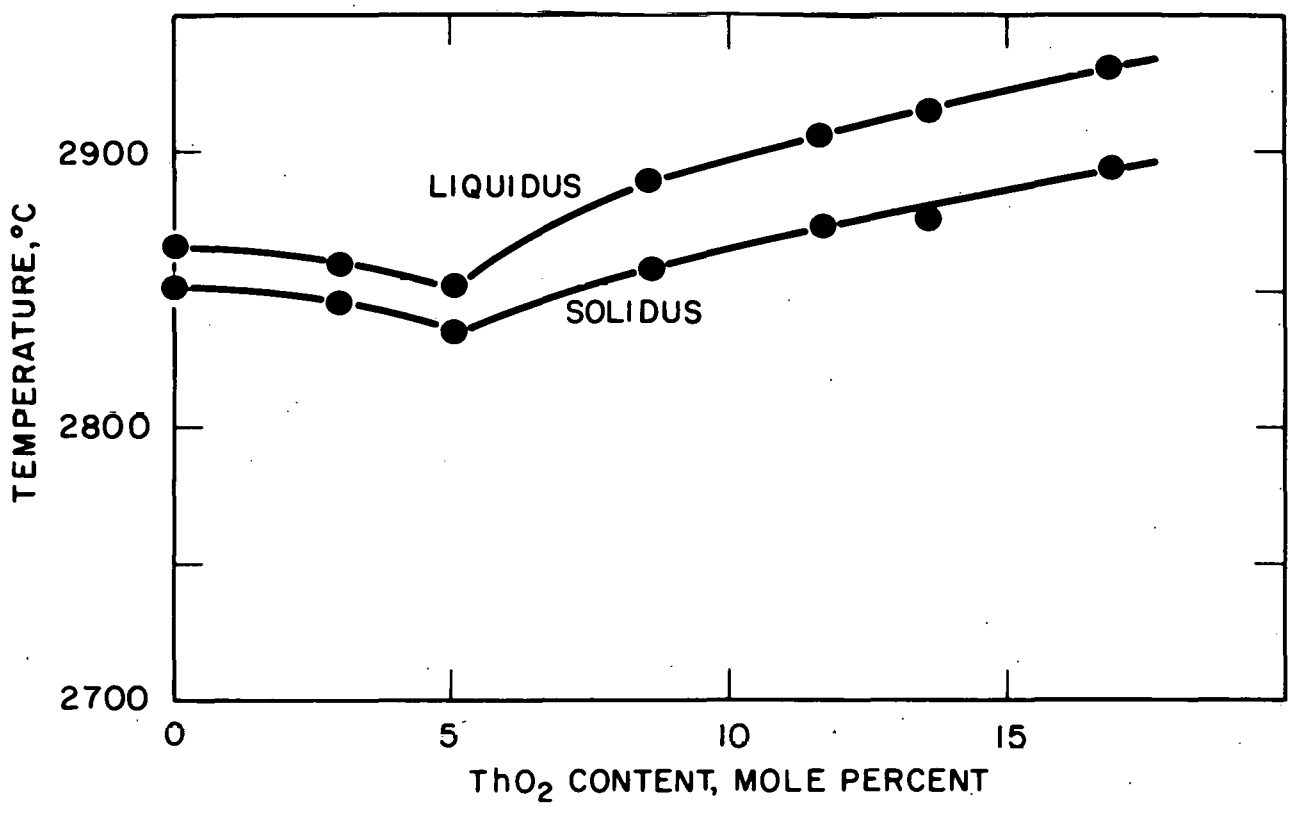

Figure 8. Solidus-Liquidus Temperatures in the UO_2-ThO_2 System (According to Latta, et al., Reference 21)

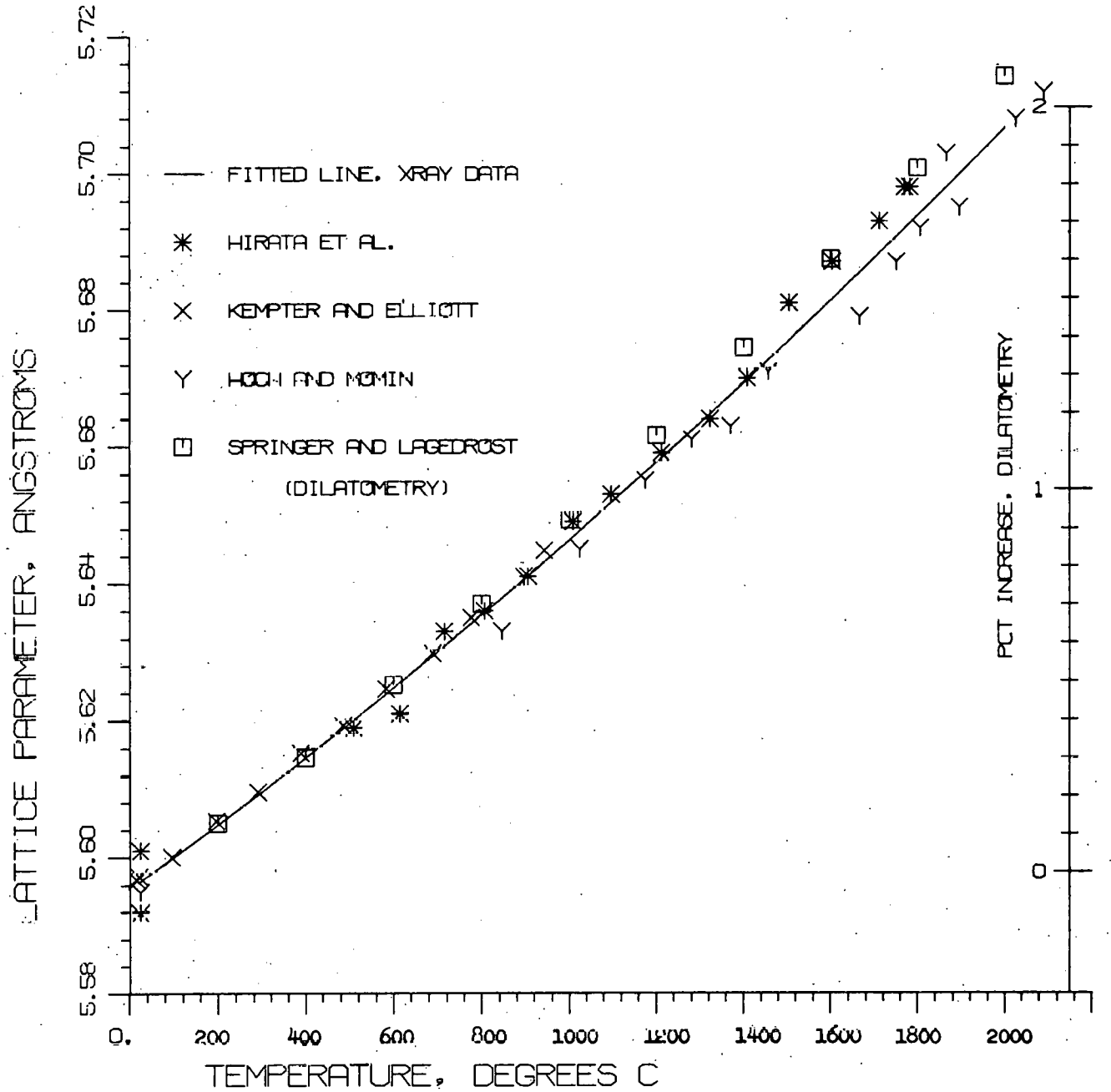

Figure 9. Thermal Expansion of Thoria

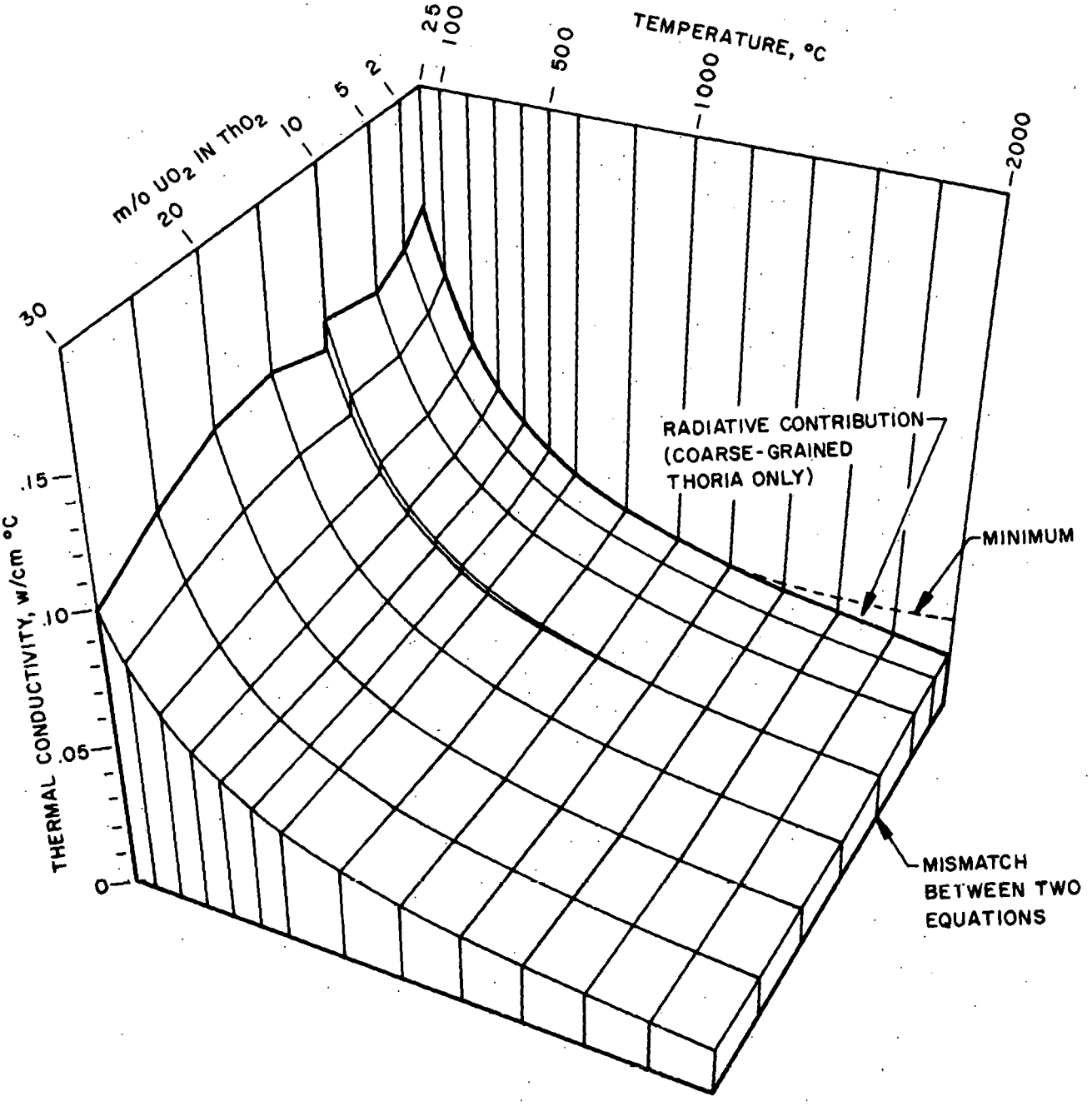

Figure 10. Thermal Conductivity of 100 Percent Dense ThO_2-UO_2 Solid Solutions, According to Equations in WAPD-TM-908

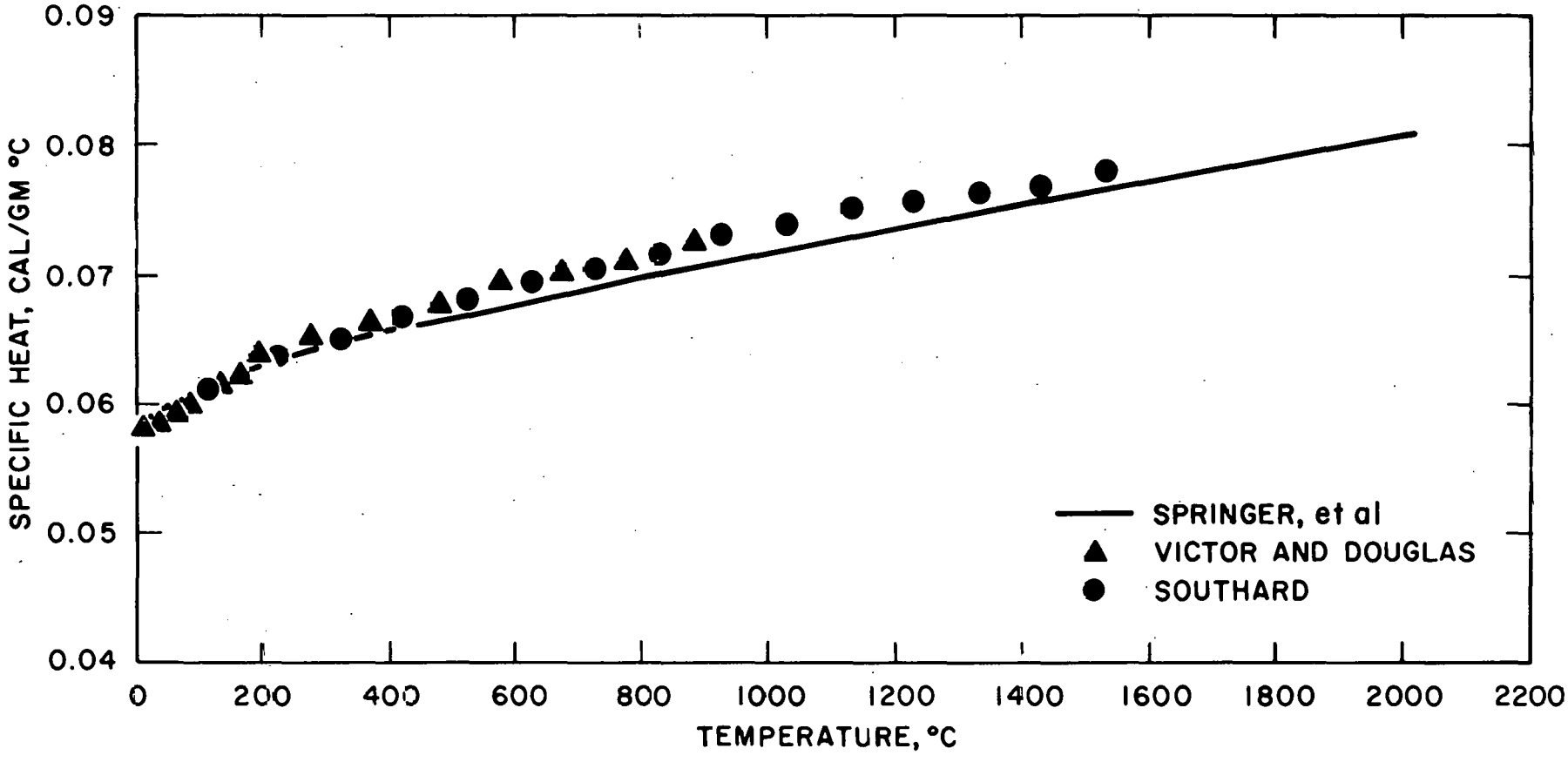

Figure 11. Specific Heat of ThO_2

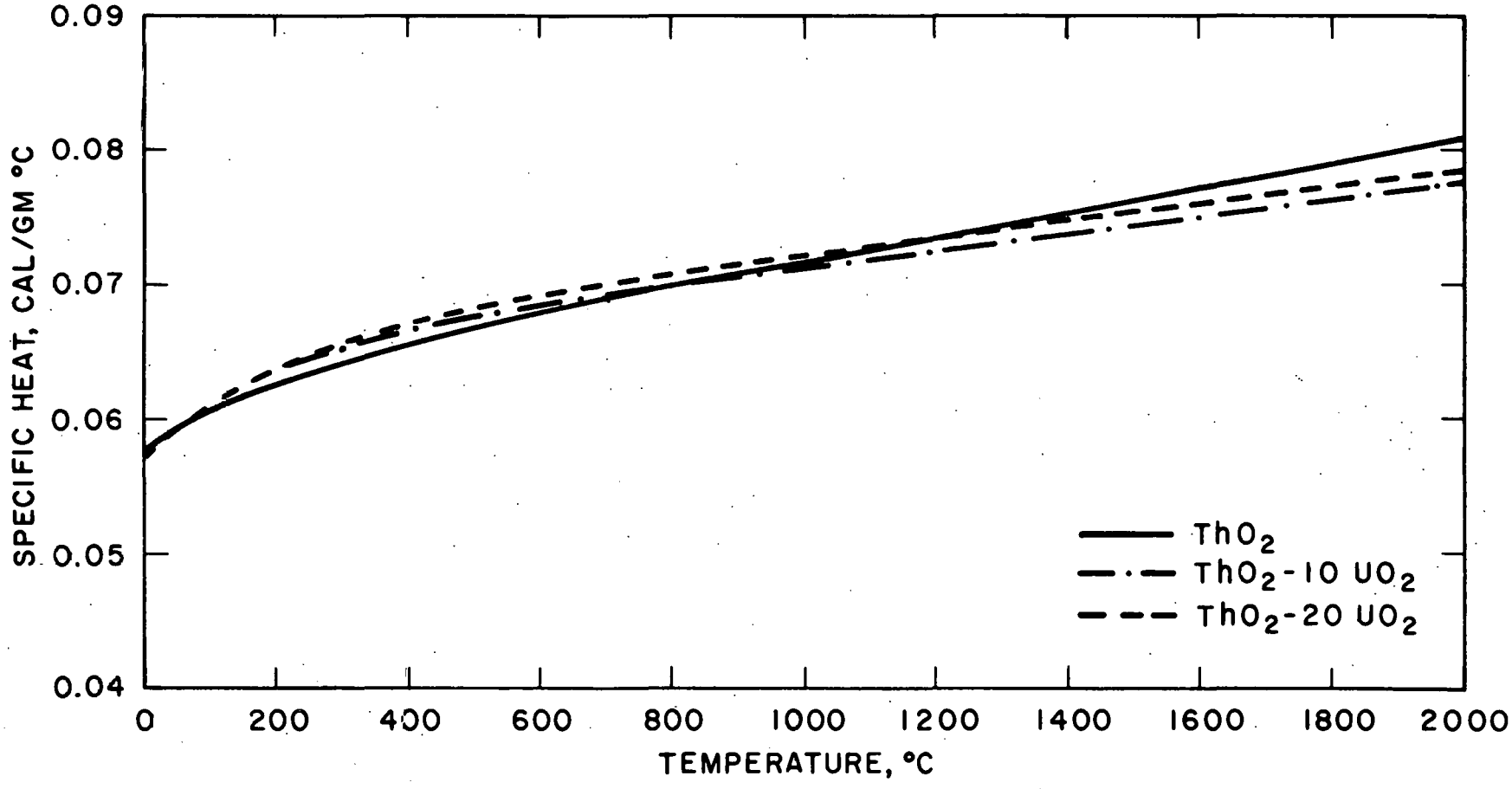

Figure 12. Composite of Specific Heat Curves for ThO_2 and ThO_2-UO_2

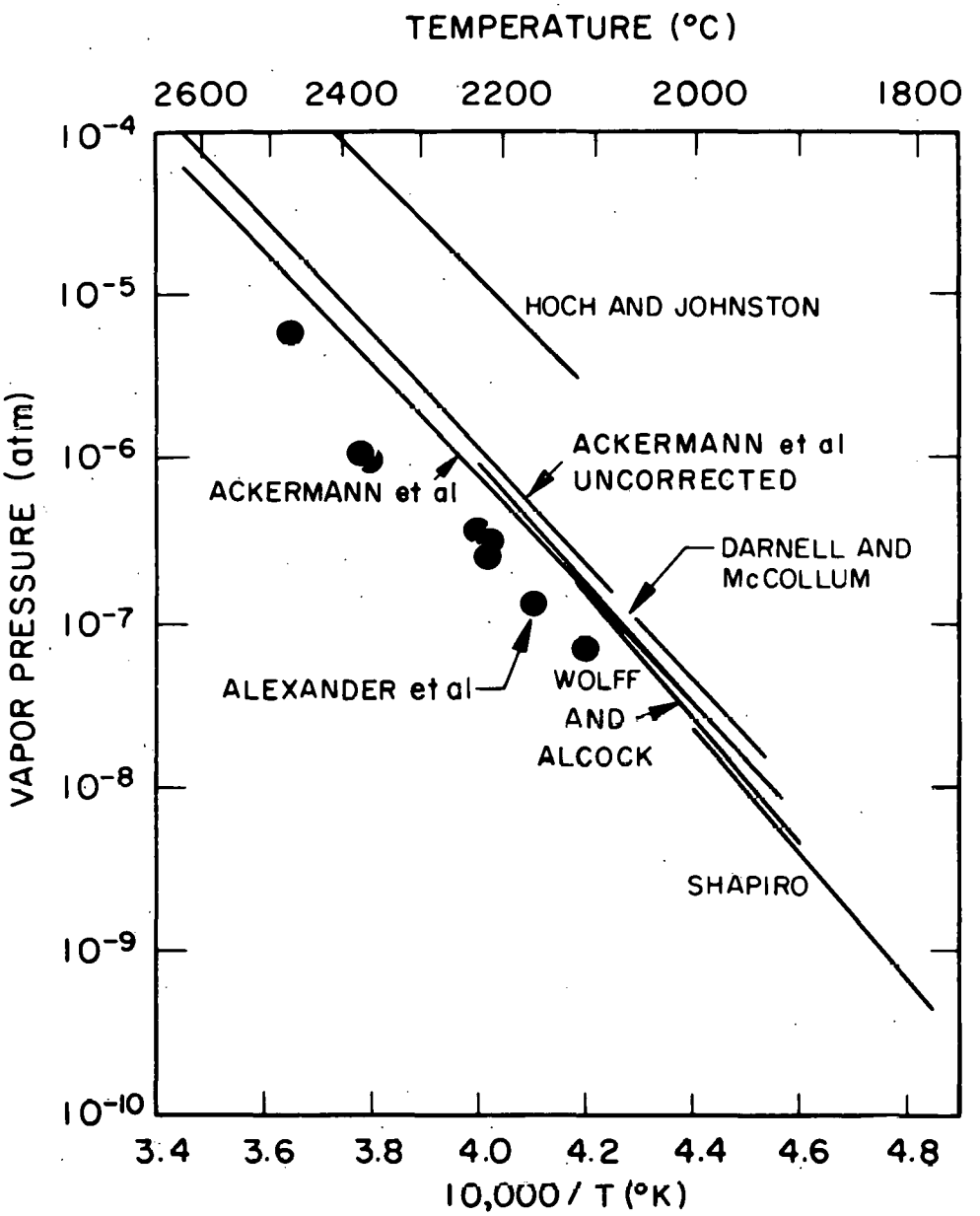

Figure 13. Vapor Pressure of Thoria

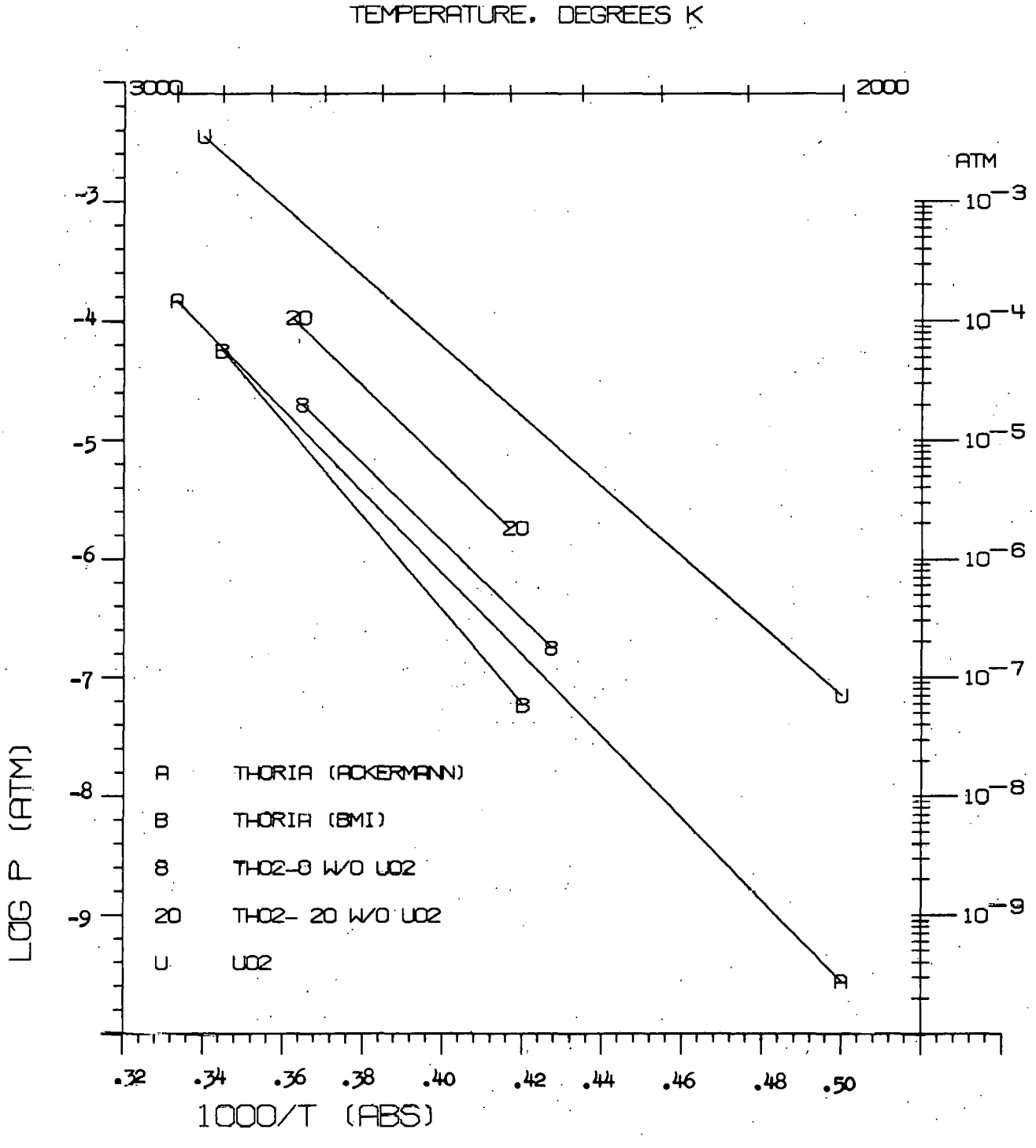

Figure 14. Vapor Pressure of Thoria and ThO_2-UO_2

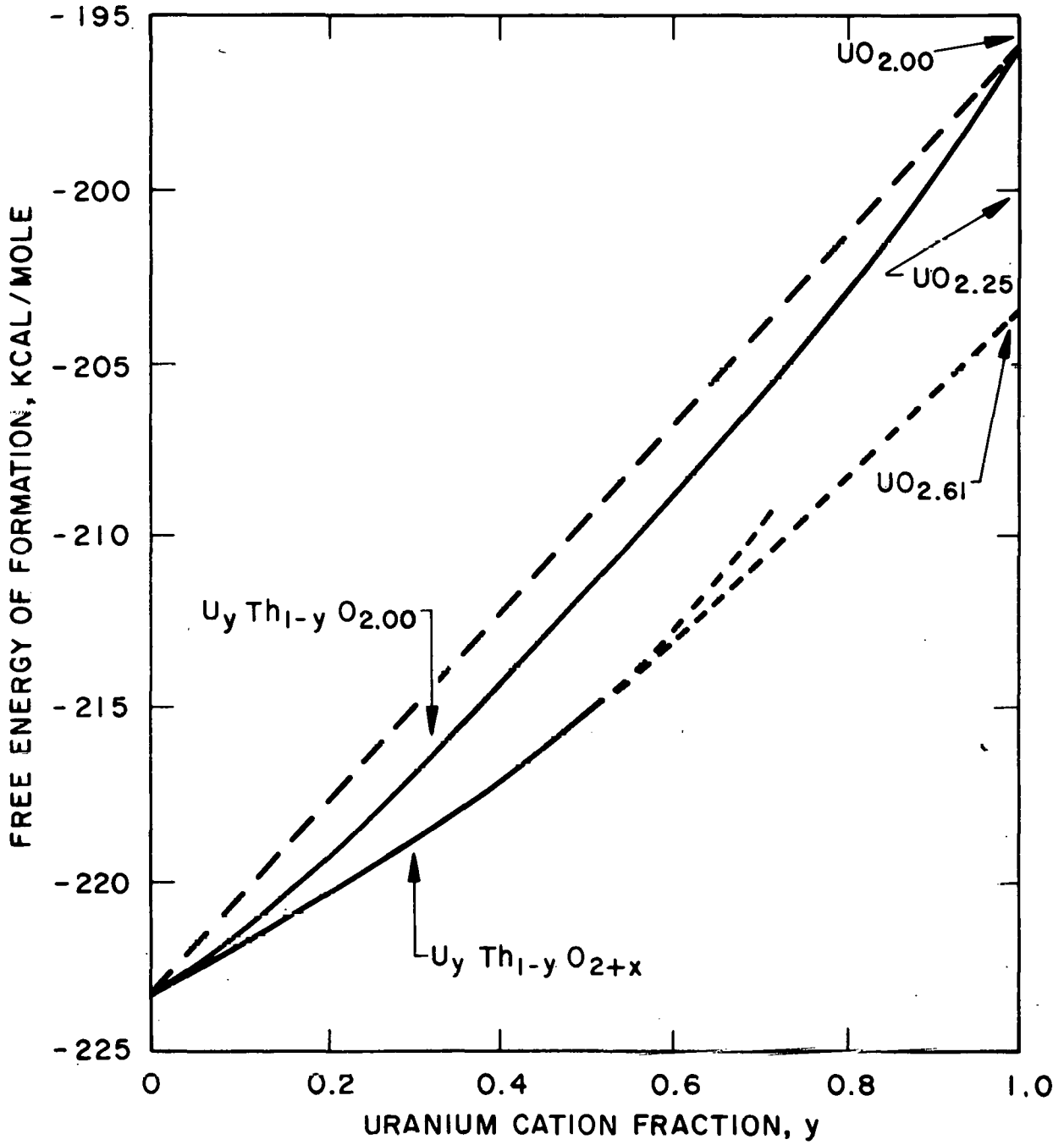

Figure 15. Free Energy of Formation of $Th_{1-y}U_yO_{2+x}$ (According to Reference 55)

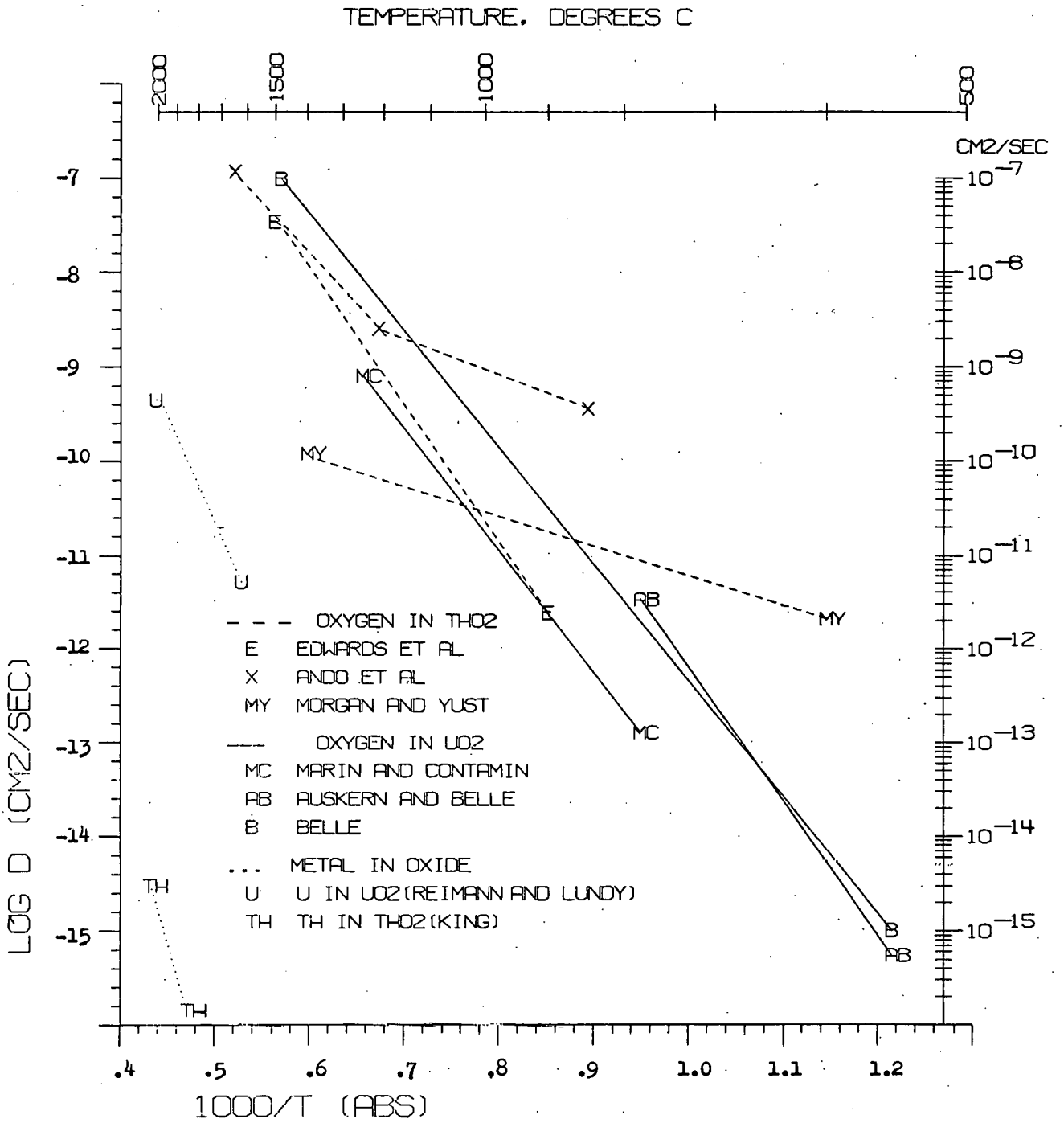

Figure 16. Self-Diffusion in ThO_2 and UO_2

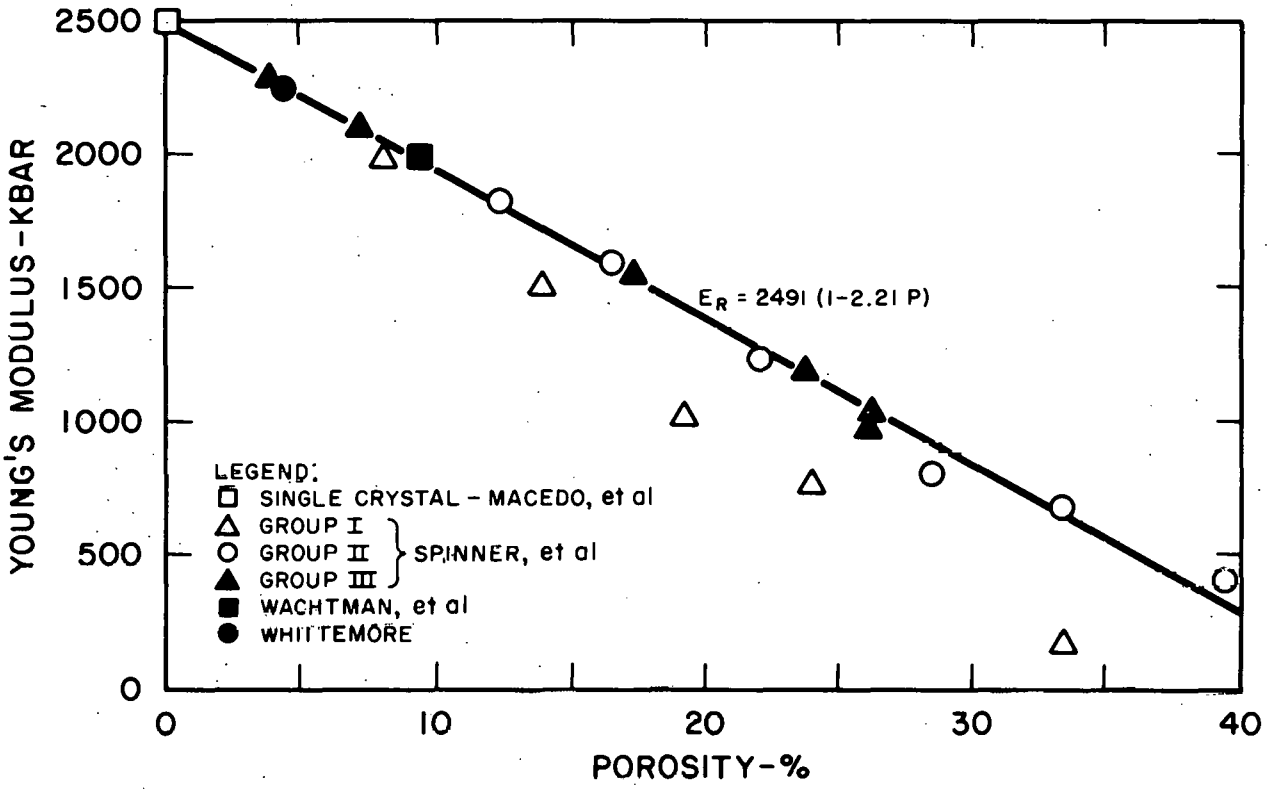

Figure 17. Effect of Porosity on Young's Modulus of ThO_2

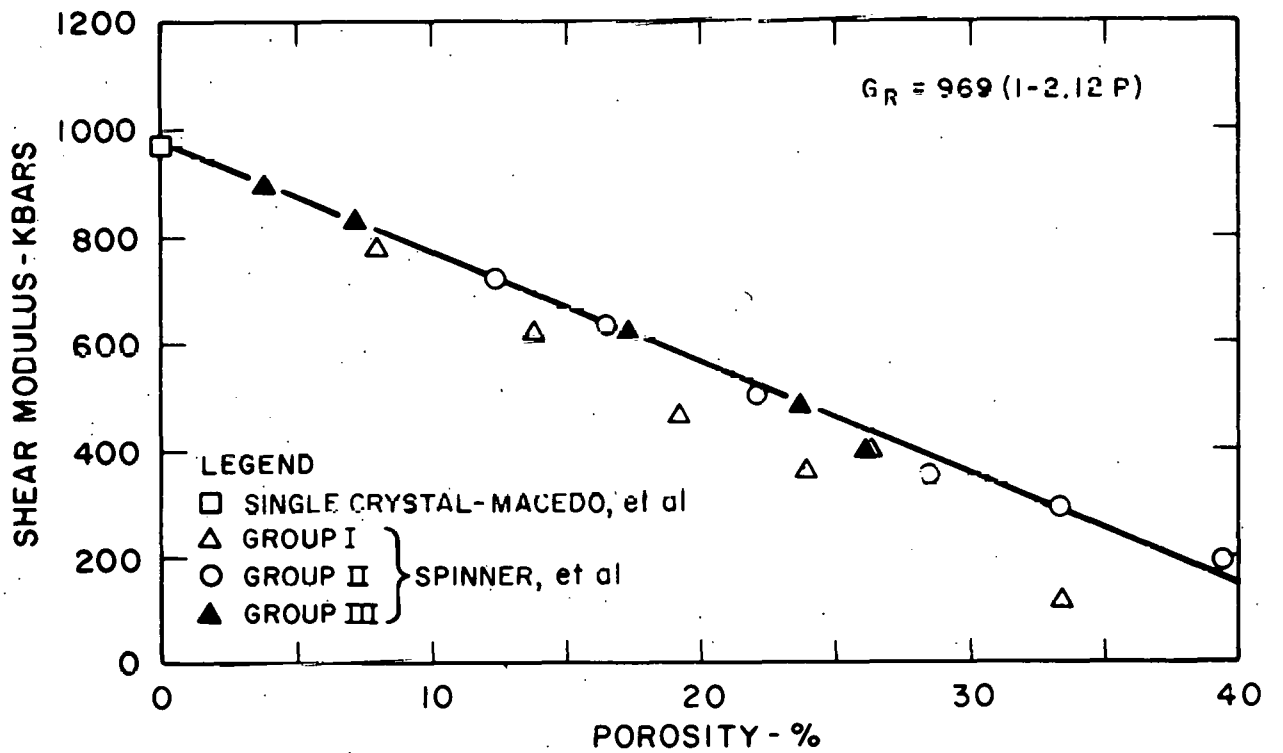

Figure 18. Effect of Porosity on Shear Modulus of ThO_2

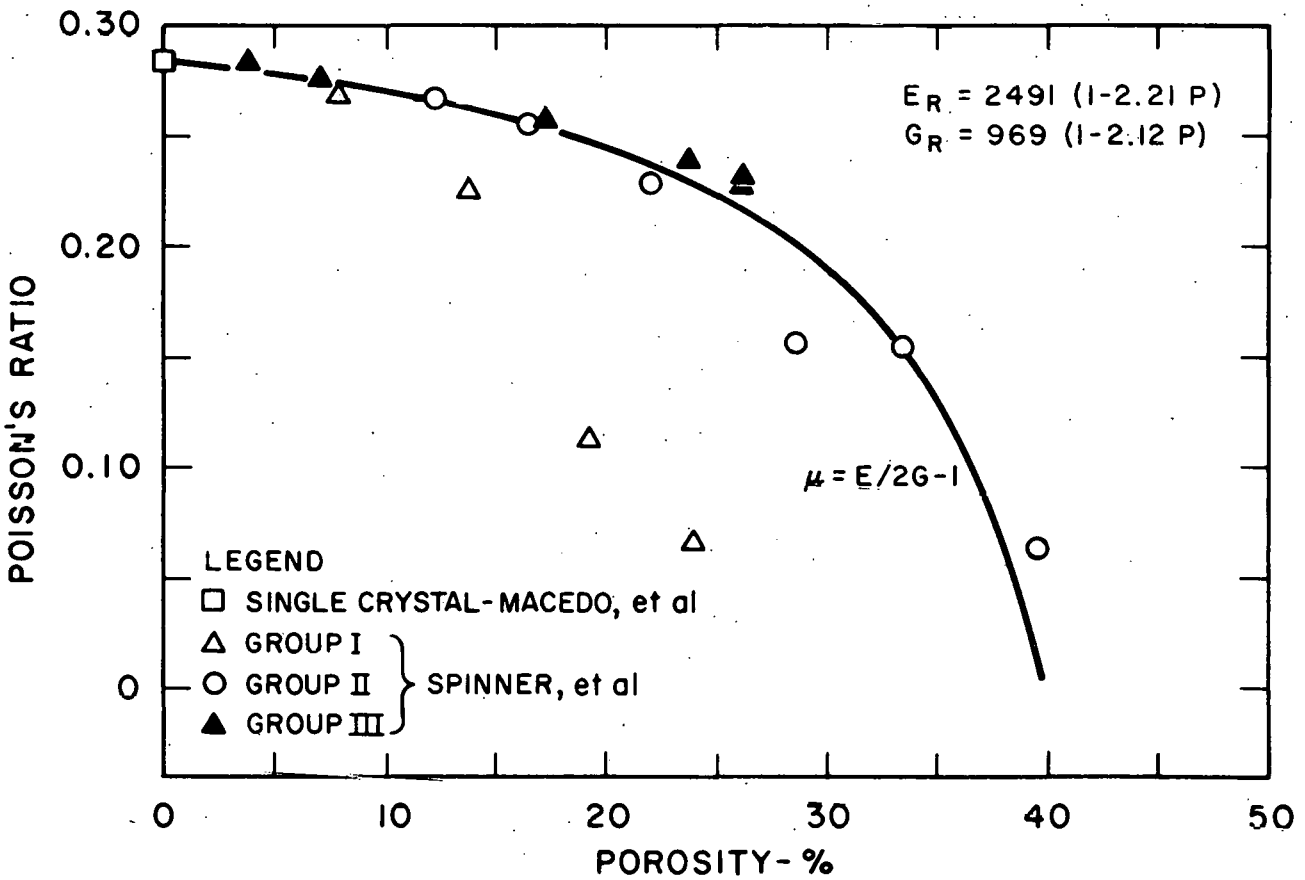

Figure 19. Effect of Porosity on Poisson's Ratio of ThO_2

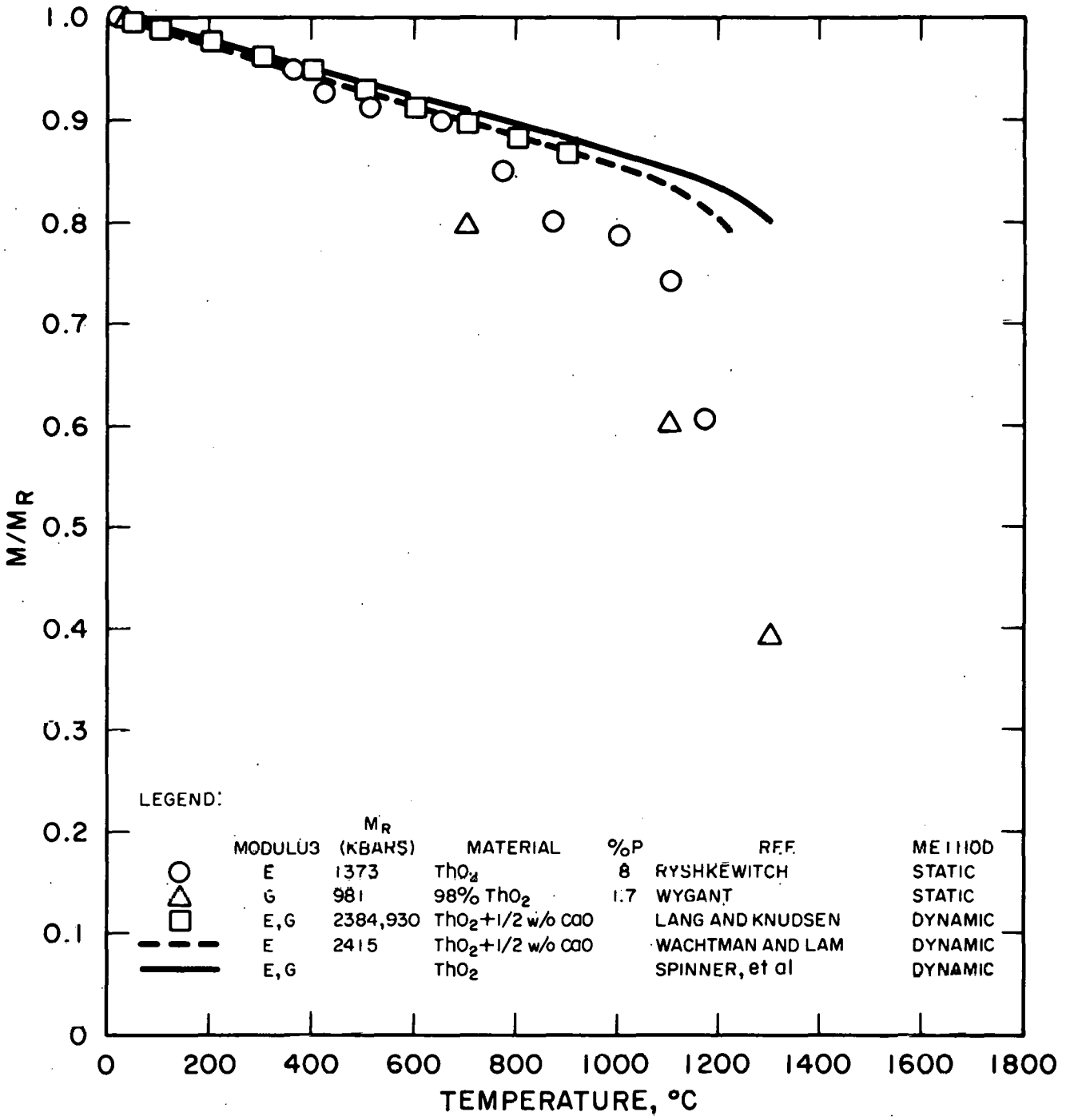

Figure 20. Effect of Temperature on Elastic Moduli of ThO_2 and ThO_2 + CaO

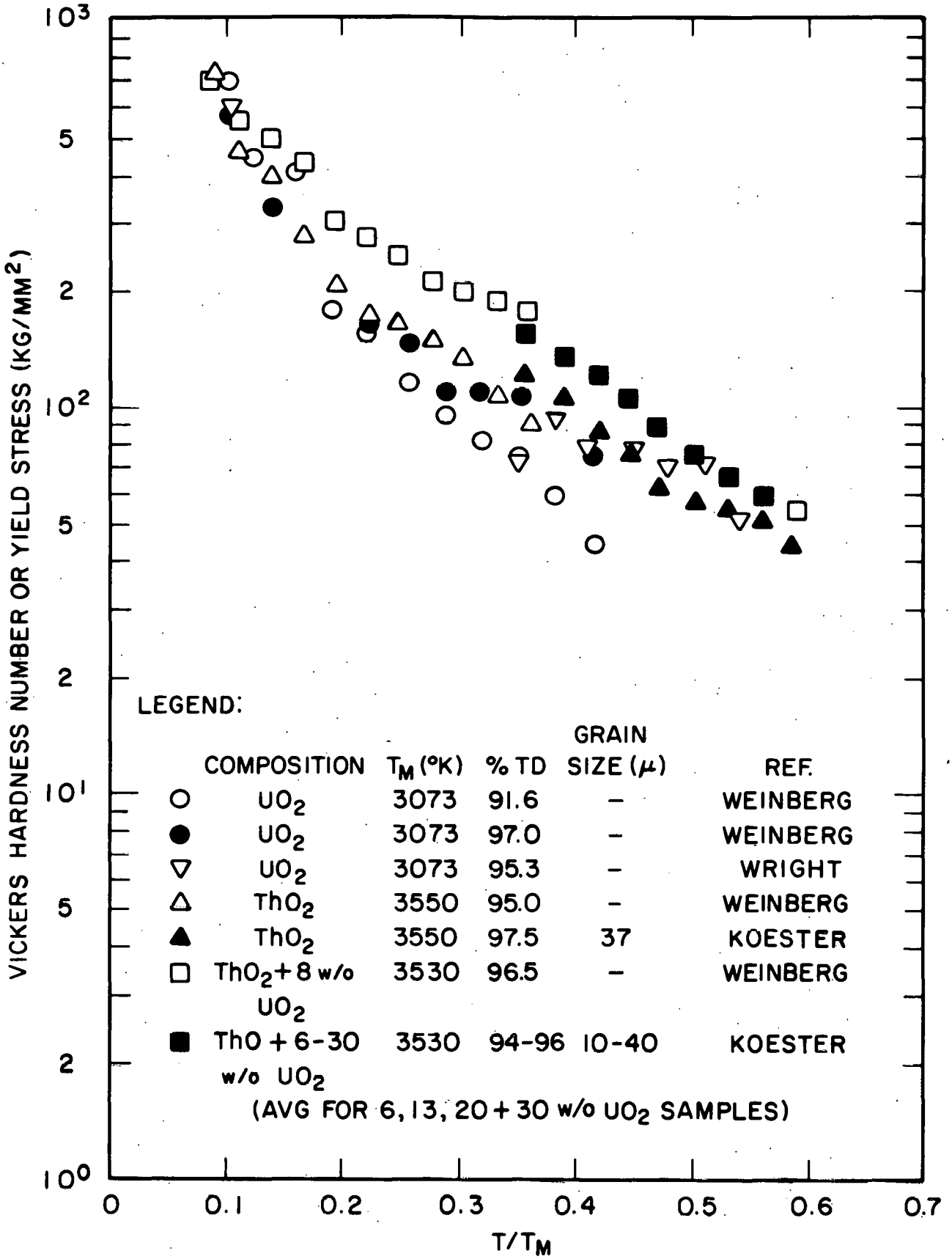

Figure 21. Effect of Temperature on the Vickers Hardness

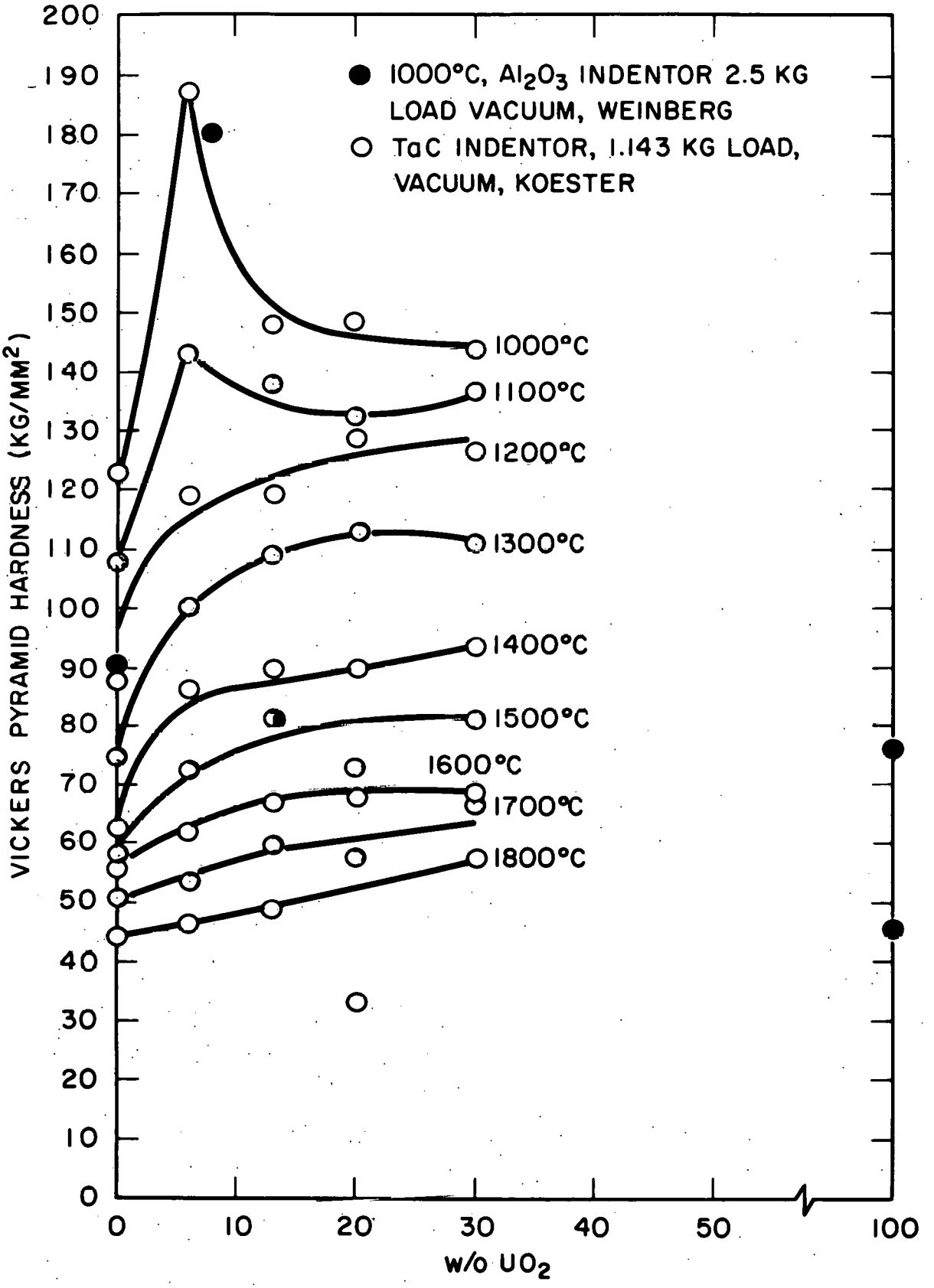

Figure 22. Hot-Hardness Isotherms of ThO_2-UO_2 Compositions

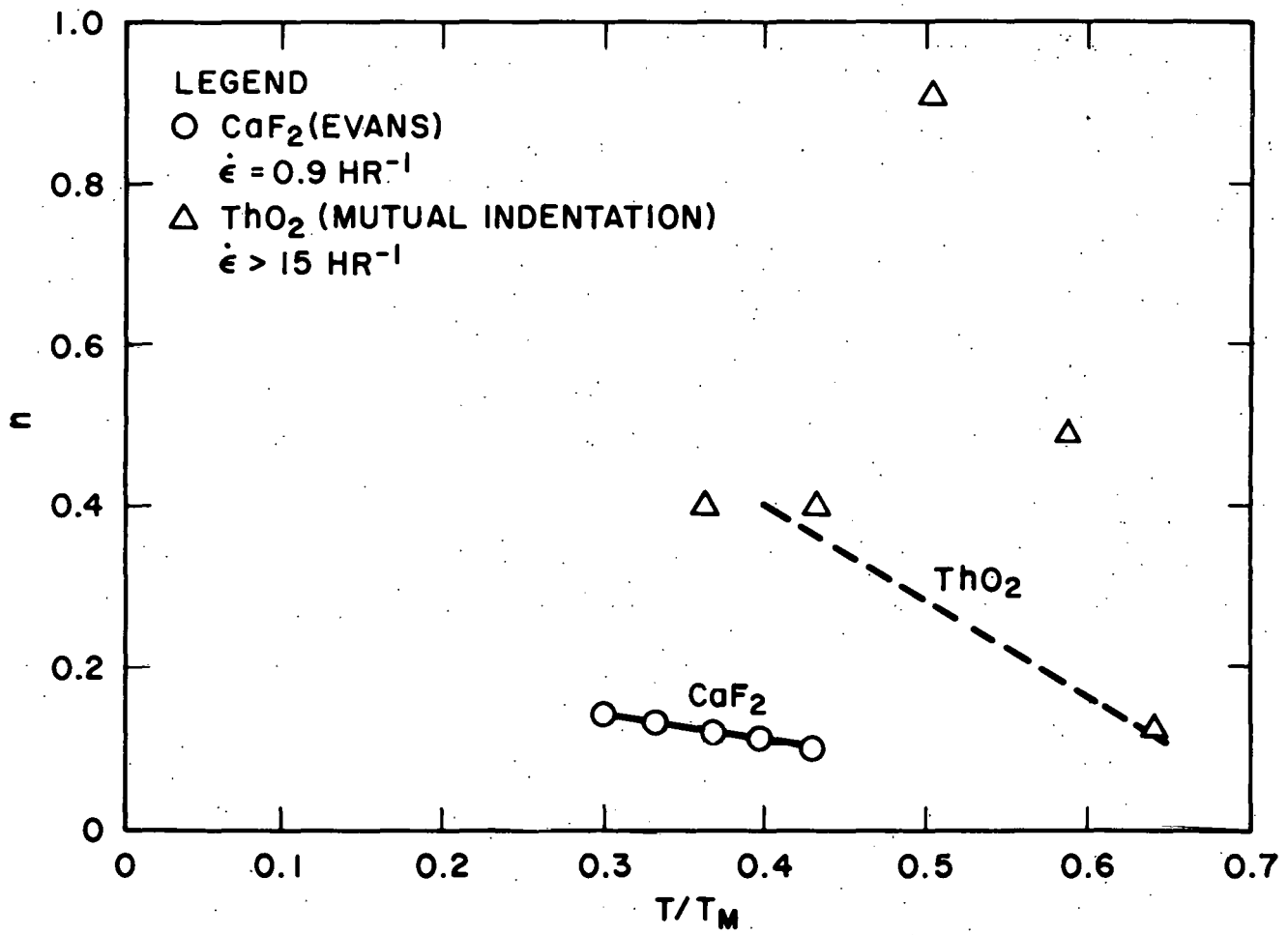

Figure 23. Effect of Temperature on the Work-Hardening Coefficient for ThO_2 and CaF_2

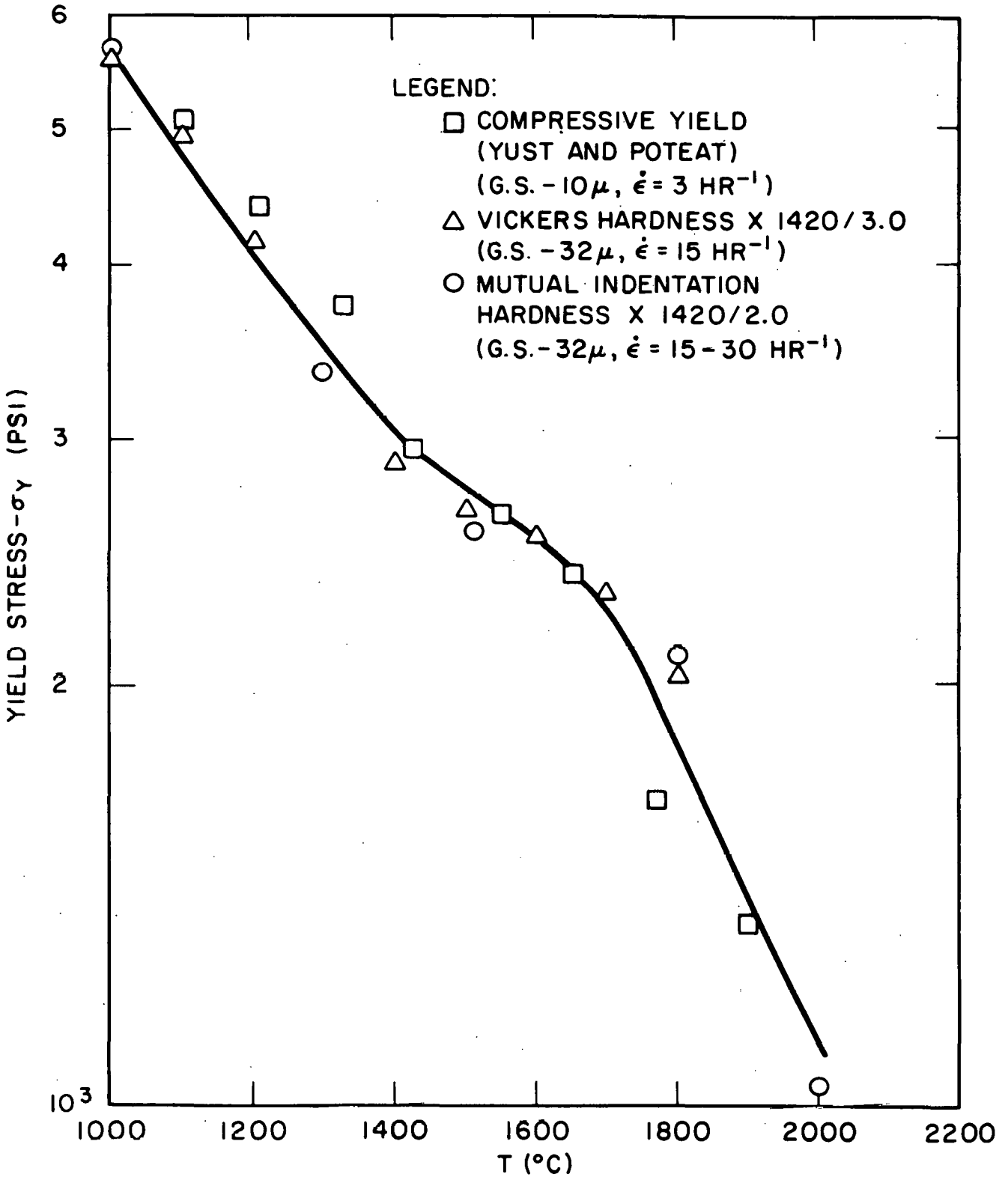

Figure 24. Comparison of Yield Stress Determinations for 97.5 Percent Theoretical Density ThO_2

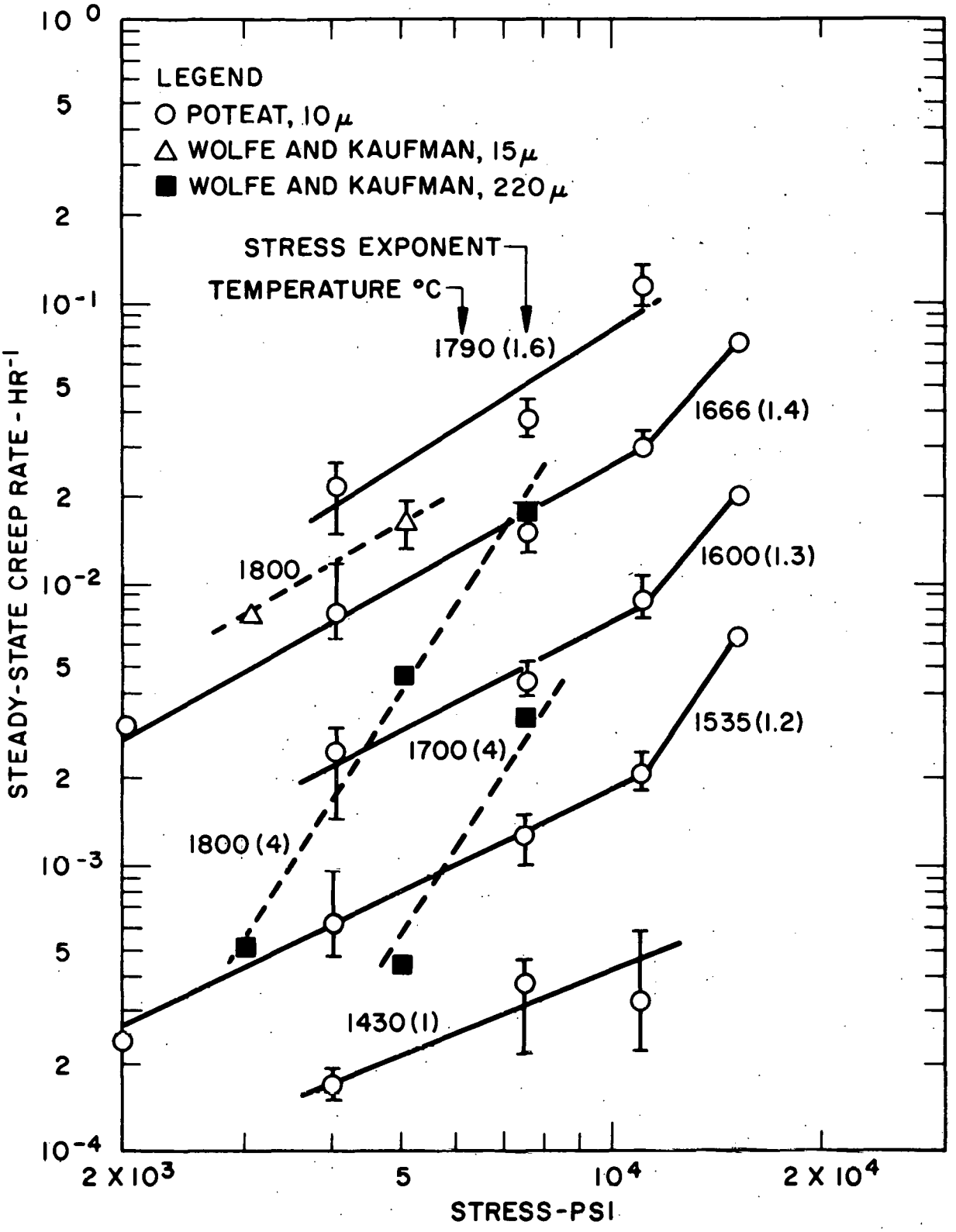

Figure 25. Effect of Stress on Compression Creep of ThO_2

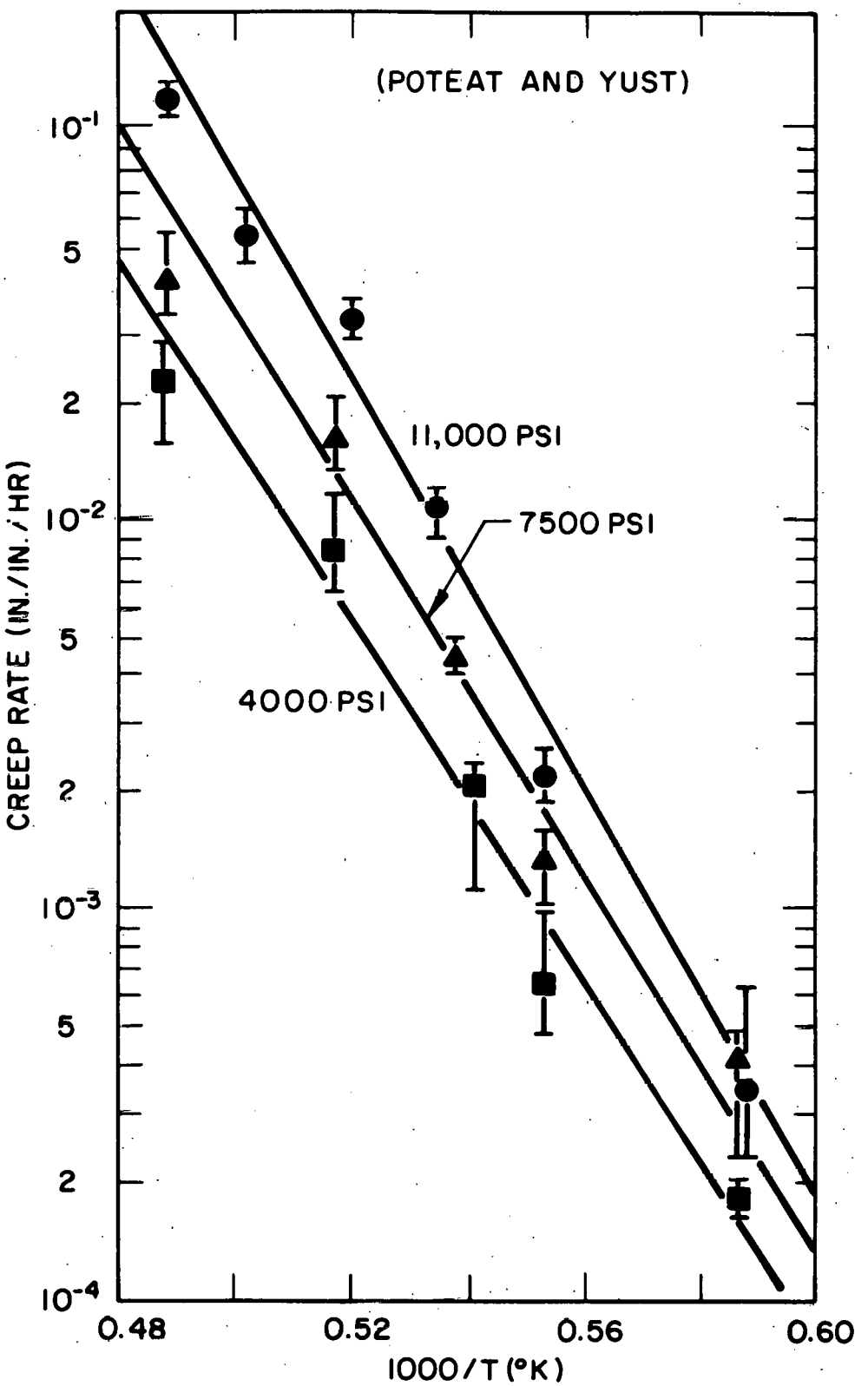

Figure 26. Effect of Temperature on Steady-State Creep of ThO_2 with 10-Micron Grain Diameter

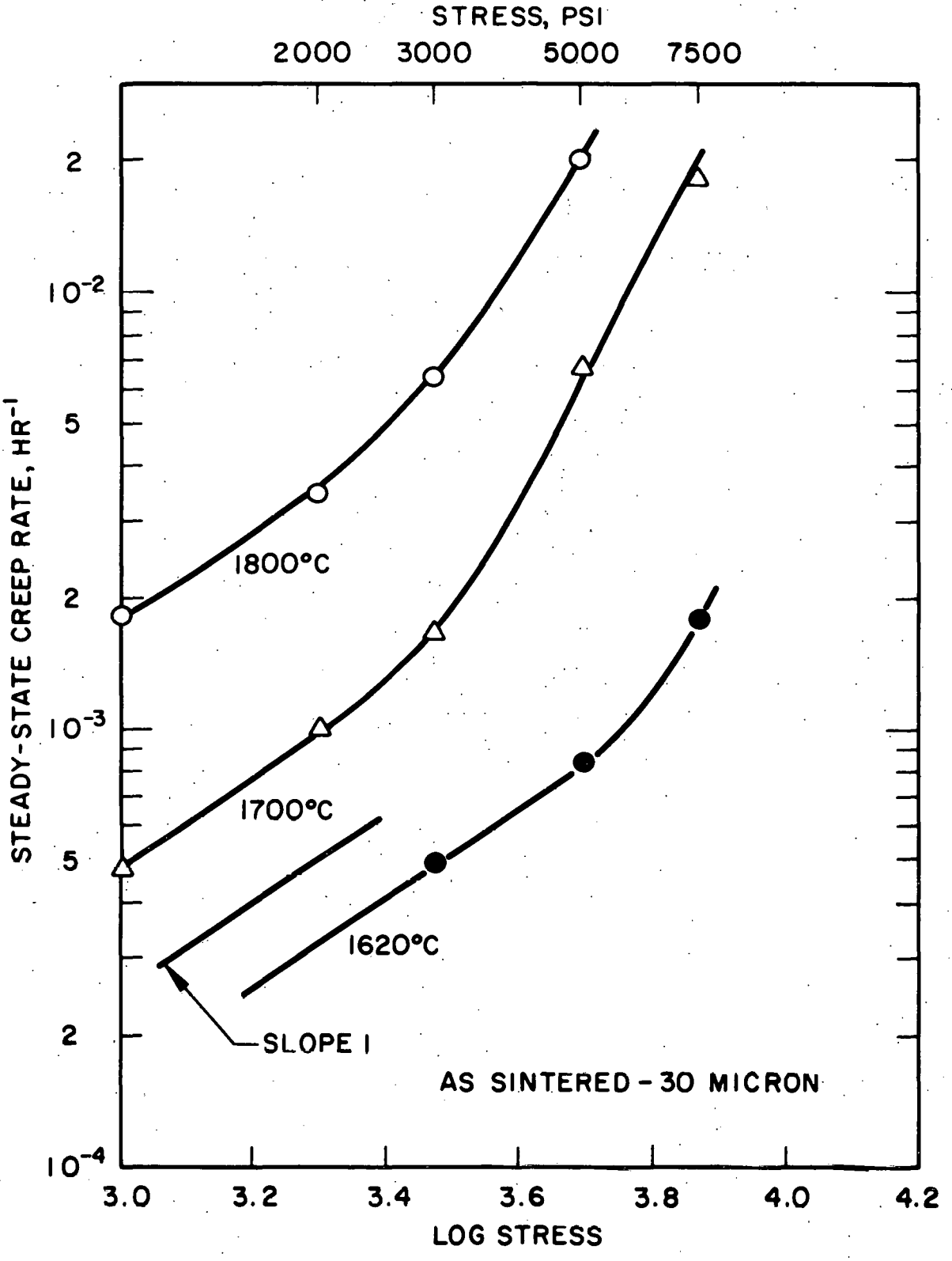

Figure 27. Steady-State Creep Rate of ThO_2-10 w/o UO_2

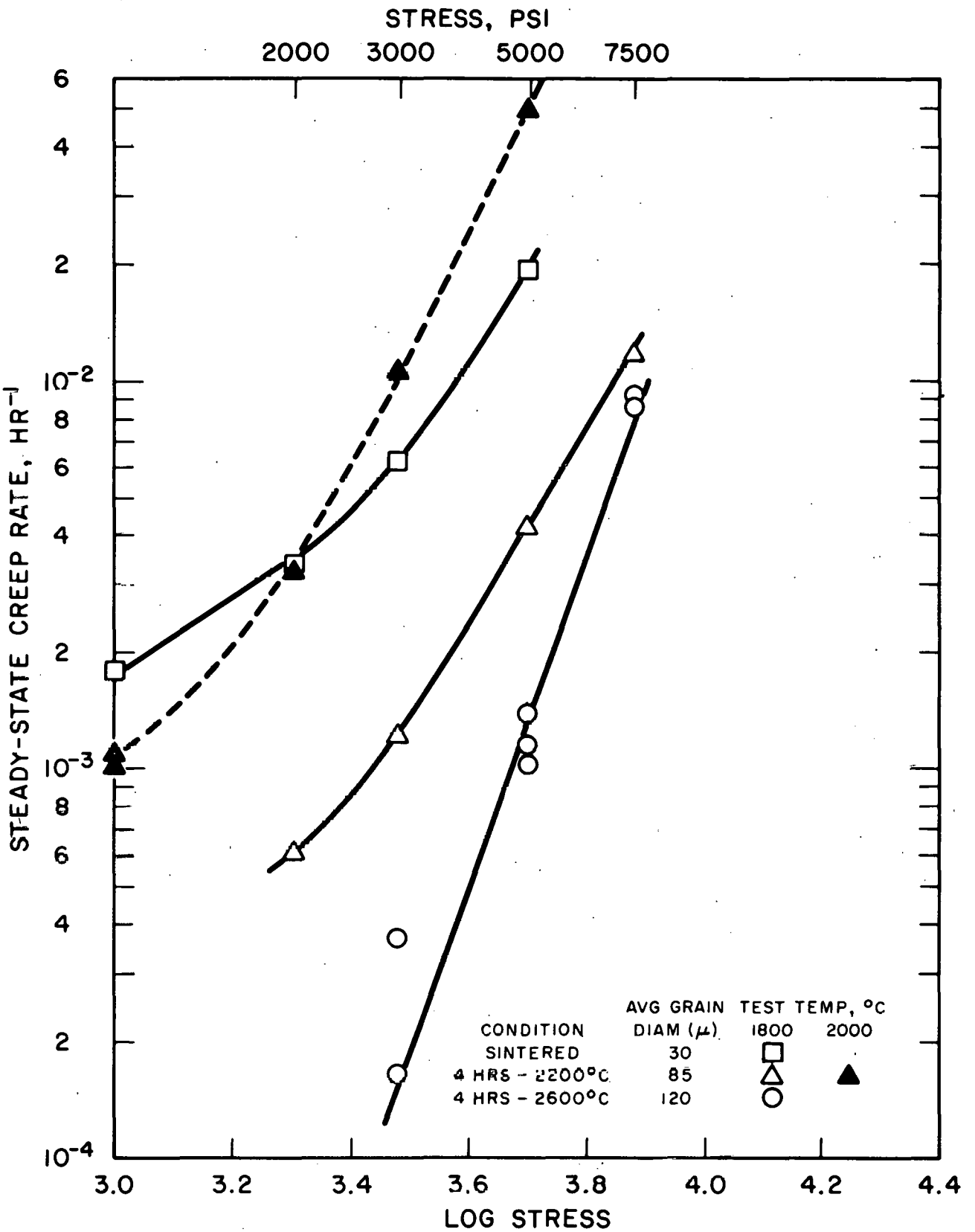

Figure 28. Effect of Stress and Grain Size on Steady-State Creep of ThO_2-10 w/o UO_2

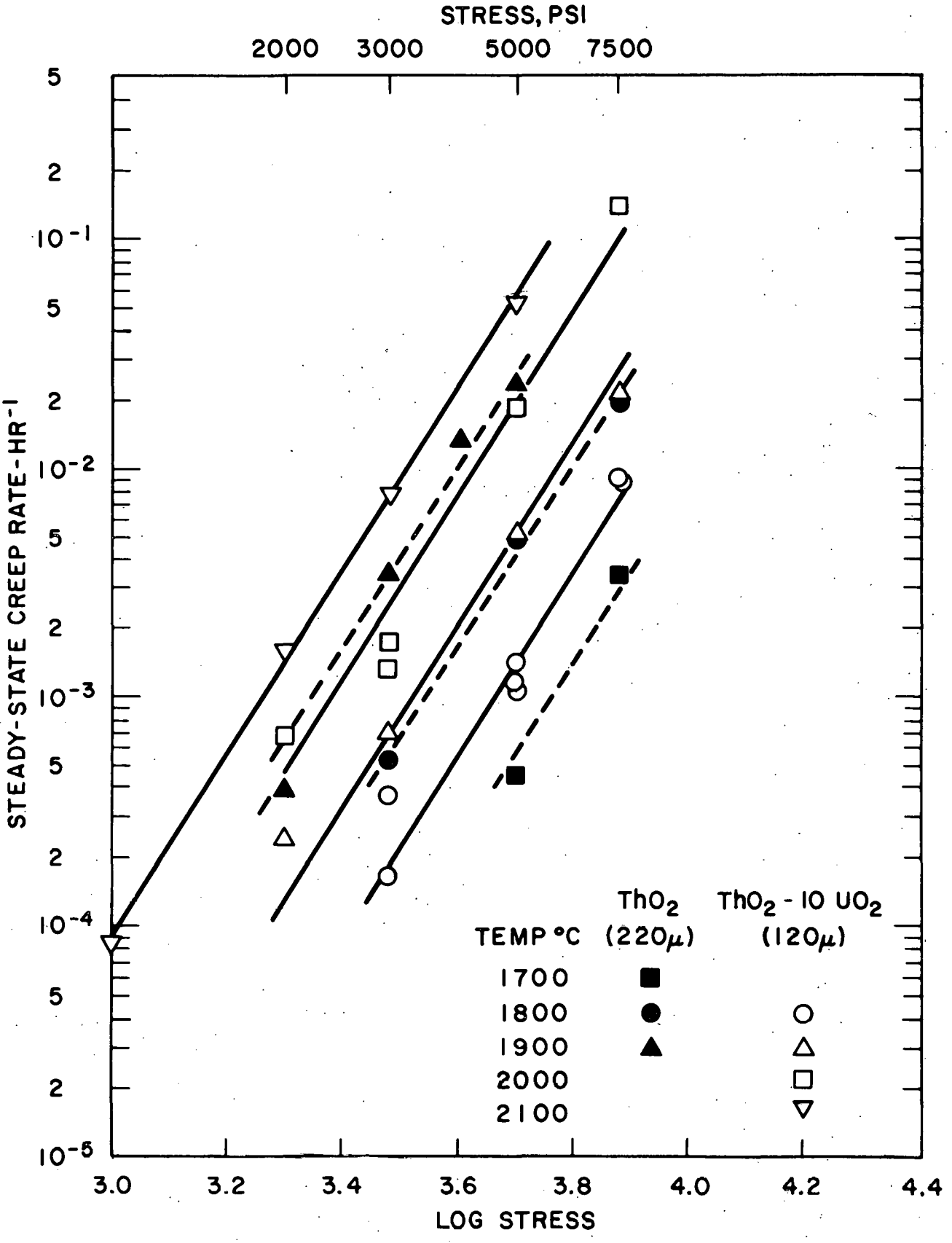

Figure 29. Steady-State Creep Rate of Coarse-Grained ThO_2-10 w/o UO_2

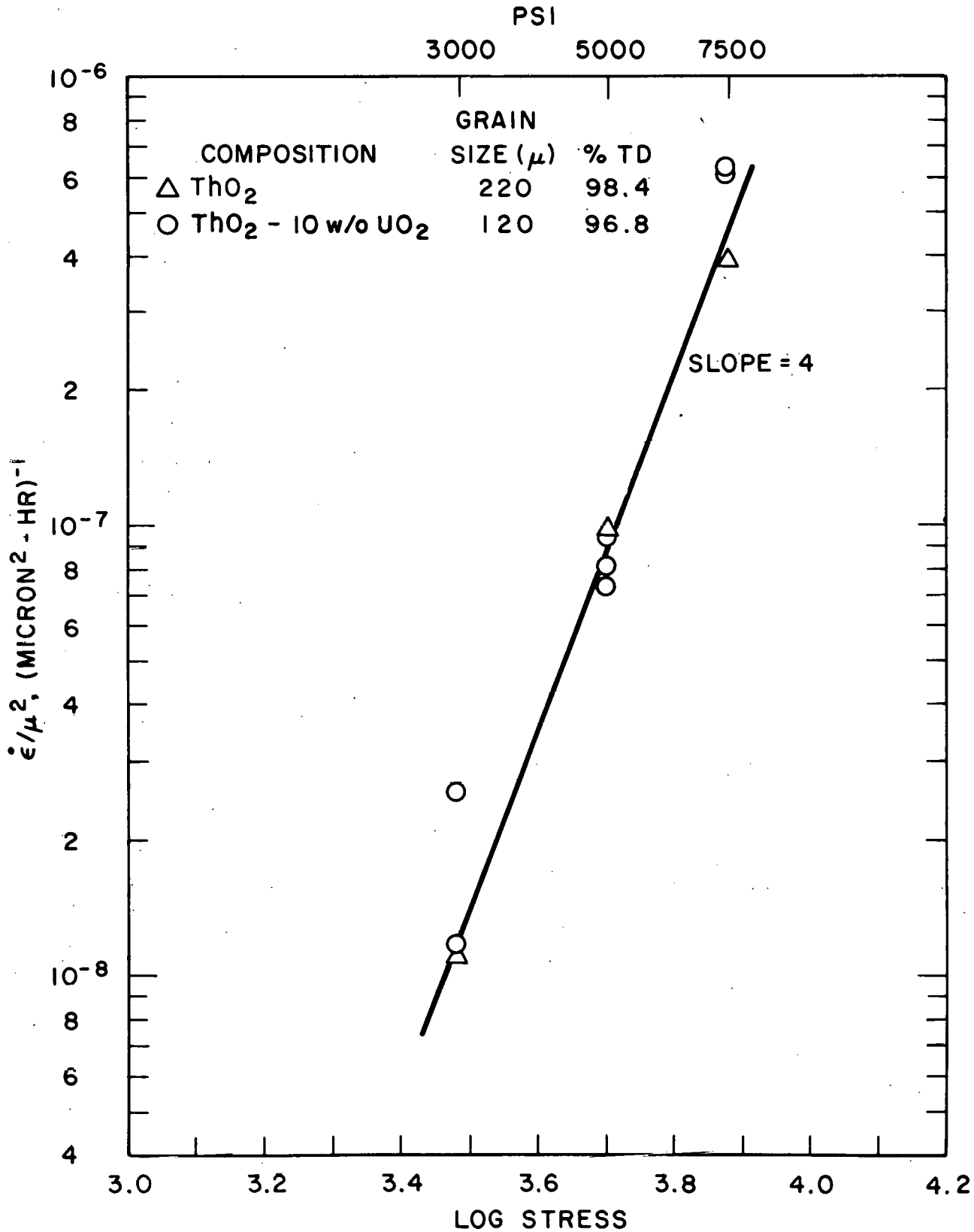

Figure 30. Creep of ThO_2 and ThO_2-10 w/o UO_2 at 1800°C

*U.S. GOVERNMENT PRINTING OFFICE: 1978-703-115/707